DAHLGREN DIVISION
NAVAL SURFACE WARFARE CENTER
Dahlgren, Virginia 22448-5100

NSWCDD/JTR-97/08

MEASUREMENT AND PREDICTION OF PARTICULATE CONCENTRATION WITHIN EXTERNAL AND INTERNAL FLOWS

LISLE H. RUSSELL   PHILIP M. BUSHONG   ROBERT E. RICHARDSON

JOINT WARFARE APPLICATIONS DEPARTMENT

OCTOBER 1997

20031201 082

MEASUREMENT AND PREDICTION OF PARTICULATE CONCENTRATION WITHIN EXTERNAL AND INTERNAL FLOWS

BY

LISLE H. RUSSELL
PHILIP M. BUSHONG
ROBERT E. RICHARDSON

JOINT WARFARE APPLICATIONS DEPARTMENT

OCTOBER 1997

REPORT DOCUMENTATION PAGE

Public reporting burden for this collection of information is estimated to average 1 hour per response, including the time for reviewing instructions, search existing data sources, gathering and maintaining the data needed, and completing and reviewing the collection of information. Send comments regarding this burden or any other aspect of this collection of information, including suggestions for reducing this burden, to Washington Headquarters Services, Directorate for Information Operations and Reports, 1215 Jefferson Davis Highway, Suite 1204, Arlington, VA 22202-4302, and to the Office of Management and Budget, Paperwork Reduction Project (0704-0188), Washington, DC 20503.

1. AGENCY USE ONLY (Leave blank)	2. REPORT DATE October 1997	3. REPORT TYPE AND DATES COVERED N/A

4. TITLE AND SUBTITLE
Measurement and Prediction of Particulate Concentration within External and Internal Flows

5. FUNDING NUMBERS

6. AUTHOR(s)
Lisle H. Russell, Philip M. Bushong, Robert E. Richardson

7. PERFORMING ORGANIZATION NAME(S) AND ADDRESS(ES)
Attn: Code J042
Commander
Naval Surface Warfare Center, Dahlgren Division
17320 Dahlgren Rd
Dahlgren, VA 22448-5100

8. PERFORMING ORGANIZATION REPORT NUMBER
NSWCDD/JTR-97/08

9. SPONSORING/MONITORING AGENCY NAME(S) AND ADDRESS(ES)
N/A

10. SPONSORING/MONITORING AGENCY REPORT NUMBER
N/A

11. SUPPLEMENTARY NOTES

12a. DISTRIBUTION/AVAILABILITY STATEMENT
Approved for public release; distribution is unlimited.

12b. DISTRIBUTION CODE

13. ABSTRACT (Maximum 200 words)
The focus of this report is the formation, growth, and transport of airborne particulate clouds within the boundary layer atmosphere as well as the interaction of such clouds with the terrain surface and objects (e.g., ships and buildings) on the earth's surface. The methodology outlined in the report can be use to answer the simple question "What happens to particulate clouds once they are formed?" The specific particulate subjected to detailed analysis was a millimeter-wave (mmw) obscurant. A novel concentration measurement device (a type of interferometer) applicable to this class of obscurants was used to collect data during a dissemination field test. The experimental data compared favorably to external flow predictions resulting from the *Transport, Diffusion, and Radiance* (TDR) computer code, interim version 3.2. TDR is based on Gaussian statistics with high fidelity physical assumptions governing the behavior of puffs and plumes. Time-dependent concentration, exposure, and deposition histories were calculated and graphically rendered for the mmw obscurant cloud. Predictions were also made of internal room contamination caused by the ingestion of a particulate cloud by a notional, ventilated building. This analysis employed the *Ship Chemical Warfare Vulnerability Ventilation Model* (VENM).

14. SUBJECT TERMS
airborne particulate clouds; millimeter-wave obscurants; concentration, exposure, and deposition histories; Gaussian statistics; computational fluid dynamics; external and internal flows

15. NUMBER OF PAGES
96

16. PRICE CODE

17. SECURITY CLASSIFICATION OF REPORT	18. SECURITY CLASSIFICATION OF THIS PAGE	19. SECURITY CLASSIFICATION OF ABSTRACT	20. LIMITATION OF ABSTRACT
UNCLASSIFIED	UNCLASSIFIED	UNCLASSIFIED	UL

NSN 7540-01-280-5500

FOREWORD

During the recent past, Naval Surface Warfare Center, Dahlgren Division (NSWCDD) personnel gained permission to participate in a previously scheduled test at Dugway Proving Ground, Utah. The Navy portion of the test focused on the performance evaluation of prototype devices that measure particulate concentrations. The particulate concentration measurements were conducted by Robert E. Richardson, Mark F. Katrancha, and Arturo M. Lopez of the Technology Applications Branch of the Systems and Countermeasures Development Division. Assistance in the fabrication of the instrumentation for these measurements was provided by William K. Cary of the Special Systems Branch in the Theater Warfare Sensors Division.

Comparisons to the experimental data were made via use of software that simulated source conditions and atmospheric transport of the particulates. The software package is known as *Transport, Diffusion, and Radiance* (TDR) and was developed with funding from the Joint Program Office for Special Technology Countermeasures.

Additional computational support to the understanding of particulate transport in complex internal and external flows was provided by the Chemical and Biological Systems Analysis Branch in the Chemical and Biological Technology Division at NSWCDD. Mary Beth Morris and Richard A. Amick provided this complementary support.

The report was written with a tutorial flavor and is intended to suggest approaches and limitations to the difficult problems of measuring and predicting particulate concentrations in external and internal flows.

This report has been reviewed by Art Blankenship, Head, Technology Applications Branch and Fred Riedl, Head, Systems and Countermeasures Development Division.

Approved by:

C. E. GALLAHER, Head
Joint Warfare Applications Department

THIS PAGE INTENTIONALLY LEFT BLANK

ABSTRACT

The focus of this report is the formation, growth, and transport of airborne particulate clouds within the boundary layer atmosphere as well as the interaction of such clouds with the terrain surface and objects (e.g., ships and buildings) on the earth's surface. The methodology outlined in the report can be used to answer the simple question, "What happens to particulate clouds once they are formed?" The specific particulate subjected to detailed analysis was a millimeter-wave (mmw) obscurant. A novel concentration measurement device (a type of interferometer) applicable to this class of obscurants was used to collect data during a dissemination field test. The experimental data compared favorably to external flow predictions resulting from the *Transport, Diffusion, and Radiance* (TDR) computer code, interim version 3.2. TDR is based on Gaussian statistics with high fidelity physical assumptions governing the behavior of puffs and plumes. Predictions were also made of internal room contamination caused by the ingestion of a particulate cloud by a notional, ventilated building. This analysis employed the *Ship Chemical Warfare Vulnerability Ventilation Model* (VENM).

Time-dependent concentration, exposure, and deposition histories were calculated and graphically rendered for the mmw obscurant cloud. Parameters that significantly impact the TDR predictions for these quantities were varied as part of a sensitivity analysis. Limitations in particulate concentration measurement accuracy are discussed in an overall sense and are related to predictions resulting from both Gaussian and computational fluid dynamics (CFD) models. Suggestions are provided as to when Gaussian and when CFD modeling approaches are warranted.

THIS PAGE INTENTIONALLY LEFT BLANK

CONTENTS

ILLUSTRATIONS

ILLUSTRATIONS (CONTINUED)

TABLES

1 INTRODUCTION

This report examines the measurement and prediction of millimeter-wave (mmw) obscurant concentration in external atmospheric flows. Local concentration data from a novel near mmw interferometer was compared to results from a robust Gaussian transport and diffusion model. The physical scenario of the field test was complex with many sources contributing to the formation of a large screening cloud. Model prediction agreed very well with local experimental measurements made with the interferometer. Parametric exercises were conducted with the Gaussian model to determine the sensitivity to selected input variables.

The report also addresses modeling approaches by which a given particulate concentration history at a ventilation inlet for a building may be propagated through the ventilated interior rooms as a function of time. In the computational example, inlet obscurant ingestion was varied as was the building ventilation flow. Exposure histories for several rooms were computed. The value and limitation of a simple model in forecasting room exposure predictions is discussed. The power of computational fluid dynamics (CFD) is contrasted with lower fidelity models for both interior and exterior flows. Limitations of both CFD and elementary ventilation models are carefully identified. Employment guidelines for CFD models are suggested for both interior and exterior flows.

THIS PAGE INTENTIONALLY LEFT BLANK

2 EXPERIMENT

2.1 PURPOSE

In support of an obscurant dissemination test, personnel from the Technology Applications Branch (J33) within the Systems and Countermeasures Development Division (J30) of the Joint Warfare Applications Department (J) at the Naval Surface Warfare Center, Dahlgren Division (NSWCDD), constructed an experiment that involved the measurement of mmw obscurant concentration. One objective of the experiment was to investigate the transfer efficiency of mmw obscurants when passing through a simplified ventilation duct. The J33 measurements were performed on a not-to-interfere basis with the primary obscurant experiment. The principal measurement device employed by the J33 personnel was a newly developed near mmw interferometer.

2.2 TEST LAYOUT

The tests described here were conducted on the TS-2 test site at the U.S. Army's Dugway Proving Ground, Utah. The test consisted of a dissemination of mmw obscurant from 216 independent sources randomly distributed over a circle of approximately 110 m radius with center at 32 m west and 5 m north of the center of the test range site as shown in Figure 2-1. The large dissemination area allows the formation of an extensive mmw obscurant cloud that maintains significant attenuation capability for several hundred meters downwind.

For example, at 57.8 seconds after the last source initiated, calculations relevant to a plane 1.5 m above the ground, as viewed from a top-down perspective, indicate an area of $16,416 \text{ m}^2$ having a 6 dB or more one-way attenuation at 24 GHz. This area is essentially circular, thereby yielding a robust mmw screen about 144.6 m in diameter.

The J33 test apparatus consisted of 11 measurements taken at 7 discrete locations. Concentration measurements from the interferometers were available at approximately 0.11-second intervals, while the other measurements were the cumulative aerosol material captured during the test.

The entire J33 data gathering apparatus was just at the edge of the test pad. Figure 2-2 is a side schematic of the J33 experimental layout. The photographs in Figures 2-3, 2-4, and 2-5 further define the experimental geometry. Three microwave interferometers were employed to gather concentration data. Data from the interferometer at station 1 was used in a comparison with the predictive results from the computer model known as *Transport, Diffusion, and Radiance* (TDR) (pre-release) version 3.2.

Data collection by J33 was for a single test. The relevant portions of the experiment began at 10:30 a.m. local time. The sources emitted the obscurant over a 3.4-second interval beginning at 10:30:49.8. The design of the Navy portion of the field test and the associated data acquisition and processing were performed by Dr. Robert E. Richardson, Mr. Mark F. Katrancha, and Mr. Arturo M. Lopez of the J33 branch at Dahlgren.
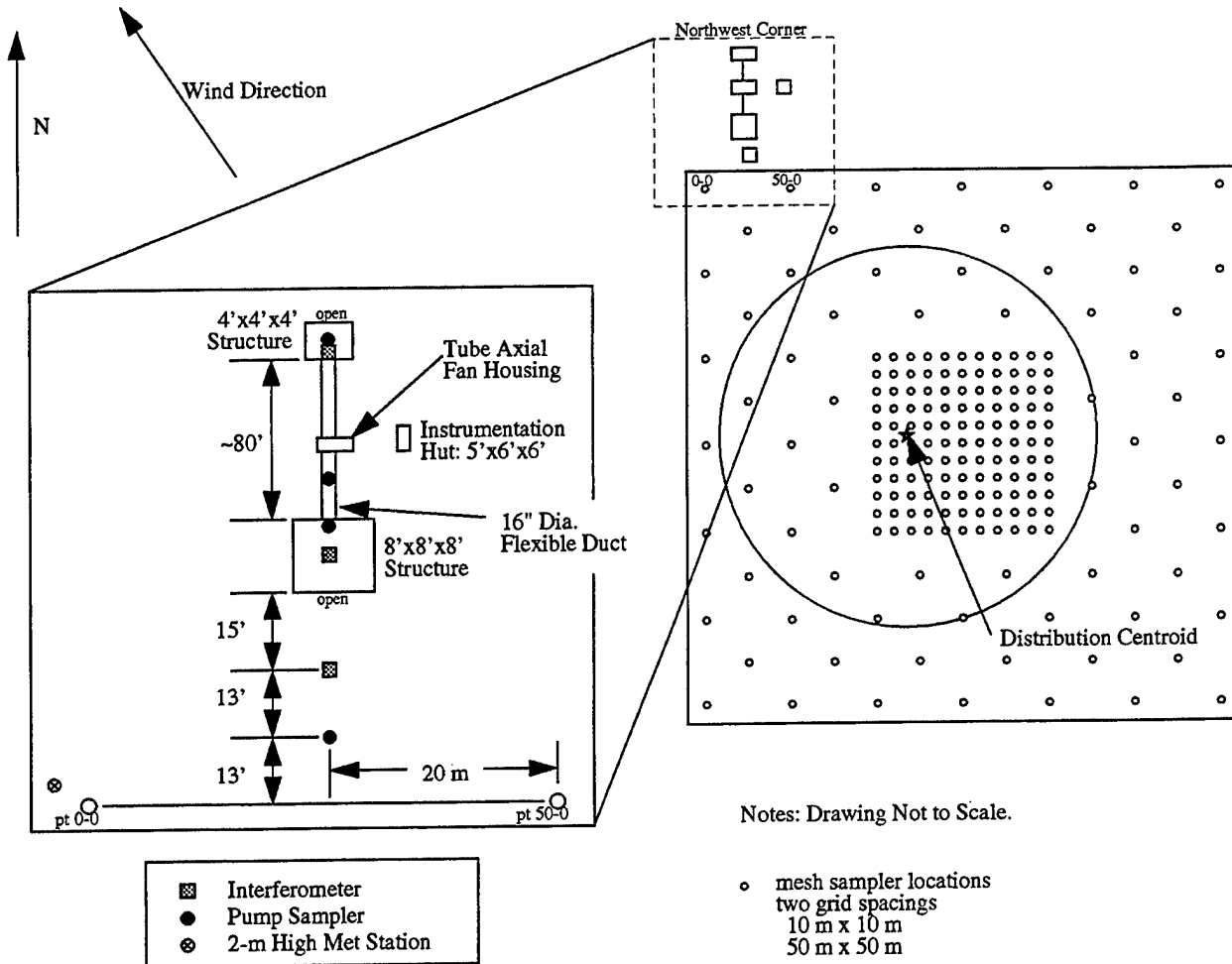
Figure 2-1.   Test Layout at TS-2 Test Site

8'x4'x4' "box"
Front Face Open

Fan

4'x4'x4' "box"
Rear Face Open

40'   40'

— 15'—

	"Mesh" sampler points	(4)
	"Pump" sampler points	(4)
Test Ref	Interferometer measurement points	(3)
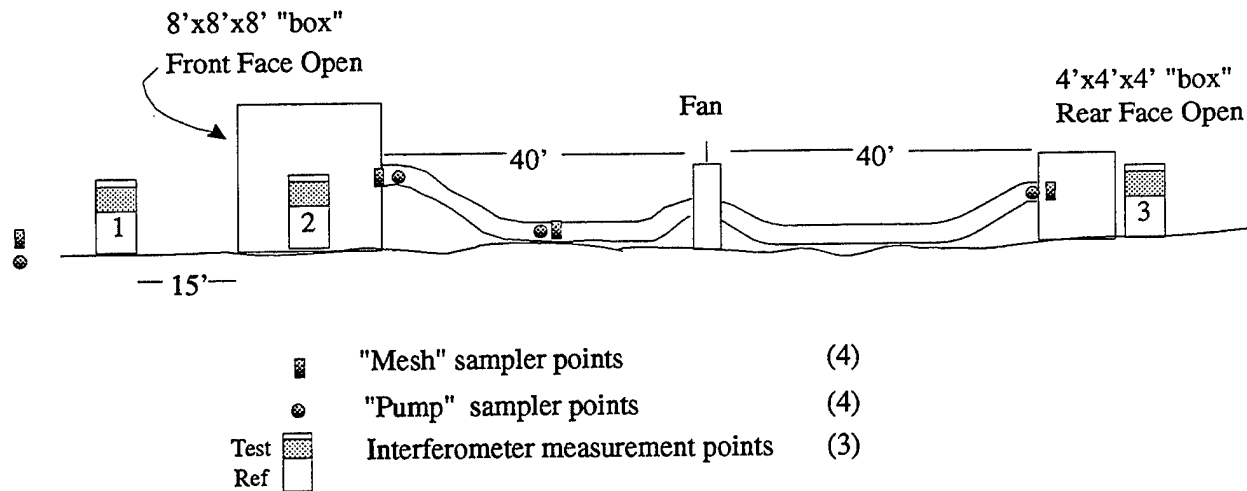
Figure 2-2.   Side Schematic of J33 Test Geometry
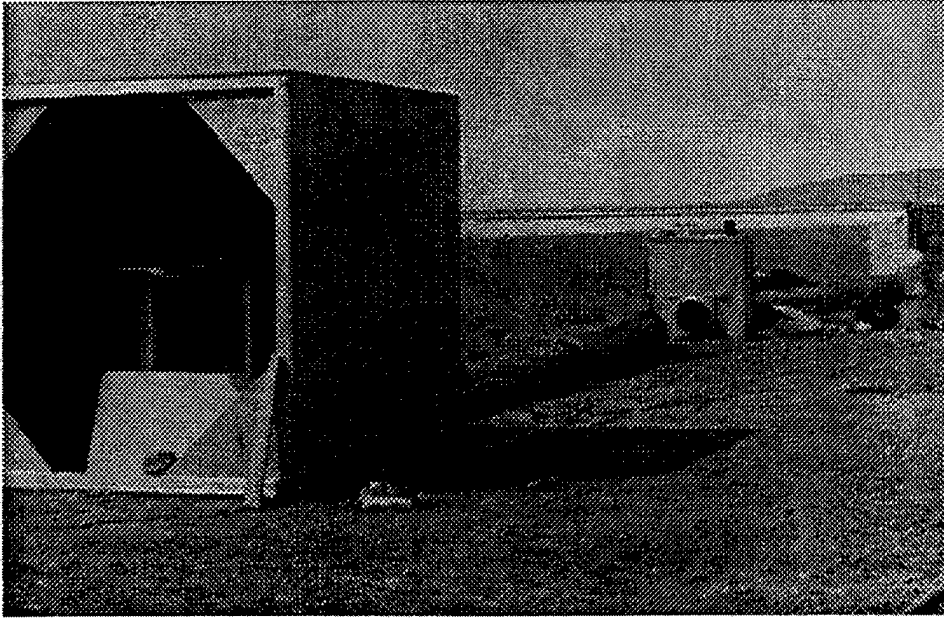
Figure 2-3.   View of Test Apparatus From South East
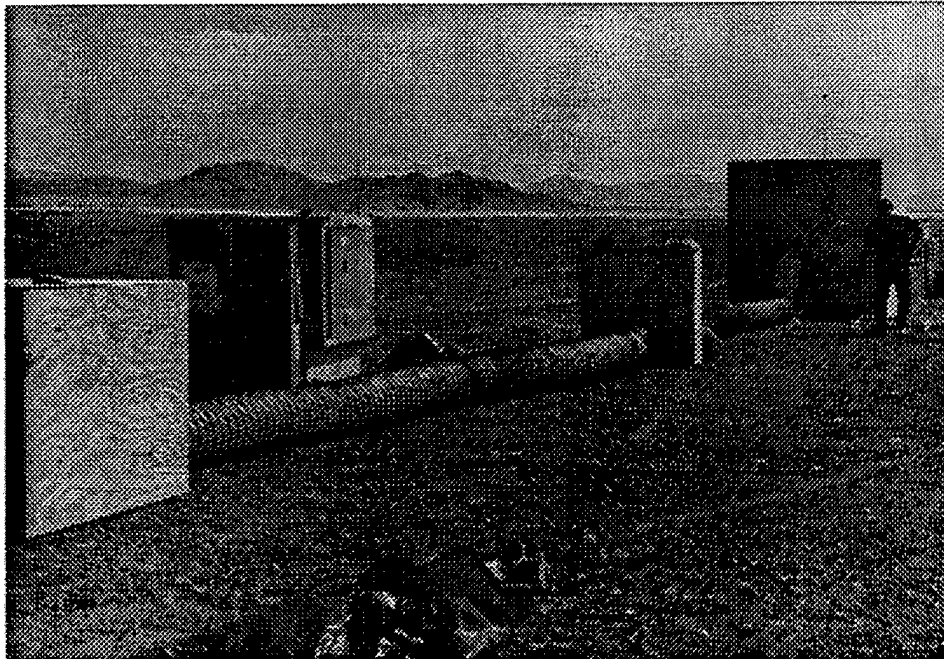
Figure 2-4.   View of Test Apparatus From North West
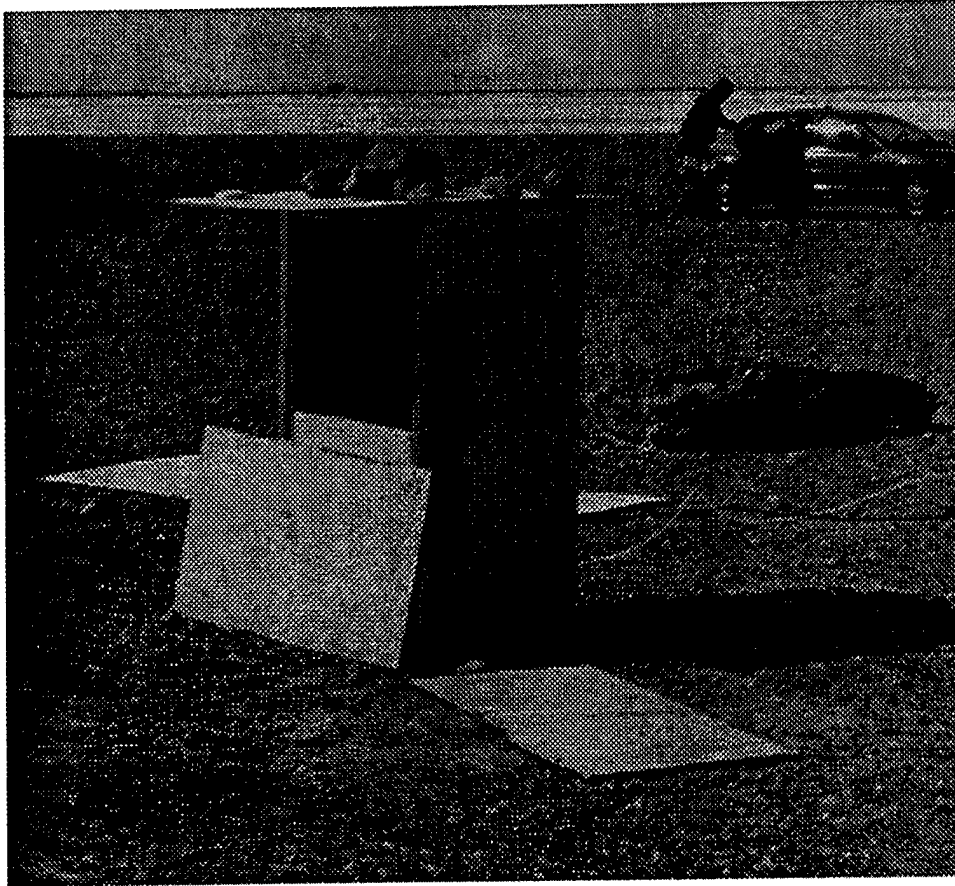
Figure 2-5. Station 1 Interferometer

3 INTERFEROMETER MEASUREMENTS AND RESULTS

3.1 INTERFEROMETER MEASUREMENT APPROACH AND TECHNIQUES

Since the mmw interferometer technique for mmw obscurant concentration measurement is new, a brief description of the operation and calibration of the device is included here. The interferometer operates at a nominal 24 GHz and interrogates a specific geometric measurement space while simultaneously comparing the receiver response to that resulting from a sealed reference space. The range of operation for the interferometer source is from 23.9 to 24.2 GHz. Within the measurement volume, the electromagnetic emission is primarily attenuated and secondarily phase shifted by the airborne obscurants. The measurement or test arm is located directly above the reference arm as shown schematically in Figure 3-1. Figure 2-5 is a photograph of one of the interferometers used in the test. Figure 2-5 clearly shows the 2×2 ft aperture through which the ambient atmosphere can flow. The center of this aperture is 1.5 m above the ground and lies within the horizontal measurement plane of the active arm of the interferometer.

Figure 3-1 is a schematic of the interferometer design. The relationship between the measured attenuation and the obscurant concentration is made by assuming Beer's Law attenuation[1] and using calculated values of absorption cross section for the individual particle. As indicated in Figure 3-1, the length parameter L that was used in Beer's Law was 50 cm. There is thus a quantitative trail based on high fidelity physics relating the output voltage of the interferometer to a concentration estimate for mmw obscurants.
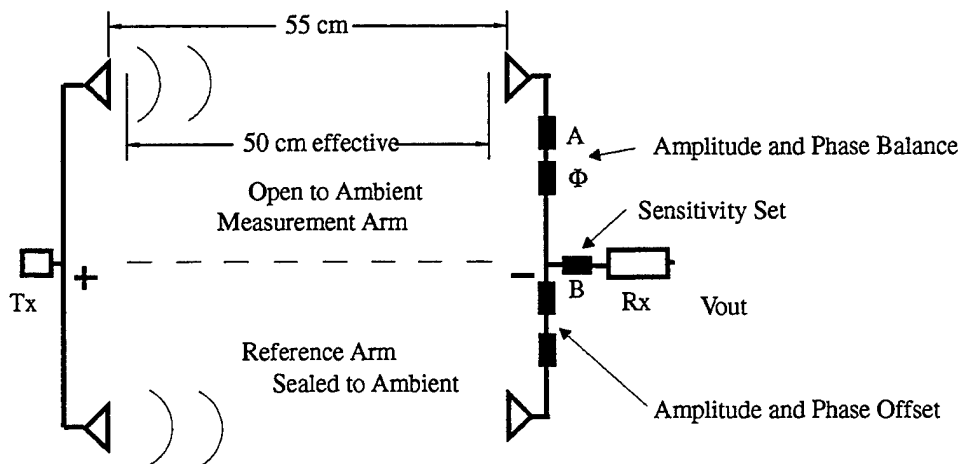
Figure 3-1. Millimeter Wave Interferometer Schematic

A basic problem in transmissometry is that of obtaining required sensitivity. Attenuation is proportional to the product of path length (L), particle absorption cross section (σ_a), and concentration (N). If measurement requirements are such that the path length must be short, then only a small amount of attenuation

---

[1] Relative transmittance may be calculated by using Beer's Law:

$$\frac{T}{T_0} = e^{-\alpha_e c_m L}$$

where

α_e = extinction coefficient (m^2/gm)

c_m = aerosol mass concentration (gm/m^3)

L = optical path length (m)

may be observed. The interferometric architecture operates somewhat like a Wheatstone bridge and thus allows small attenuation levels to be measured as a departure from equilibrium. Very high receiver (Rx) gain may be used thus yielding high sensitivity limited ultimately by the mechanical stability of the system. The design is based on inexpensive 24.125 GHz Gunn oscillator devices that are commercially available for use in police Doppler radar sets and other motion detecting devices.

3.2 INTERFEROMETER DESIGN

Symmetry is used in the measurement and reference arms of the system as shown in Figure 3-1.[2] The device is constructed so that the receiver (Rx) senses the difference in amplitude and phase of waves that travel from the measurement and reference transmit horns and appear at the input to the receiver. Tuning the interferometer is accomplished by setting the amplitude and phase offset, and amplitude and phase balance (A and Φ) attenuators and phase shifters so that a balanced condition is observed and the receiver output voltage is zero. The sensitivity-setting attenuator B does not affect the balance of the system.

3.3 INTERFEROMETER SENSITIVITY DETERMINATION

The receiver responds to the magnitude of the difference between the reference and measurement beam signals without distinguishing whether it is due to amplitude or phase imbalance. This is shown graphically in Figure 3-2. A simple geometrical calculation shows that for small departures from balance, 1 dB of attenuation is equivalent to 11.78 deg of phase shift. Sensitivity calibration and setting can be accomplished in two ways. First, by proper adjustment of the A and Φ controls, the system can be thrown out of balance a known amount and the output voltage can be observed and set to a convenient value by adjustment of the variable attenuator B. Secondly and more conveniently, a standard transmission test sample can be placed in the measurement beam and the output voltage can be set to an appropriate value.

Reference Beam

Difference between
Reference and Measurement Beam

Measurement Beam

(Attenuated and Retarded
due to Propagation through
Fiber Atmosphere)
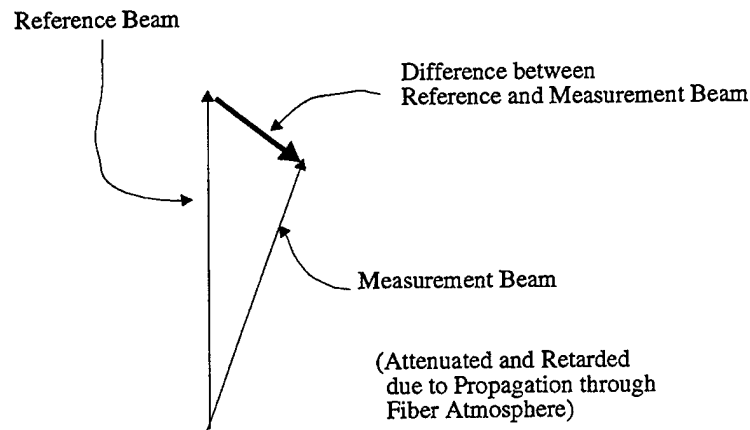
Notes: System responds to difference in beams, not distinguishing between amplitude and phase.

1 dB attenuation is equivalent to 11.78 deg of phase retardation.

Calibration standard can be amplitude or phase.

Attenuating mmw obscurants produce primarily an amplitude difference.

Figure 3-2.   Interferometer Detector Input Signals

It can be shown (see Reference [1]) that the electric field transmission factor T for an electromagnetic wave normally incident on a low loss dielectric sheet can be given by

$$T = \frac{4Pn}{(n+1)^2 - P^2(n-1)^2} \tag{3-1}$$

---

[2] Dr. Robert Richardson of J33 was the designer of this novel interferometer system.

where

$$P = \exp(i2\pi nd/\lambda_0) \tag{3-2}$$

The quantity d is the thickness of the sheet, n is the index of refraction given as the square root of the relative dielectric constant ($n = \sqrt{\epsilon}$), and λ_0 is the free space wavelength. As shown in Table 3-1, for a nearly lossless material like polyethylene ($\epsilon = 2.25$), with a thickness (d) of a few mils, the magnitude of T is nearly unity but the wave slows appreciably creating a phase shift. If a thin polyethylene sheet is inserted in the test arm of the interferometer, the phase shift will result in an imbalance condition that can be used for calibration and setting the sensitivity.

Table 3-1. Calculated E Field Transmission Factors for Thin Polyethylene Sheet at 24 GHz

Thickness (mil)	-20 Log T (dB)	Arg T (deg)	"Effective Attenuation" (dB)
1.5	0.000607	1.77	0.153
4.0	0.004	4.69	0.4

As a check on assumptions made in designing and operating the system, calibration sensitivity was measured by both the sheet insertion technique and the A and Φ control technique. The two techniques yielded comparable results.

3.4 RELATIONSHIP OF INTERFEROMETER SENSITIVITY TO PARTICULATE CONCENTRATION

Interferometer sensitivity was determined by setting a given detector output voltage for a given effective beam attenuation. Next it is necessary to relate the attenuation to a particulate concentration.

Mmw obscurant particle concentration is deduced from measured attenuation by assuming that Beer's Law is governing. The measured attenuation is assumed to be a function of the following parameters: N, the number of particles per unit volume in units of particles/cm^3; σ_a, the absorption cross section of a particle in units of cm^2/particle; and L, the path length of the transmitted beam in units of cm. The value used for σ_a can be calculated from any of several models (see Reference [2]) that have yielded predictions favorably comparable to measured results. The specific model used to compute σ_a was the original Pedersen analytic expression (see Reference [3]).

Ambiguities may, however, be implicit in the calculation for σ_a. These may be present because of uncertainties in those properties of the particles that are functionally important in the σ_a calculation. For example, uncertainty may exist in the diameter, length, and electrical conductivity of the particle. Also, there may be uncertainty in how many fibers actually comprise an average particle.[3]

One-way attenuation of the beam as caused by aerosolized particles is determined by the following form of Beer's law.

$$dB = -10\log(\exp(N\sigma_a L)) = 4.343 N\sigma_a L \tag{3-3}$$

The value of N can be written as

$$N = \frac{dB_{\text{measured}}}{4.343\sigma_a L} \tag{3-4}$$

After establishing interferometer sensitivity via either of the techniques described, a time record of the measured attenuation can be used to determine transient local concentration.

---

[3] Radar scattering and absorption data from numerous other (unrelated) dissemination tests suggest that a significant number of particles actually consist of two or more fibers.

For the interferometers constructed for this experiment, the path length L used in the Beer's law calculation was 50 cm (see Figure 3-1). The actual physical path length was 55 cm; however, compressed air ejected from the horns to keep them clear of obstruction during immersion in the particle cloud reduced the effective aerosol path length from the actual path length. It was assumed that this effective length was 50 cm.

As mentioned earlier, mmw obscurants do not always disseminate as single fiber entities. The absorption cross section was calculated (per Reference [3]) for particles consisting of a few fibers lying in cordwood fashion, parallel to each other and aligned so that the particle length was equal to the fiber length.[4] These calculations are presented in Table 3-2. The single fiber properties used to generate the table were assumed to be 6.35 mm length, 500 Mho/cm conductivity, and 7.5 μm diameter. These properties are very typical of conventional mmw obscurants.

Table 3-2. Calculated Tumble Averaged Absorption Cross Section and Resultant Interferometer Full-Scale Sensitivity for Multiple Fiber Particles at 24 GHz

Number of Fibers per Particle	Absorption Cross Section (cm^2) per Particle	Full-Scale Concentration (bundled particles/m^3) at 0.43 dB Full-Scale Interferometer Sensitivity	Full-Scale Concentration (total fibers/m^3) at 0.43 dB Full-Scale Interferometer Sensitivity
1	0.015836	1.250×10^5	1.250×10^5
2	0.025092	0.789×10^5	1.578×10^5
3	0.028561	0.693×10^5	2.079×10^5
4	0.028889	0.685×10^5	2.740×10^5
5	0.027852	0.711×10^5	3.555×10^5
6	0.026331	0.752×10^5	4.512×10^5
7	0.023163	0.855×10^5	5.985×10^5

Shown in Figure 3-3 are numerical results for broadside absorption and total scatter cross sections for the single fiber properties just indicated. The results in this figure came from the method of moments code called *Analysis of Wire Antennas and Scatterers* (AWAS)[4]. Figure 3-3 clearly shows a significant attenuating capability at mmw frequencies. To realize this capability, a sufficient number of fibers per unit volume must be present in the cloud to interact with the incident electromagnetic field. Note that the values in Table 3-2 are tumble-averaged while the plot displays broadside results. The tumble-averaged attenuation is approximately one third the broadside (i.e., maximum) attenuation.

Rather than estimate the number of fibers per aggregate bundle in the field test, the data were reduced using the nominal situation where one particle contains one fiber. The results in Figures 3-4, 3-5, 3-6, and 3-7 are therefore based on this nominal simplified situation.[5] This approach also allows a more straightforward comparison to the results from the TDR computer simulations.

It is, however, informative to consider the impact of fiber bundles on interpreting interferometer measurements. Consider the rightmost column in Table 3-2. Even though the calculated absorption cross section decreases as a function of the number of fibers in a particle, the total concentration of fibers at full-scale (based on 0.43 dB saturation sensitivity) actually increases as a function of fibers per particle. If it is assumed that each particle in the cloud can consist of only one specific number, n, of fibers, where $n = 1, 2, 3,$ or 4, then Figure 3-8 can be constructed for Station 1. It is recognized that this assumption could be challenged since fibers in a real cloud will have distributions of both "cordwood" and "birds-nest" type of clumps, each with a variable number of fibers. However, Figure 3-8 is presented to show how one type of clumping can impact diagnostic concentration measurements.

---

[4] Reference [2] provides a detailed discussion of changes in extinction caused by clumping, and its effect on interpreting diagnostic measurements, particularly concentration.

[5] To ensure consistency among all figures in this report that show or refer to time, the "zero" time was considered to be 10:30 a.m. local time.
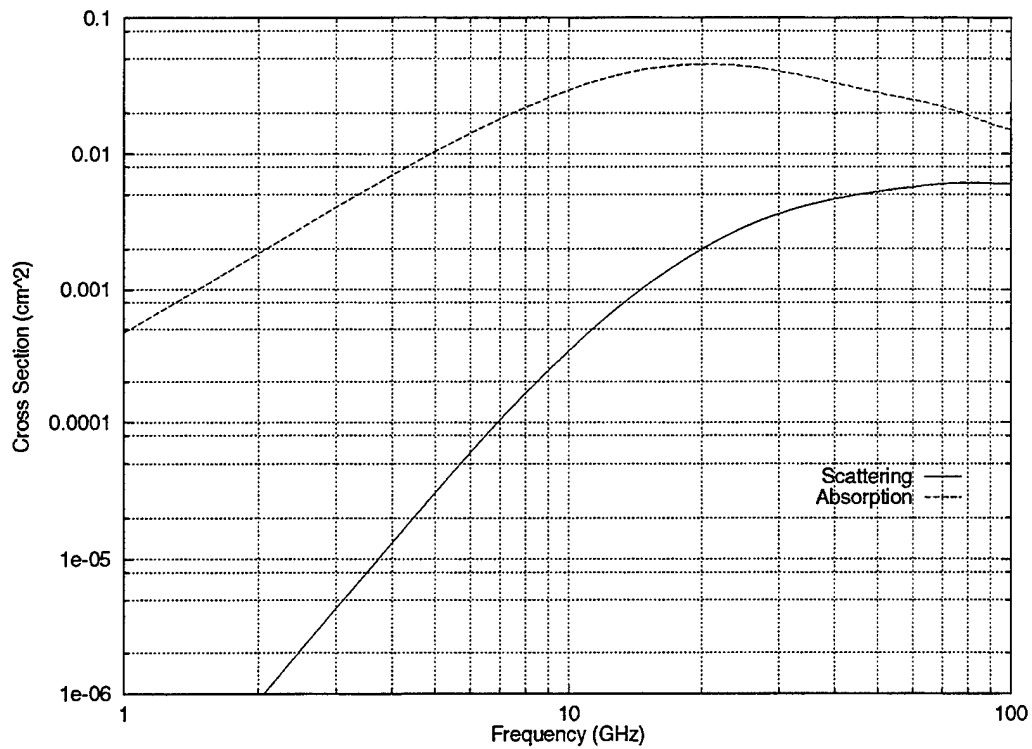
Figure 3-3. Broadside Absorption and Total Scatter Cross Sections
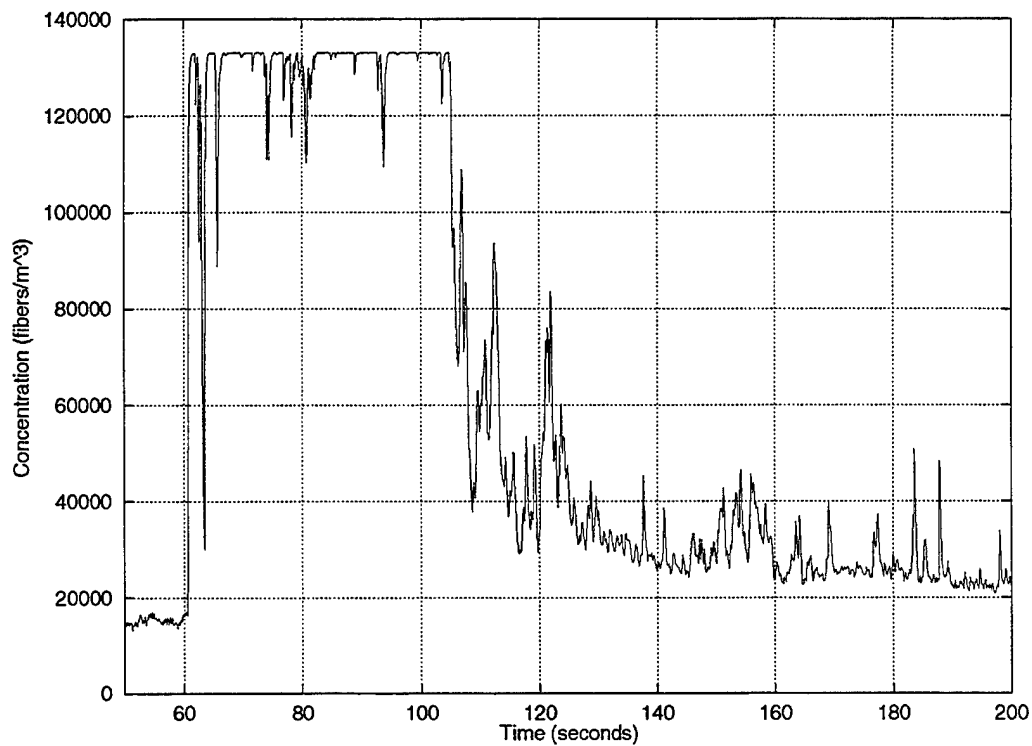
Figure 3-4. Station 1 Concentrations
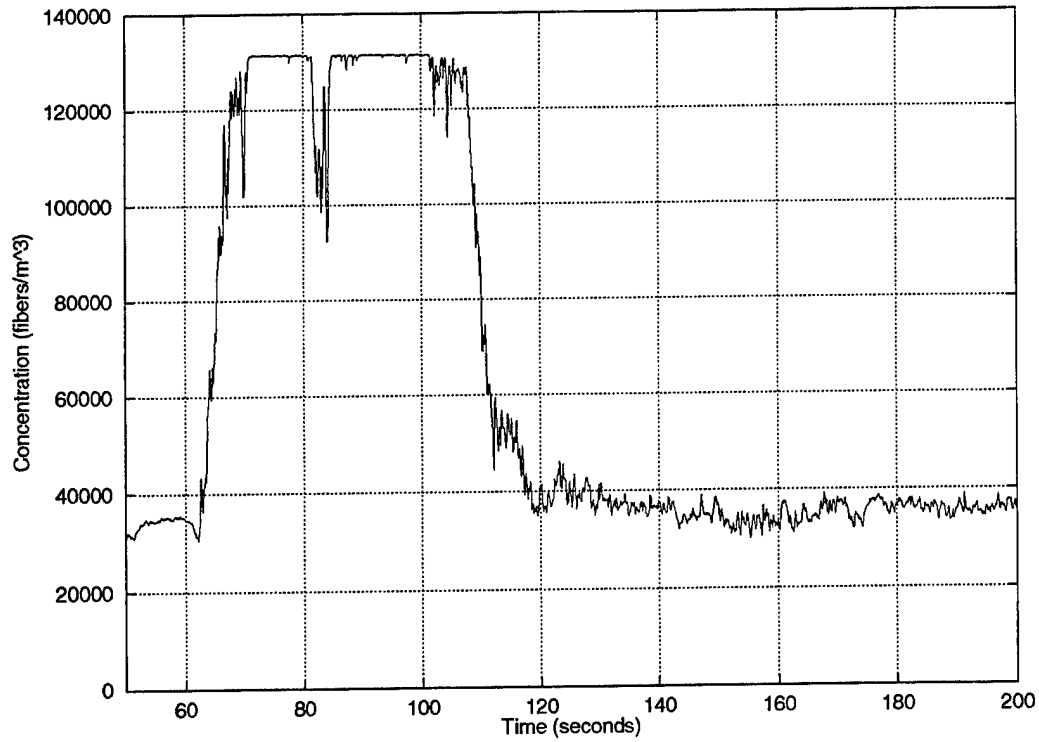
Figure 3-5.   Station 2 Concentrations
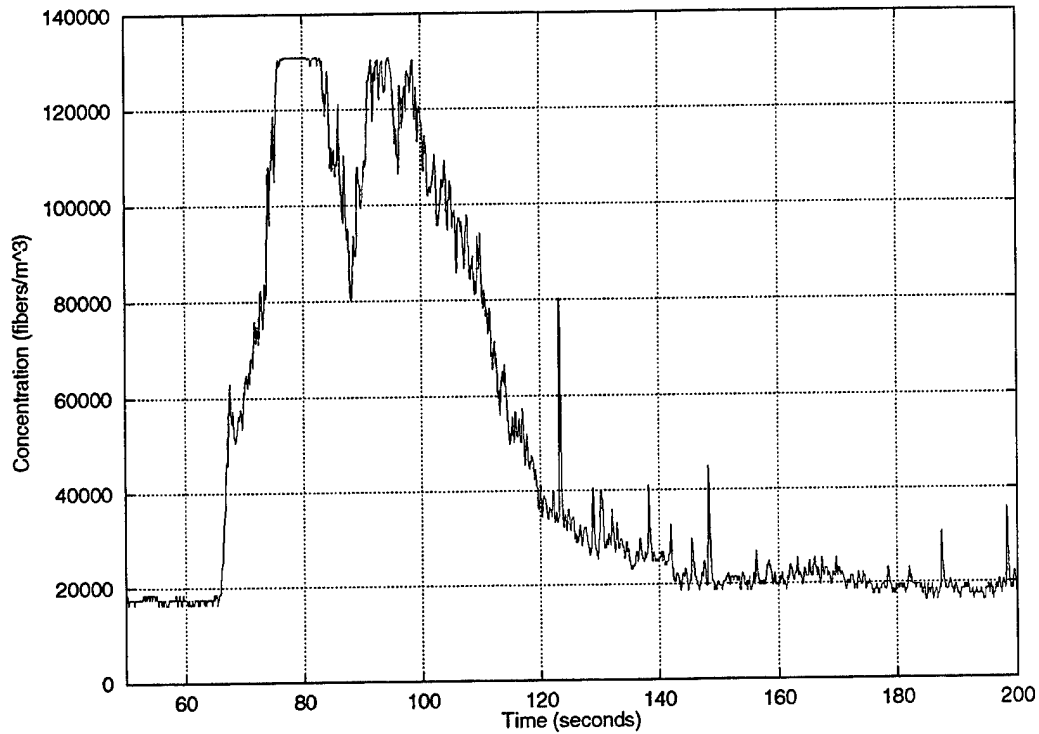
Figure 3-6.   Station 3 Concentrations
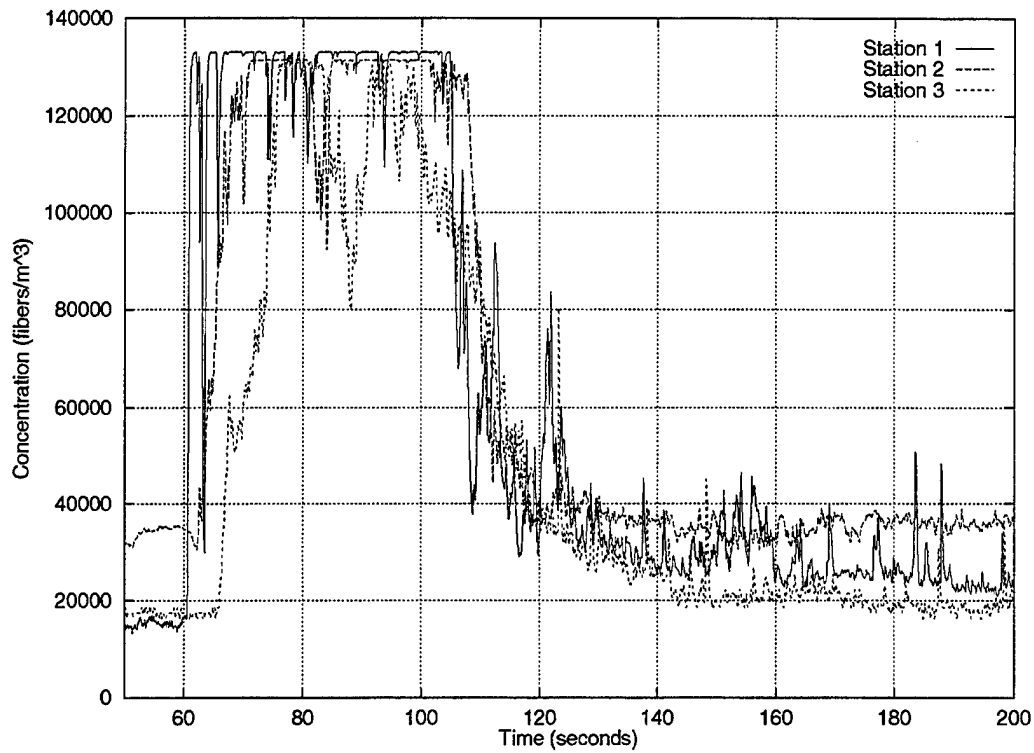
Figure 3-7.   Concentrations at Three Interferometer Stations
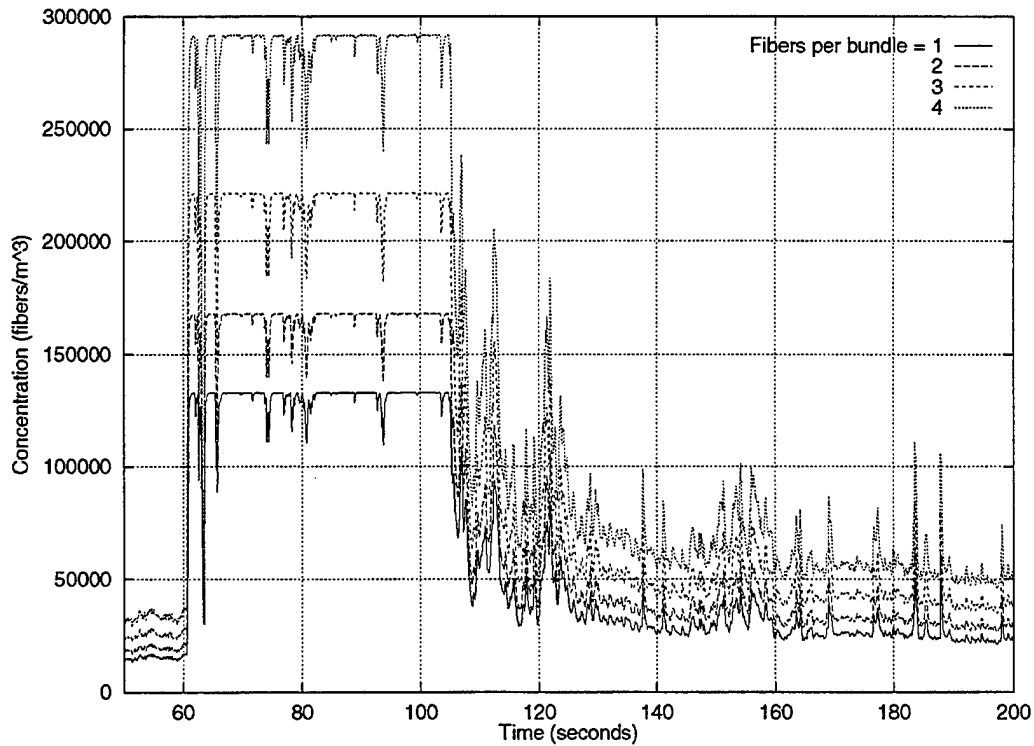
Figure 3-8.   Concentrations For Several Clumping Factors

3.5 OPERATION OF THE INTERFEROMETERS DURING THE TEST EVENTS

The interferometers were operated for only a single dissemination test. Concentration data from interferometers 1, 2, and 3 are shown individually in Figures 3-4, 3-5, and 3-6. Figure 3-7 shows all three locations on the same graph. Note that the output from stations 1 and 2 clearly became saturated and did not capture the maximum concentrations during the event. However, the interferometer at station 3 remained below saturation for most of the measurement event. Observation of Figure 3-7 shows a delay in concentration response consistent with the geometry of stations 1, 2, and 3. This figure also shows a clear reduction in concentration at station 3. Had a filter been in the duct, then reduction would have been much more pronounced. As shown in Figure 3-7, the concentration measurement threshold for stations 1, 2, and 3 were respectively, 1.5×10^4, 3.5×10^4, and 1.8×10^4 fibers/m^3. Technical improvements to these interferometer prototypes would likely increase the sensitivity so that a concentration as low as 1×10^3 fibers/m^3 might be detected. Filtration of the fiber laden air could reduce the concentration to the order of 1×10^2 fibers/m^3 or less. For very low concentrations like these, a different sensor type is needed.

In retrospect, the sensitivity of all the interferometers should have been set somewhat lower so that the probability of output saturation would have been lowered. The original sensitivity setting was chosen based on assumptions that were not upheld in the actual test. Both the dissemination efficiency of the cloud sources and the wind speed were higher than expected. Hence, not as much material fell out of the cloud onto the ground during its transport from the source locations to the measurement points. Because of time constraints, digital modeling of the transport and diffusion of the cloud was not done until after the test.

4 PREDICTIVE TDR CALCULATIONS

4.1 TDR MODEL

Computational estimates (predictions) of the concentrations were made after the physical tests via use of the TDR computer code. TDR combines a pair of wind models, *High Resolution Wind* (HRW) and *Winds on Critical Streamline Surfaces* (WOCSS), with a transport and diffusion model, *Simulation of Aerosol Behavior in Realistic Environments* (SABRE), which was developed from the radiative transfer model, *Combined Obscuration Model for Battlefield Induced Contaminants* (COMBIC), to calculate the transport, diffusion, and radiance of obscurants emitted by stationary sources (see References [5, 6, 7, 8]). The sources may be instantaneous or continuous and may start at different times. Measured wind and meteorological data in the vicinity of the source deployment are used to calculate a spatially variable three-dimensional wind field, taking the terrain, surface conditions, and atmospheric conditions into account. For a particular run of the model, TDR can use the predicted wind field from either HRW or WOCSS. The transport and diffusion of the aerosol is then calculated using a Gaussian plume and puff methodology. At specified points of interest, concentration, deposition, and exposure are estimated based on the fall velocity, ground reflection, and rate of diffusion of the obscurants. One part of the TDR code (Phase II) also calculates line-of-sight transmission and radiance between sets of arbitrary spatial point pairs, thereby providing important information that can be used to assess the impact of airborne obscurants on sensor and weapon system performance.

These studies were conducted with interim TDR-3.2 (see Reference [9]), which incorporates several significant changes from the latest distributed version of TDR, v3.1 (see Reference [10]). TDR-3.2 incorporates the COMBIC92 (see Reference [11]) method of estimating the Pasquill stability of the atmospheric boundary layer, and employs the COMBIC92 methods for development of the puff and plume diffusion rates (i.e., the rate of growth of the Gaussian standard deviations (σs) of the clouds). The principle effect of these changes is to provide for a smooth variation in behavior from unstable to stable atmospheric conditions. TDR-3.1 provided just three rates of cloud σ growth corresponding to stable, neutral, and unstable atmospheric conditions. TDR-3.2 also incorporates novel models for representing the propagation and growth of Gaussian puffs and plumes consisting of solid particulate aerosols. These models preserve the highest fidelity in physical assumptions and lead to more realistic quantitative predictions. In particular, conservation of source mass was maintained for all situations involving ground deposition.

4.2 TDR INPUTS AND ASSUMPTIONS

4.2.1 Source Scenario Inputs

The situation that was simulated is as follows: The 216 sources were randomly distributed within a circle of 220-m diameter. The sources are modeled as disseminating from a height[6] above ground of 4 m. At this starting height, the resultant mmw screening cloud has very strong attenuating capability against low slant angle sensors while still maintaining good blocking performance against top-down viewing sensors. As indicated in Figure 2-1, the center of the distribution circle was 32 m west and 5 m north of the center of the range grid. Hence, the line-of-sight distance between the center of the distribution circle and the interferometer at station 1 was 176.4 m. Each source is assumed to be comprised of 284 gm of mmw

---

[6] Although the initial height of the sources was input as 3 m (see Appendix B where zs = 3.0 for all sources), TDR internally adjusted the initial height as follows:

$$\text{initial source height} = z_s + \left[\frac{1}{3} \left(\frac{\sigma_{x_0} + \sigma_{y_0}}{2} \right) \right]$$

where σ_{x_0} and σ_{y_0} are the initial source burst sigmas, both set to 3 m. The term in brackets is called the buoyancy radius. With these values, the initial source height becomes 4 m.

obscurants. The particles are assumed to be 6.35 mm in length, to be 7.5 μm in diameter, and to have a density of 1.8 gm/cm^3.

With these physical attributes, the number of whole fibers in each source can be calculated as 562×10^6. Each source is modeled as an instantaneously generated puff with no generator-produced residual momentum (i.e., the puff transport is due only to gravity and wind).

The distributions used for these simulations were created with the EMACS (the extensible, customizable, self-documenting real-time display editor) Calculator (an advanced desk calculator and mathematical tool that runs as part of the GNU[7] EMACS environment). A vector of length 216 was formed having values of 360.0 in each slot. This was then used with the uniform random number generator function to produce a uniform random distribution over 0–360 deg. A second vector of length 216 was formed with initial values of 110^2 (12,100). This was used with the uniform random number generator function to produce a uniform distribution over this range. The square root of each of these values was then taken. Together these produced a vector of random angles, which in the limit would have a uniform distribution, and a vector of radii, which in the limit would be uniformly distributed over r^2, together allowing a uniform (in the limit) distribution over the area of the circle when employed as (mag,arg) pairs. This was explicitly accomplished by forming a sine vector and a cosine vector for the argument vector and multiplying each by the magnitude vector, producing a pair of vectors representing the crosswind and downwind locations of the sources. Two distributions were used for these exercises, presented in Figures 4-1 and 4-2. For this report, Distribution 1 has been considered as the nominal situation. Within Figures 4-1 and 4-2, the distribution centers are at coordinate (110,120). The nominal wind direction is shown as overlaying the y=120 m line. Since the location of interferometer station is 176.4 m from the center of a distribution center, the location of this same point in the wind flow grid is therefore at (286.4,120). The interferometer detector center was 1.5 m above the ground plane so this is the elevation used for all simulation results.

Shown in Appendices A, B, C, and D are listings of the full set of input parameters that create the nominal TDR predictions, when TDR-3.2 is used. Appendix A presents the inputs for the smooth terrain wind field generation module, which runs within TDR as Phase '-1'. Appendix B presents the inputs to TDR Phase I. This model uses a wind field generated by some prior operation (in this case the smooth field generator) and the inputs to compute time histories for each of the defined sources. In this particular case there are 216 sources (nsorc=216) of identical type (source_type=1,1,...,1,). Locations of the 216 sources were generated randomly in x and y with a constant vertical location. The remaining inputs provide information defining the characteristics of the individual sources. Appendix C presents the inputs to TDR Phase II, which computes line-of-sight attenuation and radiance, and which will be exploited in Section 7. Phase II inputs include an array of numbers (bgnsrc) which defines the initiation time for the sources. Appendix D presents the inputs to TDR Phase III, which computes the concentration, deposition, and exposure for the simulation. Within the inputs to Phase III is a repeated specification of the beginning time for each source (bgnsrc).[8] The other inputs to Phase III define the output locations and times for the simulation.

The placement of the sources has a noticeable effect on the outcome of the simulation. Figure 4-3 shows concentrations at station 1 as a function of source distribution with all other parameters held at the nominal values.

---

[7] GNU is the trade name of the Free Software Foundation, which supports and develops free software. Additional information, and the software itself, is available by ftp from prep.ai.mit.edu

[8] Note that Phase II and Phase III of TDR are completely independent, other than their common reliance on the results of Phase I.
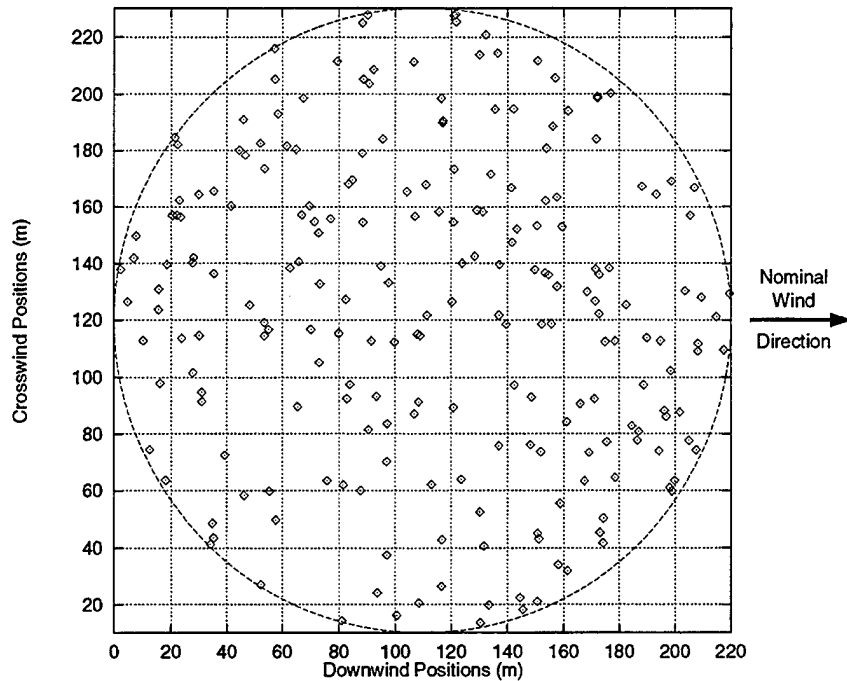
**Figure 4-1. Source Locations
Distribution 1**
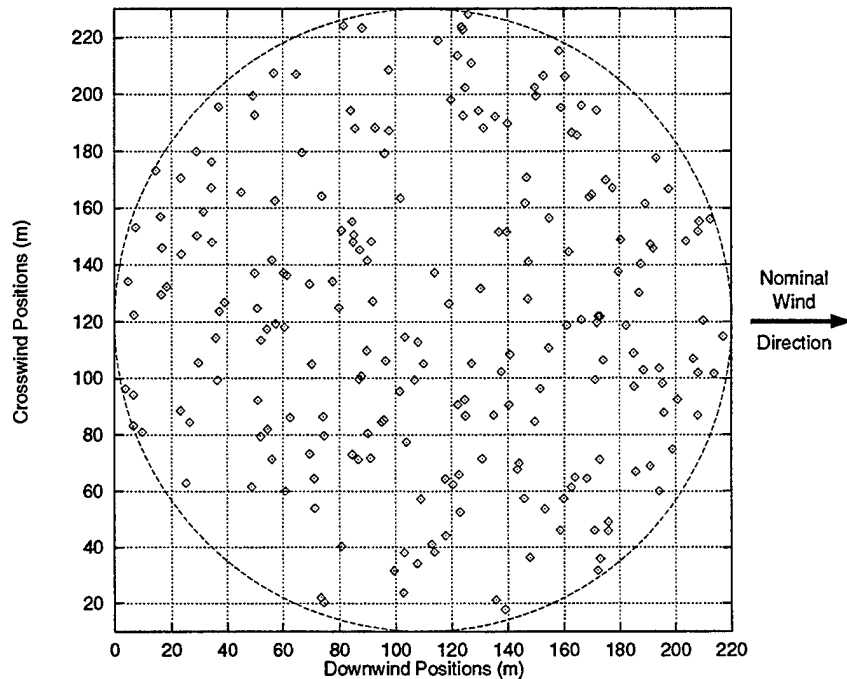
**Figure 4-2. Source Locations
Distribution 2**

4.2.2 Boundary Layer Atmospheric Model

In general, TDR requires that a wind field be provided for the area of interest. As indicated earlier, two options within the TDR model framework (HRW and WOCSS) are available for generation of wind fields influenced by terrain. If a uniform wind field is desired, then the smooth option may be run within TDR to
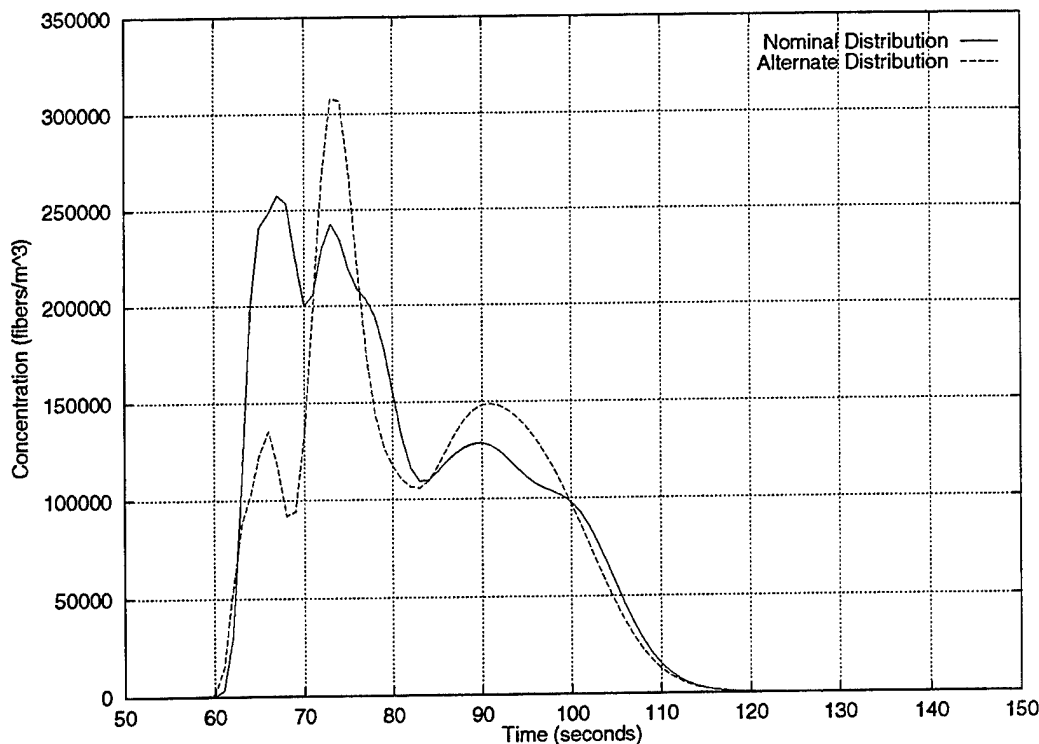
Figure 4-3. Distribution Variation Effect on Concentration History

generate a uniform wind. By uniform wind field, it is meant that the wind at a given height has the same speed and direction everywhere. The speed is a function of height satisfying the equation $u = \bar{u} * (z/z_{ref})^p$, where p is the power law exponent and z_{ref} is the reference height of the wind speed measurement. In the case of the smooth option in TDR, this height is internally constrained to be 10 m.

Given the nature of the area over which the test was conducted, a smooth terrain and uniform wind field were chosen for the simulations. Several meteorology stations were present on the test site so relatively good data was available on wind speed and direction. A time history of the wind speed and direction indicate a variation during the test of around ±30 percent on wind speed and ±20 deg on direction. Wind data was gathered at several stations of different heights.

In TDR-3.2, the wind field model uses the COMBIC92 routines for estimation of the Pasquill stability of the atmosphere. The values computed are not directly output, but the algorithm now produces a smooth transition from stable through neutral to unstable. A previously documented version (TDR-3.1) used an algorithm that resulted in one of three discrete values for stability. The dominant input parameters to the wind field generator that drive the stability computation are provided in Table 4-1. A complete listing of the inputs to the wind field generator for the nominal case is provided in Appendix A. Descriptions of the available input variables and their default values are provided in Reference [10]. Presented in Table 4-1 are several of the more important input parameters to the smooth wind field module, along with an explanation and background for the particular values chosen as nominal inputs to TDR.

The values provided in Table 4-1 require some elaboration. The 5.98 m/s wind speed is an average of the readings from the several meteorological stations taking observations at different heights. This was arbitrarily chosen as the nominal 10-m wind speed input to smooth. The power law relationship then gives a wind speed of 5.21 m/s at the 4-m dissemination height, and a speed of 4.50 m/s at the 1.5-m sensor height. The roughness length of 0.01 m was chosen from the table of roughness lengths on pages 59 and 60 of Reference [11]. No entry exactly describes the test site, but values from 0.01 m to 0.1 m would be acceptable. Using 0.01 m in the equation for friction velocity gives a result of 0.346 m/s when a 10-m reference height is used. Using a roughness length of 0.01 m and a chosen reference height of 1 m results in the 0.519 m/s that

Table 4-1. Smooth Terrain Atmospheric Module Inputs

Variable	Value	Usage and Explanation
ubar	5.98	Wind velocity (m/s) in x-direction. This is one component of a vector wind; the other component is vbar. This coordinate system was oriented such that the nominal wind was along the x-axis. The average value of 5.98 m/s was used for all the simulations related to this test. For the purpose of computing the friction velocity, and Pasquill Class in Figure 4-4, this value was taken to be at 1 m height. Elsewhere this value is associated with a 10 m height.
z0bar	0.01	A function of the height of the surface roughness and the density of that roughness. Is approximately the height at which the logarithmic velocity profile goes to zero. In this case there was a quite flat medium gravel surface over most of the area, with a slightly raised very flat area for the actual test.
ustbar	0.519	Friction velocity. This has no explicit physical representation, but is related to the power law wind speed and is indicative of the attachment of the boundary layer to the terrain surface. To wit, a very low value of surface roughness causes the calculations to be inordinately sensitive to surface heat flux. Friction velocity is computed by the equation $\bar{u}^* = 0.40|\bar{u}|/\ln(z_1/\bar{z}_0)$ where z_1 is the height of the wind speed measurement and $\bar{z}_0$ is the surface roughness length. This is a scalar value.
hs	150.0	Surface heat flux (W/m²). This is a measure of the conductive heat transfer from the terrain surface to the air and provides an indication of the temperature gradients that will be found in the boundary layer. Positive values indicate that heat is being transferred from the ground into the air, creating an unstable thermal gradient, while a negative value indicates that heat is being transferred to the ground from the air, cooling the air and producing a stable thermal gradient. Running COMBIC with inputs appropriate to the location, time, and date of the test produced a surface heat flux range (variations due to various assumptions) of 140–185. Dr. Al Astling of Dugway indicated that measured values for similar conditions were from 150–200. 150.0 was used as a representative value.

was used. The friction velocity term $\bar{u}^*$ is not related to a directly measurable quantity but is indicative of the turbulent mixing at the surface. The sensitivity of the boundary layer stability to heat flux is inversely related to the ratio $\bar{u}^*/\bar{u}$. The above variations in $\bar{u}^*$ have a relatively modest impact on the downwind nominal obscurant concentration predictions.

These nominal inputs result in a moderately unstable atmosphere, which implies increased mixing when compared to a neutral or stable atmosphere. Simulations with different atmospheric conditions showed marked differences in the nature of the solutions. Figure 4-4 shows the difference that occurs with a change from a stable atmosphere to neutral to unstable. This is indicative of the importance of correct assessment of the meteorological conditions in a simulation of this type.

The reason for this behavior is that a stable atmosphere has relatively mild mixing. Atmospheric mixing is driven by vertical flow produced by negative temperature gradients near the surface. Local surface heating of the air causes expansion of the air, which results in a reduction in density, causing increased buoyancy, which produces a tendency for the air to rise. This produces convection currents (which tend to be locally unpredictable) that produce vertical and horizontal flows in local spaces. These flows are collectively modeled by TDR as faster expansion of the cloud. In Figure 4-4 this is manifested by smoother contours (from the increased horizontal mixing), and an overall lower concentration level (from the increased vertical mixing) for the unstable conditions.
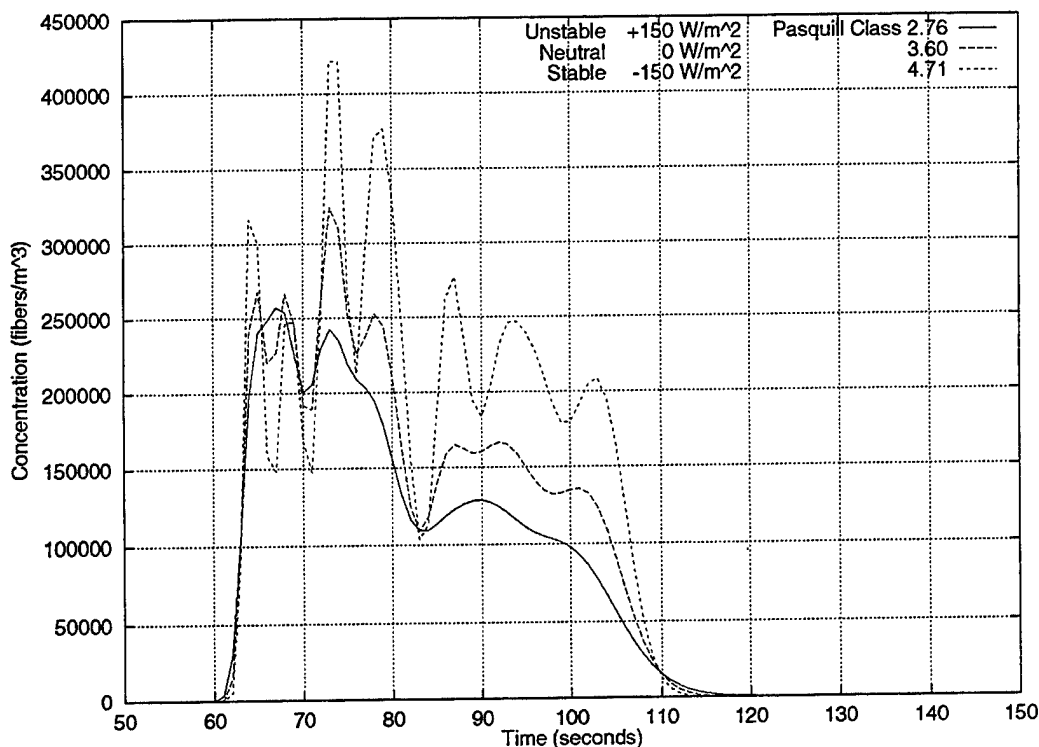
Figure 4-4. Atmospheric Stability Variation Effect on Concentration History

4.2.3 Wind Direction Variation Effects

During the period lasting from source initialization through passage of all puffs past station 1, the wind was observed to vary in both speed and direction. In particular, the directional variation was on the order of ±5 deg. The TDR model does not have the capability to model time-varying winds, but, as the wind variations are not locally predictable, this capability would not add benefit to a predictive tool. The TDR model was run for a plus and minus 5 deg variation in wind direction from the nominal. Figure 4-5 is a comparison of concentration predictions for station 1 for these directional perturbations. Note the similarity in the effect of relatively small directional changes to the effects of completely different distributions as shown in Figure 4-3. Small changes in wind variation can produce essentially the same effect as differing source distributions.

It can be seen from these comparisons that small changes in the angle produce quite significant variations in the concentrations at the initial encounter with the cloud, and smaller variations at the trailing edge. The reason for this is that the puffs that reach the target point first have had less time to develop and are therefore more sharply defined.
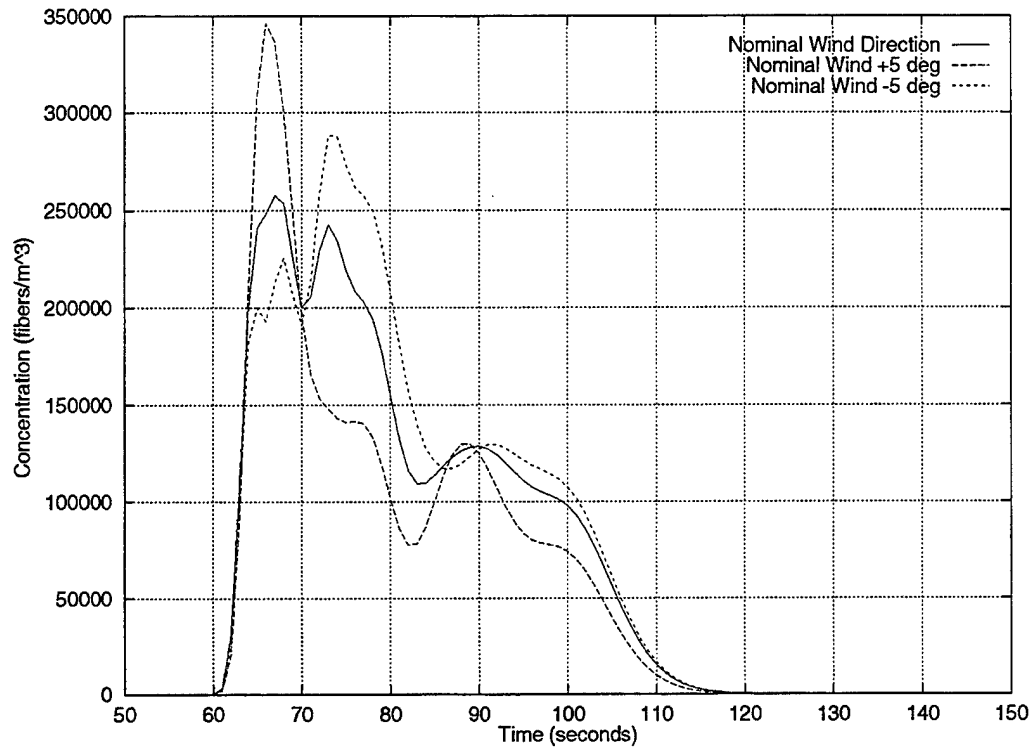
Figure 4-5. Wind Direction Variation Effect on Concentration History

THIS PAGE INTENTIONALLY LEFT BLANK

5 COMPARISON OF TDR PREDICTIONS TO FIELD TEST INTERFEROMETER RESULTS

Shown in Figure 5-1 is the comparison of the nominal TDR prediction to the interferometer results at station 1. The measurements in Figure 5-1 are based on the assumption of one fiber per bundle. Figure 3-8 presents projected measured concentrations based on other clumping factors. The principal difficulty with a correlation between the simulation and the experimental data is the saturation limit of the interferometer. Another apparent disparity is that the interferometer does not drop back to the initial zero condition. This has been attributed to three effects: 1) heating of the unit from use and from sitting in the sun during the test, 2) deposition of material within the interferometer test section, and 3) material that had been deposited on the ground being re-aerosolized by the wind and going through the interferometer well after the primary cloud had passed. The first two effects are calibration issues for the test equipment. The third effect is a dynamic non-linear turbulent boundary flow problem that the TDR code does not handle, nor is there any reasonable way to model this type of situation within the auspices of a Gaussian formulation.
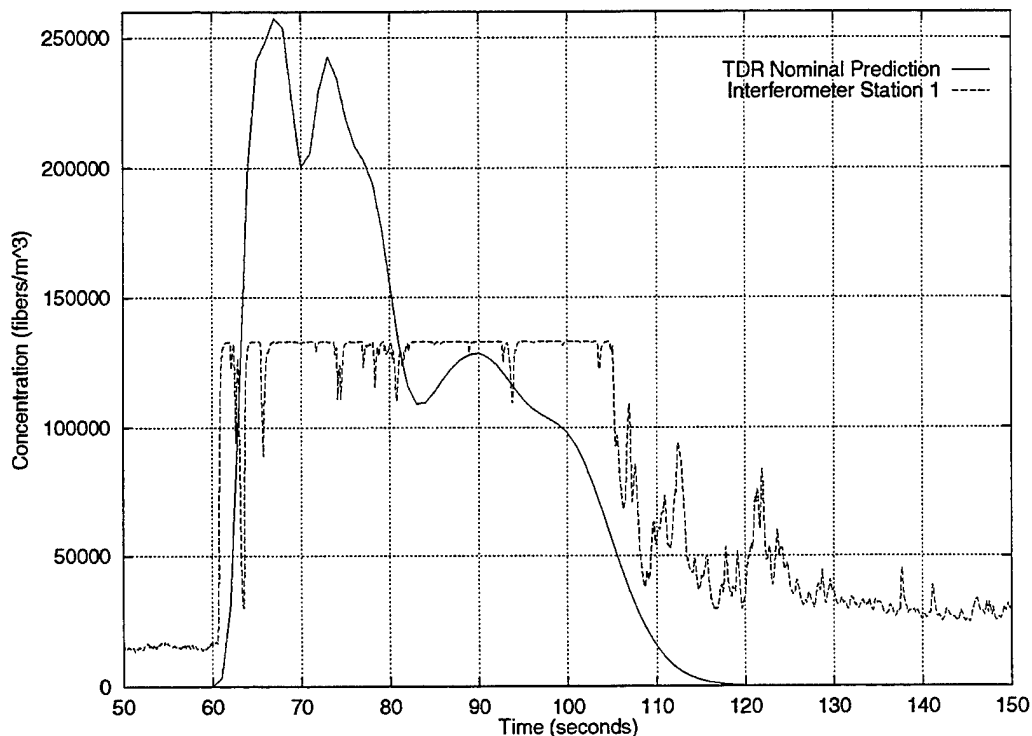
Figure 5-1.   **Comparison of Nominal TDR Prediction to Interferometer Station 1 Data**

If the interest is in contamination by the material (e.g., risk to personnel via inhalation) rather than the obscuration effect produced by the material, the total exposure calculated as material concentration integrated over time will be the more important measure. Figure 5-2 presents the time integral exposure at the observation point for the nominal random source distribution at the three wind directions as shown in Figure 4-5, along with a computation of the experimental exposure as based on measured data. The measured data were modified by subtracting the initial noise floor as seen in Figures 3-4 and 5-1 from the remaining values. This has the effect of reducing the slope of the exposure along the saturation line, but provides a more realistic estimate of the exposure growth after the cloud has passed.
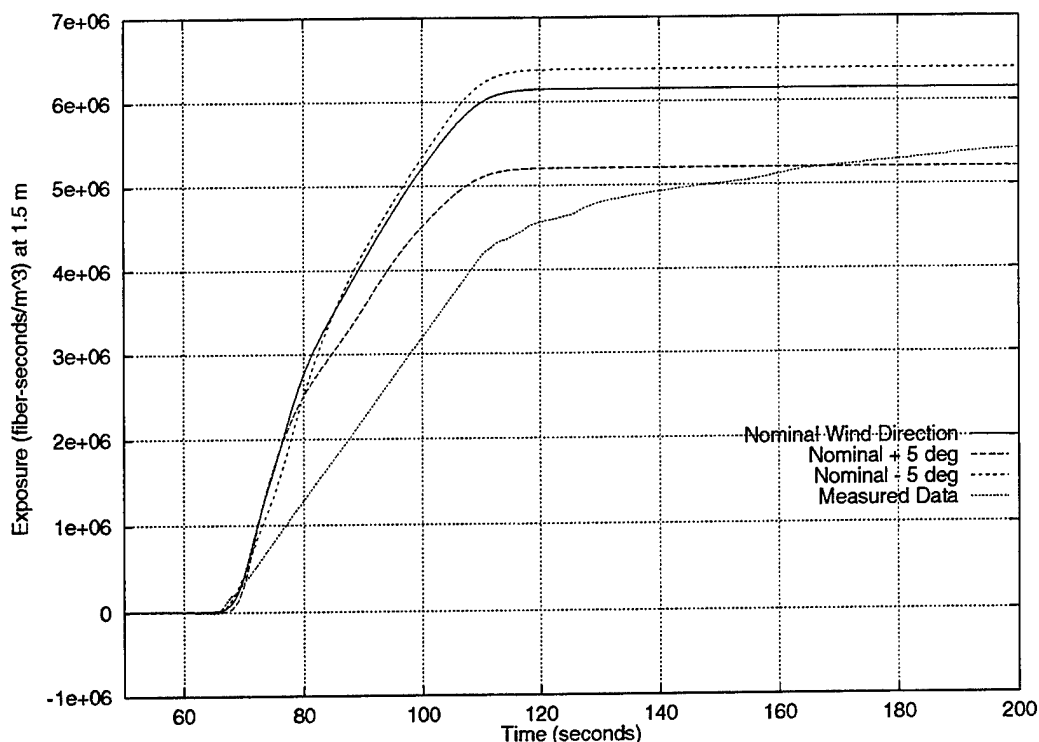
Figure 5-2. Exposure for First Distribution

Note that the final exposure as simulated by TDR varies by roughly 20 percent depending on the exact distribution of the sources and the exact wind angle. This seems to be consistent with experimental results, which may vary by factors of 2 or 3 (or sometimes even more) from one similar event to the next. Considerable insight into the dynamics of a multiple source release event like that represented in Figure 4-1 can be gained if concentrations near the center of the distribution are observed. Although no interferometer measurements were made at these locations during the field test, it is informative to analyze TDR predictions relative to this geometry. With respect to Figure 4-1, consider what interferometer measurements may have looked like if they had been made at locations $(123, 122)$, $(123, 123)$, $(123, 124)$, $(123, 132)$, and $(123, 142)$. Recall that the center of the distribution is at $(110, 120)$. Figure 5-3 presents TDR predictions for these five hypothetical points, with all other inputs held nominal. Note that Figure 5-3 starts at 50 seconds after 10:30 local time. Because the source puffs are now located very close to the pseudo-measurement points, large TDR concentration results begin much earlier than the measurement and TDR prediction for station 1. Also, because the puffs are not spatially developed early in the event, the concentrations at the pseudo-measurement points show severe magnitude variation until about 68 seconds. By this time the upstream puffs have spatially bloomed and coalesced so that the concentrations at the observation points do not vary significantly. Contrast the predictions in Figure 5-3 with the results in Figure 5-1 for station 1. The choice of measurement location can have a very large impact on the necessary dynamic range for the measurement instrument.

As a final observation on the dynamics of the five pseudo-measurement points, consider the TDR predictions for exposure for these locations as shown in Figure 5-4. None of the exposures for the five locations exceed about 5×10^6 fiber-seconds/m^3. Contrast these predictions with the TDR results in Figure 5-2, which relate to station 1. In Figure 5-2, all three simulated exposures are in excess of 5×10^6 fiber-seconds/m^3. Recall that interferometer station 1 was 176.4 m from the center of the distribution circle. The five locations in Figures 5-3 and 5-4 are, respectively, 13.2., 13.3, 13.6, 17.7, and 25.6 m from the center of Distribution 1. Even though these five locations are all significantly closer to the center of the source distribution, the location of interferometer 1 yields TDR exposure results that are higher. If contamination by material is the interest, then points well outside the initial source distribution may have higher exposures. TDR predictions can be used to help quantify contamination questions such as inhalation risk to personnel.
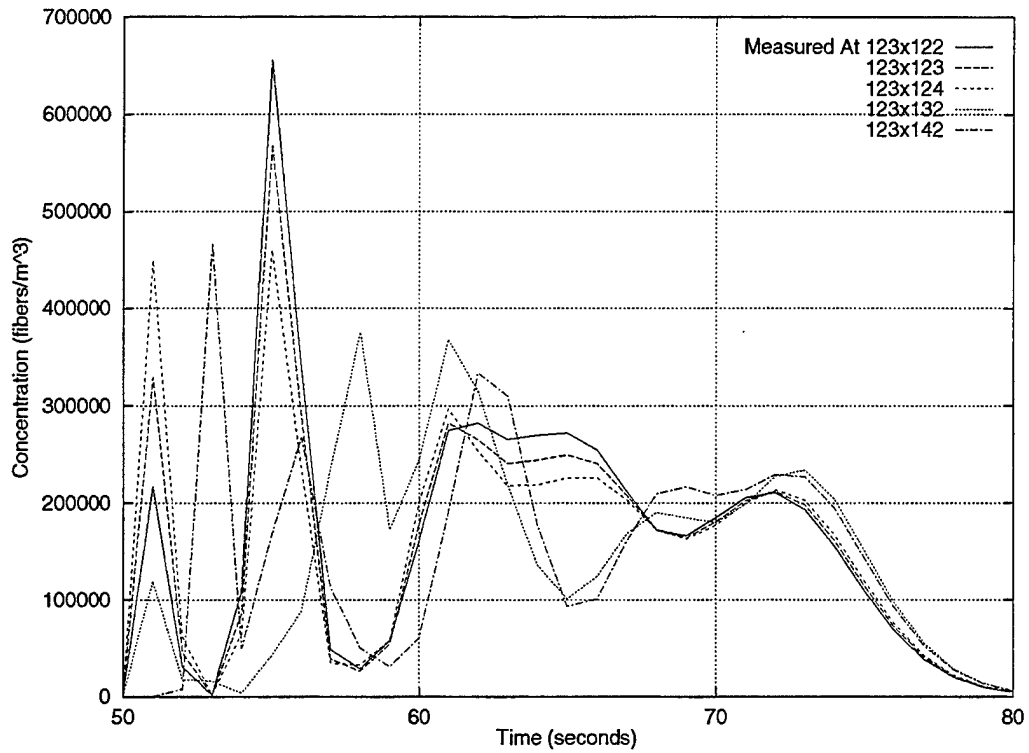
Figure 5-3. Concentration at Location Near Center
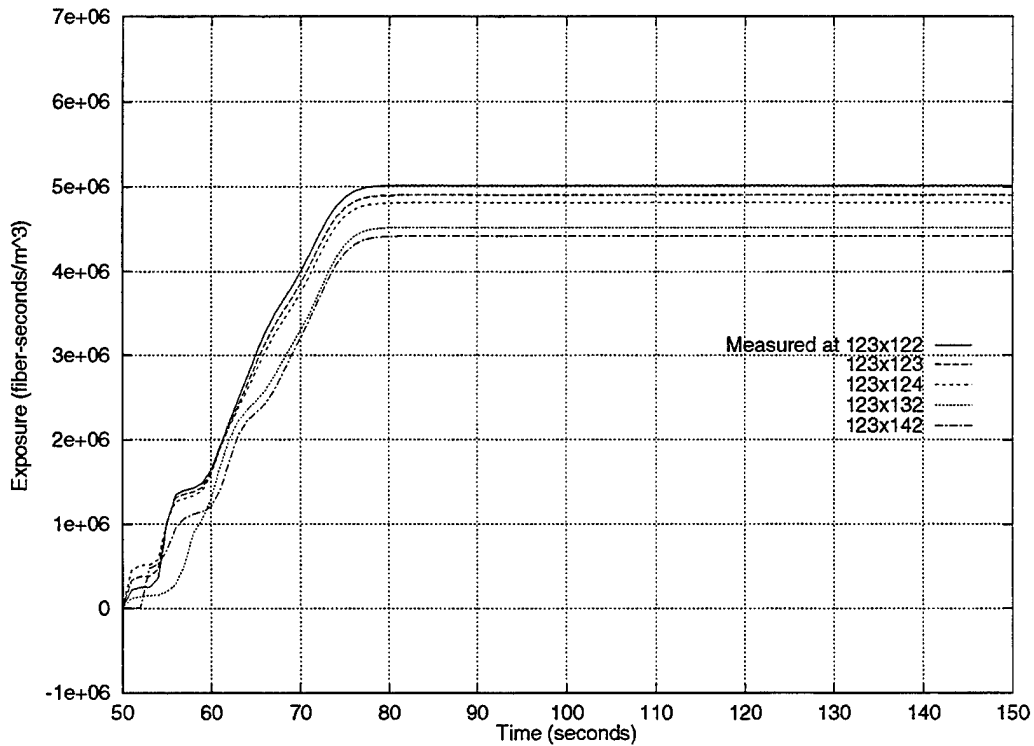
Figure 5-4. Exposure at Location Near Center

THIS PAGE INTENTIONALLY LEFT BLANK

6 AREA CONCENTRATION, EXPOSURE, AND DEPOSITION CALCULATIONS WITH TDR

Sections 4 and 5 have emphasized the ability of the TDR model to make reasonable predictions of local or point concentration. TDR has the additional capability of computing the concentration, exposure, and deposition over a grid covering an area of interest. Producing plots of concentration over an area can give additional insight into the complex phenomenology at work in the event. For source distribution 1 and nominal inputs for all variables, Figure 6-1 depicts gray-scale plots of the concentration, exposure, and deposition at 54 seconds, which is immediately after the last source initiation, and then at 30-second intervals beginning at 80 seconds into the event timing. Concentration and exposure are relevant to a plane 1.5 m above the ground. Each subgraph of the mosaic has dimensions of 606 m downwind (to right) × 366 m crosswind. The grid resolution for this exercise was 6 m in both directions. The center of the initial source distribution is centered in the crosswind direction and is 113 m from the upwind edge. Station 1 is 176.4 m downwind of the center of the distribution, making it 289.4 m from the upwind edge of the grid. Shown in the 200-second concentration plot is the relative position of station 1.

Each of the plots in Figure 6-1 is normalized with respect to the maximum value within that plot, as presented in Table 6-1. They are therefore not quantitatively comparable from one time to the next. The individual plots of Figure 6-1, and the combined mosaic, were produced using components of the Khoros 1.0 Software Package[12].[9] The TDR Phase III output was processed by a custom application to convert the one ASCII output file to several Khoros Viff format graphics files.

Table 6-1. Maximum Concentration, Exposure, and Deposition at Several Times

Time (seconds)	Concentration (fibers/m^3)	Exposure (fiber-seconds/m^3)	Deposition (fibers/m^2)
54	1307000	2.578×10^6	2.550×10^6
80	237000	8.768×10^6	2.832×10^6
110	107100	9.867×10^6	2.882×10^6
140	68320	9.867×10^6	2.882×10^6
170	6649	9.867×10^6	2.882×10^6
200	5.856	9.867×10^6	2.882×10^6

Before normalizing to create the individual plots within Figure 6-1, the raw TDR data plots allow quantitative determination of concentration, exposure, and deposition at any point within the computation grid. These values are available from the Khoros image display software by moving the cursor over the raw image. The original raw data images contain more detailed information than conventional contour plots.

Table 6-1 in conjunction with Figure 6-1 demonstrates that the concentration is initially very high but diffuses and moves downwind reasonably rapidly, and by 200 seconds the cloud is essentially off the grid. The exposure and deposition both reach maximum values by 110 seconds as the bulk of the cloud has moved away from the primary source initiation area. It is noteworthy that the maximum exposure and deposition both occur just at the downwind side of the initial distribution area.

---

[9] Khoros is an Open Software Package developed by the University of New Mexico and Khoral Research, Inc. Further information about the Khoros system, and the system itself, may be obtained by ftp from ftp.khoros.unm.edu.
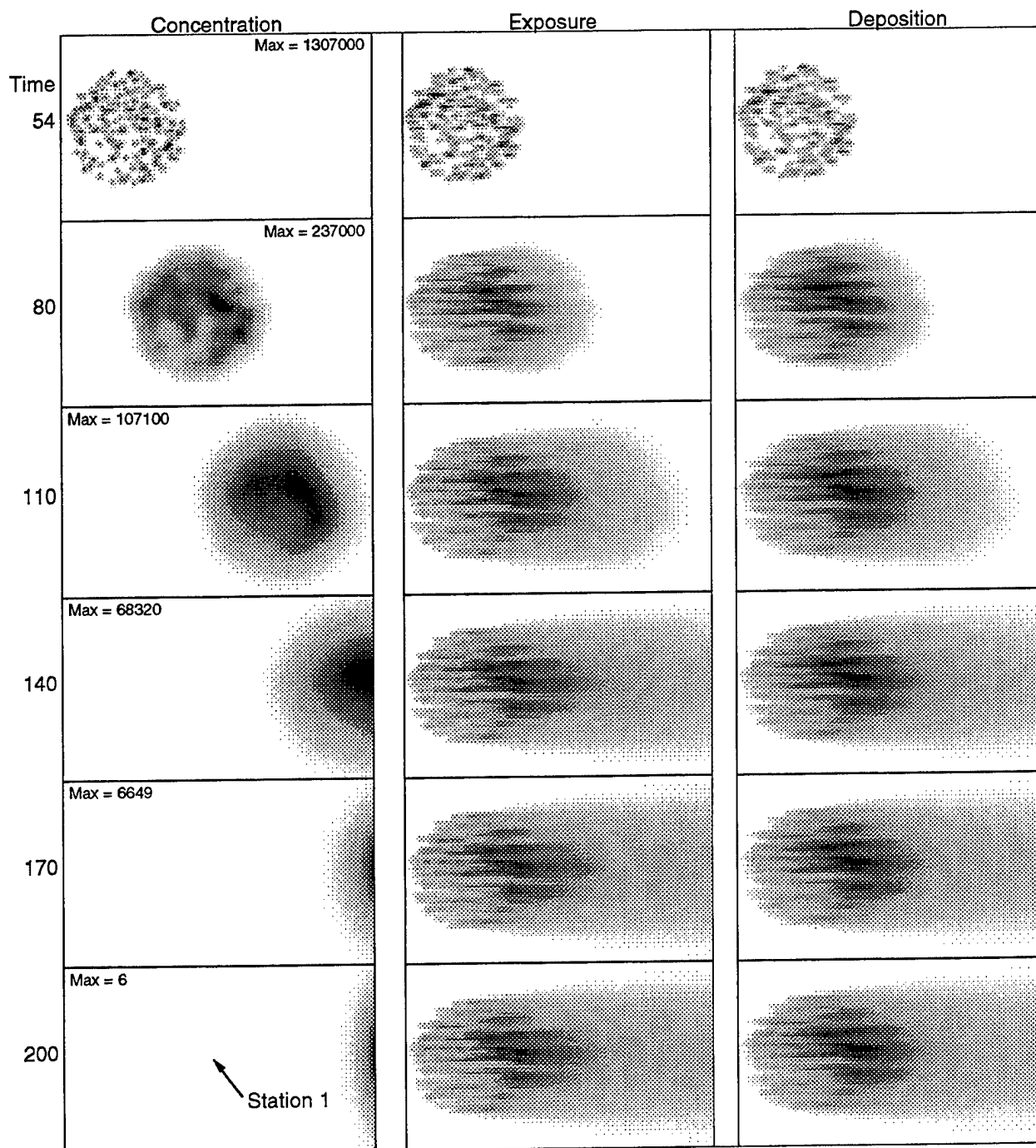
Figure 6-1. Composite of Concentration, Exposure, and Deposition Over Time

It should be noted that TDR computes concentration, exposure, and deposition at points on a grid. While the discussion at times is of average values of concentration and such, what is really being discussed is average values over a finite set of points. The assumption is that the values that are computed are representative values over an area around the computation points. Table 6-2 presents a table of integrated values over the entire grid area. In this example, the grid contains 101 downwind by 61 crosswind points, equaling a total of 6161 points. The area *enclosed* by the grid (that is, between the first and last grid points) is 216,000 m². In constructing Table 6-2, each of the 6161 individual grid values was multiplied by 36 m² (6 m × 6 m grid spacing). This implies that the relevant area is 221,796 m² (366 m × 606 m). The

concentration values represent a count of fibers in a 1-m thick layer centered at 1.5 m height (that is, a count of fibers in the layer from 1 to 2 m height). The exposure values represent the count of fibers in this layer integrated over time. The deposition represents the total number of fibers deposited on the ground up to that time. The units are then fibers (within a 1-m layer), fiber-seconds (within a 1-m layer), and fibers for Table 6-2.

Table 6-2. Total Concentration, Exposure, and Deposition at Several Times

Time (seconds)	Concentration (fibers/m)	Exposure (fiber-seconds/m)	Deposition (fibers)
54	8.51643×10^9	2.02299×10^{10}	9.09973×10^9
80	5.54001×10^9	2.06004×10^{11}	2.48802×10^{10}
110	3.42899×10^9	3.35917×10^{11}	3.38791×10^{10}
140	1.32980×10^9	4.11926×10^{11}	3.74819×10^{10}
170	2.91832×10^7	4.25860×10^{11}	3.79916×10^{10}
200	1.81043×10^4	4.26023×10^{11}	3.79955×10^{10}

As indicated in Appendix B, the nominal input for TDR included a value of zero for the variable usurfrefa. This represents a reflection coefficient of zero for all fibers that contact the ground. Another way to view the physics implied by usurfrefa=0.0 is to say that every fiber that contacts the ground sticks on the ground. Another nominal input variable given in Appendix B that is very important to total deposition is effa. This is the dissemination efficiency of the sources and was chosen to be 0.75. This provides that only 75 percent of the source mass is assumed to become airborne and to be transported by the wind. The TDR results throughout this report address only this airborne mass and account for its presence spatially and temporally within the computation grid. Thus, Figure 6-1 and Tables 6-1, 6-2, and 6-3 are relevant only to this airborne material.

Table 6-3. Average Concentration, Exposure, and Deposition at Several Times

Time (seconds)	Average Concentration (fibers/m^3)	Average Exposure (fiber-seconds/m^3)	Average Deposition (fibers/m^2)
54	38397.58	9.121×10^4	4.103×10^4
80	24977.95	9.290×10^5	1.122×10^5
110	15460.11	1.514×10^6	1.527×10^5
140	5995.60	1.858×10^6	1.690×10^5
170	131.58	1.921×10^6	1.713×10^5
200	0.08	1.921×10^6	1.713×10^5

The total number of fibers in the 216 sources has been estimated to be 12.148×10^{10} (based on a single fiber mass of 5.0496×10^{-7} gm). With a dissemination efficiency of 0.75, the total number of tracked fibers is then 9.111×10^{10}. The total deposition at 200 seconds in Table 6-2 corresponds to 41.70 percent of the total fibers that became airborne after dissemination (or 31.28 percent of the total fibers). At 54 seconds the deposition is 9.99 percent of the airborne fibers (or 7.49 percent of the total fibers). This quantity of fibers is comprised of two independent contributions as follows: first are the fibers from the initial burst

expansion of each source[10]; second are the fibers that settle normally from each puff after its initial burst. Running TDR with no initial deposition indicates that the normal deposition over this time interval amounts to 0.732 percent of the airborne fibers, leaving 9.26 percent as initial deposition. An analysis of Gaussian statistics would show that the amount of material deposited by the initial bursts, with the height at $4/3\,\sigma_z$, would be approximately 9.12 percent. It has been shown elsewhere (see Reference [9]) that a difference in deposited mass calculations may arise when discrete grid point integration is compared to the closed form ideal Gaussian solution. In general, the difference between the two approaches to the prediction of deposited mass would be greater when the grid is coarse relative to the initial σ_x and σ_y values. As indicated earlier, the two calculations differ by only about 0.14 percent of total mass, or 1.53 percent relative. The closeness of the comparison is heavily influenced by the relatively large number of randomly placed sources that enter into the discrete integration at the many grid intersections.

TDR computes a deposition from the initial expansion of the puff. This is assumed to be a radial expansion maintaining a Gaussian distribution. At each grid point, TDR computes the quantity of material outside a radius corresponding to the distance from the center of a puff to the grid point. This is then used to compute an estimate of the material deposited at the grid point by the initial source function. Anomalies may arise when the initial standard deviations of the puffs are significantly smaller than the grid spacing. With random locations of the sources, the initial TDR deposition estimates can, and do, vary significantly over the grid. Because of the relatively low height of the sources, the initial deposition directly under each source is very high and falls off rapidly as we move away from the source location. This results in very localized deposition which to some extent dominates the plots of deposition at later times. This is born out in Figure 6-1 where the total deposition at 54 seconds is less than 24 percent of the total at 200 seconds (see Table 6-2). Note from Table 6-1 that the maximum deposition at a point on the grid at 54 seconds is 88 percent the maximum at 200 seconds.

As mentioned previously, an additional source of fiber deposition that is not spatially or temporally tracked is a function of the efficiency factor effa in the TDR Phase I definition of the source (see Appendix B). This factor is a multiplier of the total source mass (or in this case the total source count) that adjusts the source for undeployed non-transported material. In this case, it was assumed that 25 percent of the fibers in each source do not disseminate in the air. The expectation would then be to find the "missing" fibers in the expended source, or spread on the ground nearby. This then would add an additional 3.037×10^{10} fibers over the initial deployment area. This superposition of fibers would result in about 56.3 percent of the 12.148×10^{10} fibers being deposited somewhere on the grid area, with 31.28 percent accounted for on the grid by TDR, and 25 percent unaccounted as to location.

Finally the average values over the area of 221,796 m^2 at various times are presented in Table 6-3. These are the average values computed by dividing the entries of Table 6-2 by the area. It is instructive to compare the maximum and the average values of exposure in Tables 6-1 and 6-3 to the local exposure values in Figure 5-4. Figure 5-4 yields mature (i.e., non-increasing) exposure values that are about 2.5 times the average values given in Table 6-3 at about 150 seconds. However, these same local or point exposure values from Figure 5-4 are only about half the maximum values shown in Table 6-1 for about 150 seconds. These two simple comparisons are logically bounded and help demonstrate the consistency of the TDR predictions.

---

[10] The puffs are modeled as instantaneously appearing Gaussian clouds at the source initiation time. The initial expansion of the puff, which may involve significant energy, is not directly modeled, except for the modeling of material deposited on the ground due to the radial expansion, and the elevation of the center by the buoyancy radius as previously noted.

7 LINE-OF-SIGHT TRANSMISSION CALCULATIONS WITH TDR

To gain an appreciation of the attenuating capability of the resultant mmw obscurant cloud, it is informative to calculate results relative to a top-down view through the volume of the cloud. This analysis involved use of the Phase II module of the TDR code. Section 6 was based on calculations within the Phase III module of TDR.

In the look-down analysis, the angular field-of-view was arbitrarily chosen to be 15 deg in the downwind direction and 15 deg in the crosswind direction. To achieve a physical field-of-view at ground level of 360 × 360 m, an observer height of 1367.2 m was computed. The field-of-view was divided into 60 sections in both the downwind and crosswind directions. This resulted in a physical resolution of 6 m (on average), which is the physical resolution of the computations from Section 6. The target or objective plane was then chosen to be 1.5 m above the ground to retain association with previous calculations. The observer height was then increased 1.5 m to 1368.7 m to compensate. The chosen angular field-of-view is small enough to keep the fish-eye effect quite small. The center point of the physical field-of-view was chosen to be 290 m downwind of the center of the source distribution circle and on the downwind centerline so as to capture the cloud at 110 seconds. The attenuation map presented in Figure 7-1 was constructed from 3600 separate line integrations. The axes in this figure are consistent with those shown in Figure 4-1. The computations for this attenuation map were based on the material response characteristics of single fibers at 24 GHz, as presented in Table 3-2.
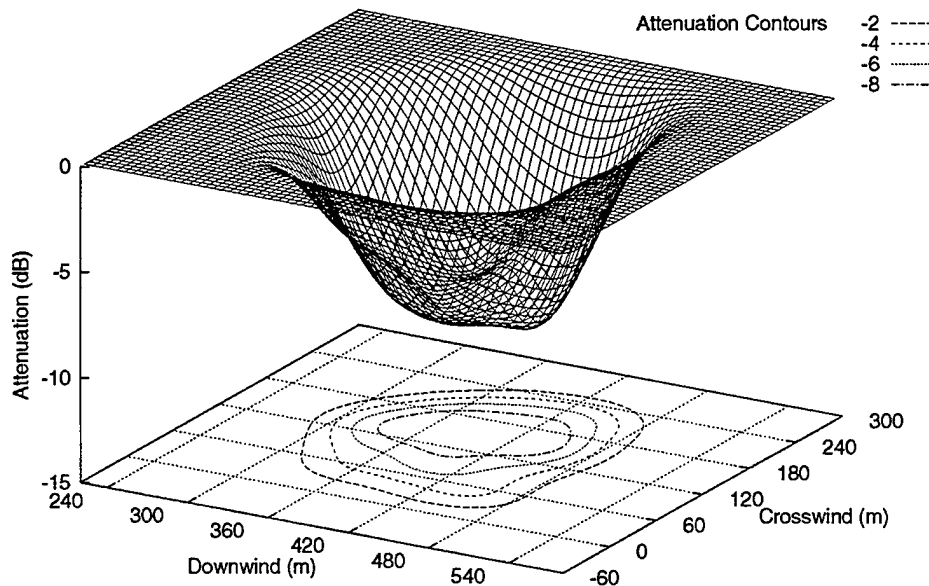
Figure 7-1. One-Way Lookdown Attenuation of Cloud at 110 seconds

Figure 7-1 shows contour lines of one-way attenuation from -2 through -8 dB. Recall from Figure 3-3 that mmw obscurants also possess some scattering cross section. Performance of radar or mmw obscurant clouds may depend on both backscatter and attenuation levels. Reference [13] was an examination of radar

obscurants and how they deny target designation in synthetic aperture radar (SAR) imaging. This study established objective relationships between SAR operator targeting performance and specific backscatter and attenuation levels resulting from radar obscurant clouds interacting with X-band ($\approx$9 GHz) electromagnetic radiation. Operator performance was found to degrade with increasing levels of both backscatter and attenuation. Mission failure, defined as the inability of the operator to designate a target, was quantitatively related to both backscatter and attenuation.

8 MATERIAL CONTAMINATION OF INTERIOR SPACES

8.1 APPROACH PHILOSOPHY

Having discussed aerosol cloud concentration histories relative to several specific points within Figure 2-1, it is logical to investigate concentration and exposure dynamics when such obscurant clouds are ingested by a ventilation system. One important reason for such an investigation is that airborne fiber material likely present the greatest risk to man through inhalation. Accurate prediction of aerosol concentration within the spaces of a structure is a complex problem. Depending on the specific objective of the predictions, the solution may require exceptionally detailed physical modeling. High fidelity modeling may require CFD solutions. Sometimes, however, less sophisticated approaches may provide the required insight. This latter approach has provided the foundation for this section of the report.

8.2 PHYSICAL SCENARIO

Assume that Figure 8-1 represents a cloud concentration history just outside a building inlet ventilation duct. The overall shape and duration of the event are not atypical of a large aerosol cloud. Two ordinate scales appear on Figure 8-1. The right-hand scale indicates a maximum concentration of 3×10^5 fibers/m^3. For physical scenarios modeled in Sections 4 and 5, the TDR prediction (see Figures 4-3, 4-4, 4-5, and 5-3) show that such a maximum concentration is readily attainable. The left-hand scale of Figure 8-1 indicates a maximum concentration of 1×10^9 fibers/m^3. This is an exceptionally high concentration and it is worth further discussion to put this number into perspective.
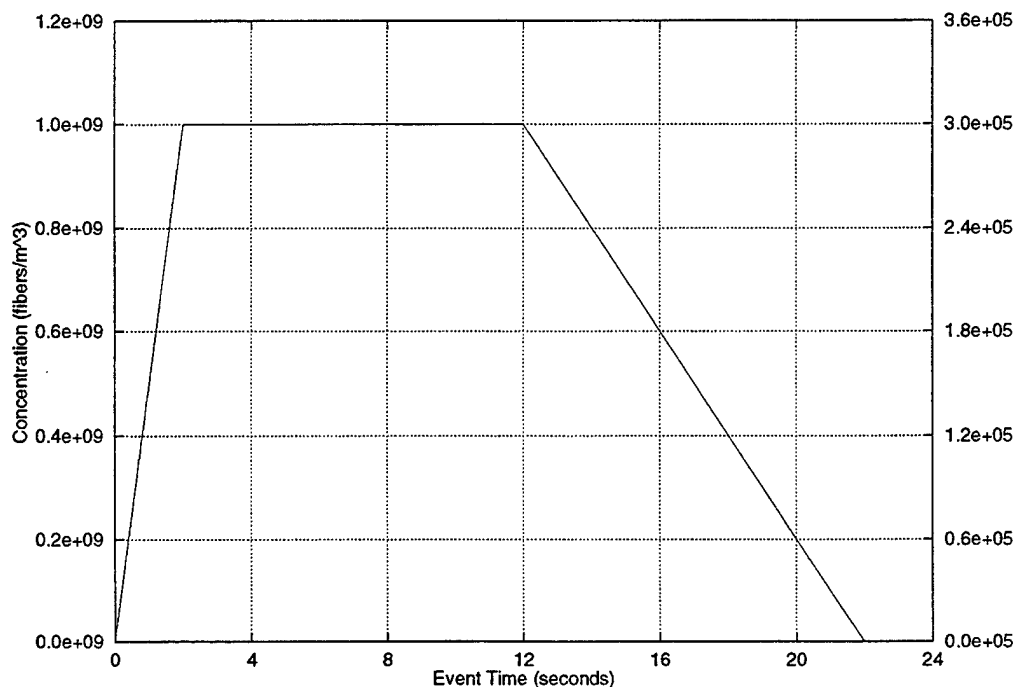
Figure 8-1. Inlet Duct Concentration Time History

The nominal fiber of interest is 6.35 mm in length, has a 7.5×10^{-6} m diameter, and has a density of 1.8 gm/cm^3. The concentration of fibers that are aerodynamically independent can be approximated by computing the number of 6.35 mm diameter spheres in a 1 m^3 volume. This simplified computation yields

7.46×10^6 fibers/m^3. If the calculation assumes that the 6.35 mm spheres must be contained within cubes that are stacked to make a 1-m cube, then the concentration of aerodynamically independent fibers becomes 3.91×10^6 fibers/m^3.

If each fiber is assumed to be packed in hexagonal fashion, then the maximum packing density for the 7.5×10^{-6} m diameter fibers can be calculated as 3.23×10^{12} fibers/m^3. This concentration yields a 1-m cube that weighs 90.7 percent that of a solid cubic meter of the obscurant material.

A concentration of 1×10^9 fibers/m^3 would yield a 1-m cube that weighed 0.028 percent of a solid 1-m cube of the obscurant material. Alternatively, the 1×10^9 fibers/m^3 can be converted to 0.505 kg/m^3.

The building chosen for analysis was an underground Command, Control, Communications, and Intelligence (C^{3}I) facility, also known as a type B hardened structure (see Reference [14]). Table 8-1 identifies the rooms in the bunker and provides an estimate for the volume of each room. Per these room estimates, the total volume of the building connected to the primary air distribution system is 184,864 ft^3.

Table 8-1. Bunker Compartment Identification, Volumes, and Usage

Space No.	Volume (ft^3)	Description
105	5964	Tech Control
106	5964	Radio Switch Room
107	5964	Comm Center
108	8064	ADP
109	6804	Plans/Logistics
110	5796	Restrooms
111	6804	Break/Dining Room
112	5964	Storage Room
113	5964	Admin and Facility Mgr.
114	5964	Security
115	5880	Intel
116	5880	Ops
117	5880	Common/Briefing Room
118	5964	Cooling Towers
119	5964	Diesel Generator Room
120	5964	Diesel Fuel Tanks
121	8064	Electrical Distribution and Control
122	6804	UPS and Batteries
123	5796	Restrooms, Potable and Waste Water Storage
124	6804	Workshop and Parts Storage
125	8064	Mechanical Chiller Plant
126	5964	Oxygen Storage and CO$_2$ Removal
127	5964	Air Handling
128	5964	Ventilation and Filtering
129	29568	Down Corridor
130	18880	Up Corridor
131	8064	Billeting

In any dissemination of mmw obscurants, some fraction of the fibers are broken or fractured during the very early formation of the cloud. Typical unbroken mmw obscurants have equivalent aerodynamic diameters in the range of 10 to 50 μm. As indicated in Reference [15], fibers of this size are not respirable (i.e., not penetrable past the terminal bronchioles) in humans. In fact, penetration to the collector begins only when the aerodynamic diameter is reduced to about 8 μm. For the results presented in Sections 4, 5, and 6 of this report, the virgin particulates had an aerodynamic diameter of just under 14 μm (as based on a settling speed of 1 cm/s). Reference [15] shows that the thoracic mass fraction penetration (i.e., penetration past the

larynx) for a 14 μm aerodynamic diameter particle is about 20 percent. Since some of the mmw obscurants will break during the dissemination, this action will effectively reduce the aerodynamic diameter of some particulates to a value less than 14 μm. If these fractured particulates are ingested into the air handling system of a building and not filtered out, humans inside might be adversely affected or at least irritated by the contamination.
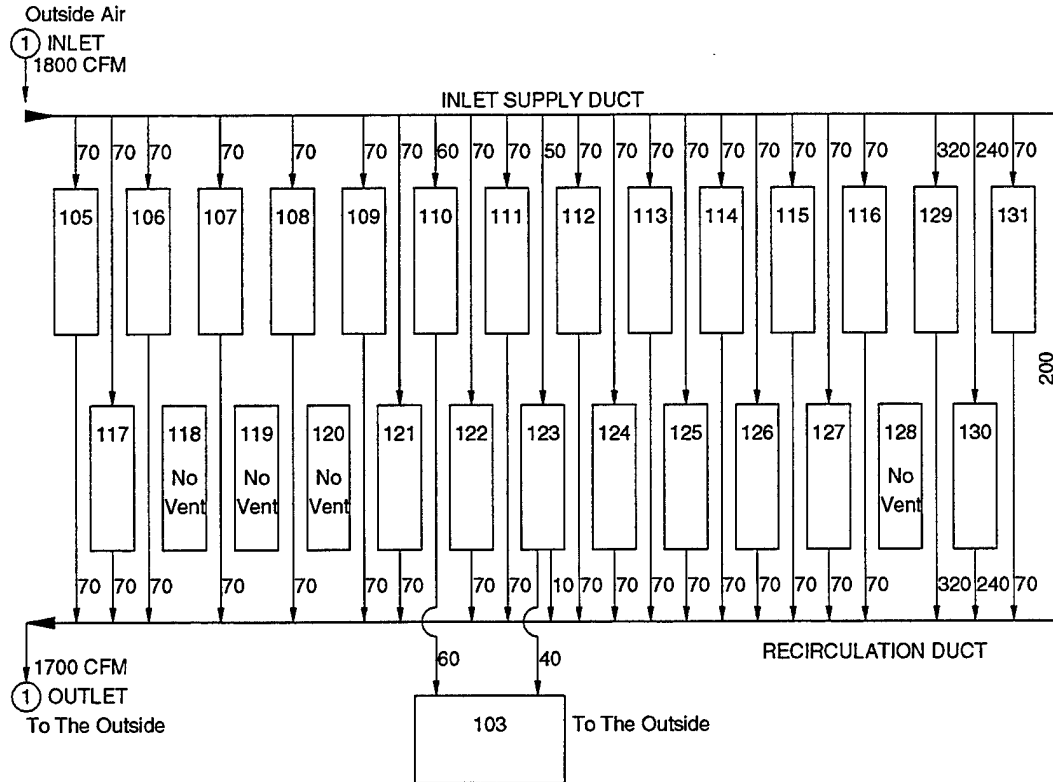
Figure 8-2.   Building Ventilation Schematic

One of the main reasons the C^{3}I building was chosen is the diverse range of ventilation conditions that can reasonably be associated with its operation. Two widely disparate ventilation conditions were assumed for the building. The first case was a low inlet flow based on a "sealed" building status (see pages 75–77 of Reference [14]). For this case the total ventilation was 2000 cfm with this flow comprised of 1800 cfm inlet air flow and 200 cfm recirculation flow. Figure 8-2 shows the assumed primary ventilation system for the low flow case. All the indicated air flows in this schematic are in cubic feet per minute. The "No Vent" spaces in Figure 8-2 were assumed to have special dedicated ventilation requirements and were not considered as being connected to the primary ventilation system. The second ventilation condition was the high flow case, which was intended to be more typical of "normal" building operation. This case was constructed by assuming that the total volume of the building connected to the primary air distribution system was refreshed with outside air about four times per hour. By using this typical rule-of-thumb guideline, all the flows in Figure 8-2 can be multiplied by the factor 6.85. The inlet flow then becomes 12,330 cfm rather than 1800 cfm.

The analysis focused on two inlet concentration histories (Figure 8-1) and two ventilation cases—low flow and high flow. It is informative to analyze the total weight of all single fibers that would be ingested into the inlet ducts of the C^{3}I building for these situations. For the low flow case, the typical and very high concentration aerosol events would yield, respectively, 2.059×10^3 gm (4.54 lb) and 6.864×10^3 gm (15.14 lb). For the high flow case, the typical and very high concentration aerosol events would yield, respectively, 14.105×10^3 gm (31.10 lb) and 47.018×10^3 gm (103.68 lb). To put these weights in perspective, recall that the total weight of all fibers in the 216 sources analyzed in Section 4 was assumed to be 61.344×10^3 gm (135.26 lb). For convenience Table 8-2 summarizes the above quantitative information.

Table 8-2. Concentration, Flow, and Weight Facts

Concentration Facts for Nominal Fiber:

Concentration Type	fibers/m^3
maximum typical (see Figure 8-1)	3.00×10^5
maximum very high (see Figure 8-1)	1.00×10^9
aerodynamically independent (simplified)	7.46×10^6
aerodynamically independent (cubic stacked)	3.91×10^6
maximum packing density (hexagonal packing)	3.23×10^{12}

Flow Facts:

Flow Type	ft^3/min
inlet flow (sealed operation — low)	1,800
inlet flow (normal operation — high)	12,330

Weight Facts for Low Flow:

Inlet Conditions	Total Ingested into Building gm	lb
typical concentration	2.059×10^3	4.54
very high concentration	6.864×10^3	15.14

Weight Facts for High Flow:

Inlet Conditions		
typical concentration	14.105×10^3	31.10
very high concentration	47.018×10^3	103.68

Weight Facts for Sources:

total source weight	61.344×10^3	135.26

8.3 MODELING AEROSOL CONTAMINATION

Having discussed the ventilation dynamics of a given building and postulated potential concentration histories at the inlet duct of a building, it is now appropriate to model the contamination within the building caused by the solid particulate aerosol. In keeping with the philosophy of Section 8.1, the model chosen for application was the *Ship Chemical Warfare* (CW) *Vulnerability Ventilation Model* (VENM). VENM was originally developed to predict CW agent dosage histories within a ship under an attack involving external CW bursts or penetrating CW warheads (see Reference [16]). VENM is a simple yet useful model that has benefit beyond ship analysis. It was suggested for application to the building geometry by the Chemical and Biological Systems Analysis Branch (B51) at NSWCDD. Personnel from B51 ran the VENM simulations and provided the output data files for further graphic manipulation and interpretation.[11] The choice of VENM was based on its ease of use, ready availability, experienced local user base, and level of physical fidelity sufficient for our needs.

The National Institute of Standards and Technology (NIST) has developed a computer program called CONTAM93 (now updated to CONTAM96) to calculate airflows and dynamic levels of indoor contaminants within multi-zone buildings (see Reference [17]).[12] Both the contaminant and airflow simulations are based on high fidelity physical modeling but still constrained within a non-computational fluid dynamics environment. Although not used in the present analysis, a review of Reference [17] suggests that CONTAM96 is a strong candidate for providing good solutions to complex, pressure driven, airborne contamination problems relevant to building systems.

Two very stringent assumptions governed the VENM simulations. First, both the inlet supply duct and the recirculation duct were modeled as having zero volume. This has the effect of producing instantaneous propagation of inlet and recirculation duct concentrations. That is, the concentrations indicated in Figure 8-1 are immediately applied to the inlet flow of each room having ventilation as indicated in Fig-

---

[11] Richard Amick and Mary Beth Morris of B51 provided this support.

[12] The technical point of contact at NIST is George Walton, Building and Fire Research Laboratory, (301) 975-6421.

ure 8-2. Recirculation also reacts instantaneously to modify the input concentrations. The second limiting assumption involves the method by which the individual room aerosol concentration is calculated. The net number of fibers resident in a room at a given time is assumed to be instantaneously mixed and uniformly distributed throughout the room volume. Localized or spatially dependent flow effects within a room are neglected as is aerosol deposition within a room or duct.

Although the VENM model does accept user-defined inputs for both filter efficiency (percent) and filter capacity (milligrams) for each flow path between a donor and a recipient space, it was decided to run VENM with a values of zero for these inputs. The rationale for this decision was the attempt to keep the present analysis conservative (i.e., constraining the analysis to yield reasonable upper limits for room concentration and exposure).

In the VENM model, the time-dependent inlet duct concentration is entered in units of milligrams per cubic meter. The model then computes the dynamic room concentrations in milligrams per cubic meter. In the VENM results that follow, the weight per unit volume concentrations were transformed to units of fibers/m^3 by assuming that all the ingested aerosol material was comprised of single, non-fractured fibers. This assumption is consistent with both the nominal or baseline TDR prediction and the experimental interferometer results wherein one fiber per bundle was assumed. When observing the VENM predictions remember that the graphs of room concentration and exposure values would be higher if fractured fibers were considered and lower if bundles of whole fibers were considered.

8.4 VENM PREDICTIONS AND COMPARISONS

Results from the VENM simulations are shown in Figures 8-3 to 8-12. The simulations extended to almost one hour. Only results for selected rooms are shown. These representative rooms have space numbers 106, 121, and 122 (see Table 8-1). A result for one room can be extended to another room if they both have the same volume and the same inlet and outlet flows. For example, the break/dining room (space 111) will have the same result as space 122. Similarly, the billeting office (space 131) will respond exactly as space 122.

Each of the Figures 8-3 to 8-12 has two ordinate scales. The left vertical scale correlates with very high aerosol inlet concentration while the right vertical scale should be used to determine results for the more typical aerosol inlet flow. Figures 8-3, 8-5, 8-7, 8-9, and 8-11 are results for the 1800 cfm inlet flow. Figures 8-4, 8-6, 8-8, 8-10, and 8-12 are results for the 12,330 cfm inlet flow. Room concentration predictions are contained in Figures 8-3 to 8-8 while room exposure predictions are shown in Figures 8-9 to 8-12.

Several interesting comparisons between the results in the figures deserve discussion. Even though the early room concentrations are much higher in Figure 8-4 than in Figure 8-3, this trend is relatively short duration and the relationship reverses. This is the direct result of the high ventilation flow rates in Figure 8-4. The impact of the high ventilation flow is even more pronounced when the exposure results in Figures 8-9 and 8-10 are compared. From Table 8-2 recall that for either of the two inlet concentration conditions, the high ventilation flow rate will cause 6.85 times as much aerosol to be ingested into the building. However, as indicated by the final exposure values at 3500 seconds in Figures 8-11 and 8-12, the high ventilation flow rate caused an exposure that was only about twice as great as the low ventilation situation.

As mentioned in Section 8.3, filters were purposely not placed between donor and recipient spaces in the VENM simulations. If filtration of the air had been considered in the analysis, then all the ordinate values in Figures 8-3 to 8-12 would have been much lower. Such lower values would have been a strong function of the specific type of filter employed. Filter types have various efficiency factors depending on the physical characteristics of the aerosol particulates and the flow dynamics at the filter. The filter efficiency factor is defined as one minus the transmission factor (the ratio of transmitted particulates to incident particulates). Conventional disposable panel filters made of continuous filament glass fibers and having thickness between 1 and 2 inches can have transmission factors in the range of 0.1 to 5.0 percent for fibers like the nominal fiber considered in this report. Alternatively, the filter efficiency could range from 99.9 to 95.0 percent. Focusing only on the exposure predictions shown in Figures 8-11 and 8-12, very efficient filters could reduce the indicated ordinate values by as much as a factor of 1000. That is, each ordinate value in these two figures could be multiplied by 1×10^{-3}.
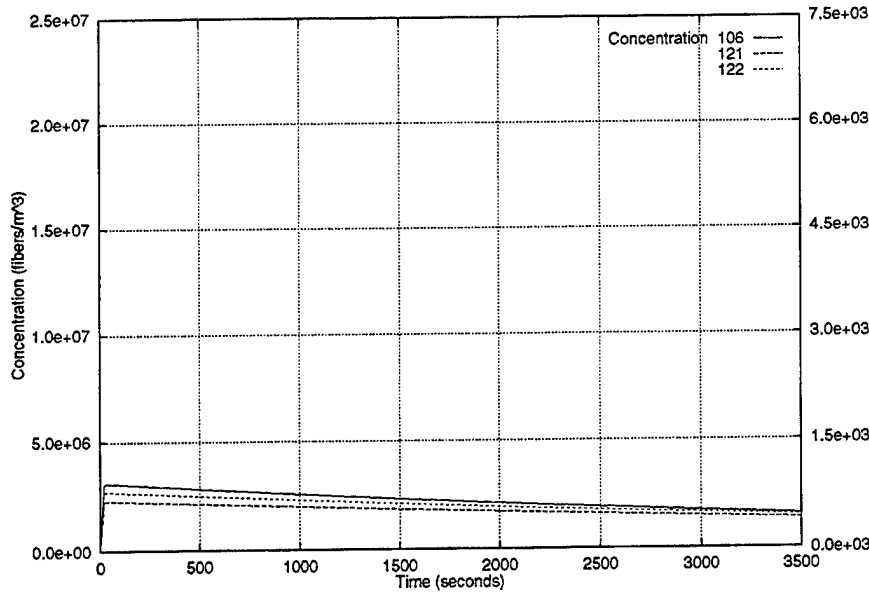
Figure 8-3. **Concentration - 1800 cfm airflow**
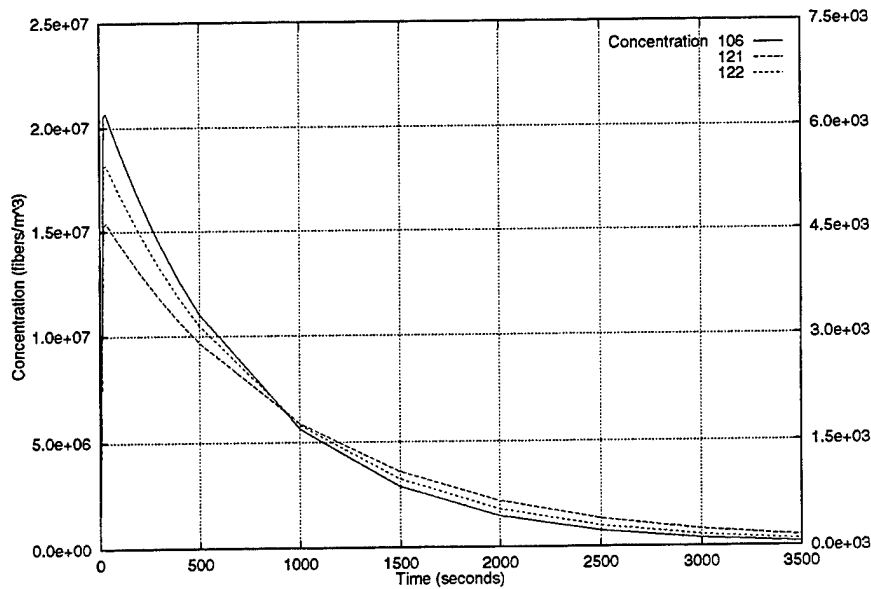
Figure 8-4. **Concentration - 12330 cfm airflow**

Although the results in Figures 8-11 and 8-12 are "conservative" as defined in Section 8.3, the importance of air filtration should not be overlooked. This is particularly true if some special exposure threshold value is being predicted for a given room. To summarize, Figures 8-3 to 8-12 bound the upper limits of concentration and exposure, as constrained by the two limiting assumptions discussed in Section 8.3.

8.5 IMPLICATIONS OF CFD MODELING FOR ROOM CONCENTRATION PREDICTIONS

If the assumptions implicit in VENM for instantaneously mixed and uniformly distributed particulates within a room volume is deemed unsatisfactory because of concern for spatially variable concentration, then higher fidelity modeling must be employed. This high fidelity approach will be CFD. One commercial CFD code with a large world-wide user community is CFX from AEA Technology Engineering Software,
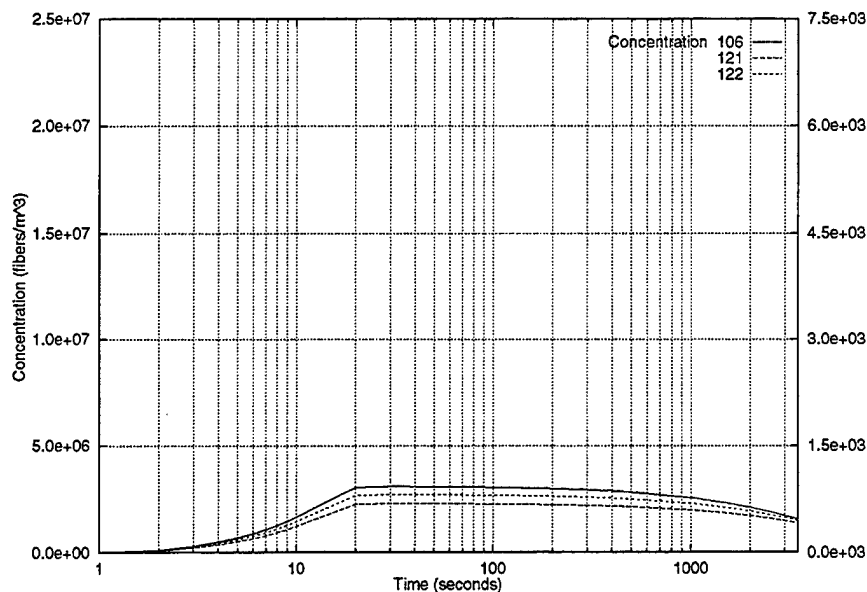
Figure 8-5.   Concentration - Log Time - 1800 cfm airflow
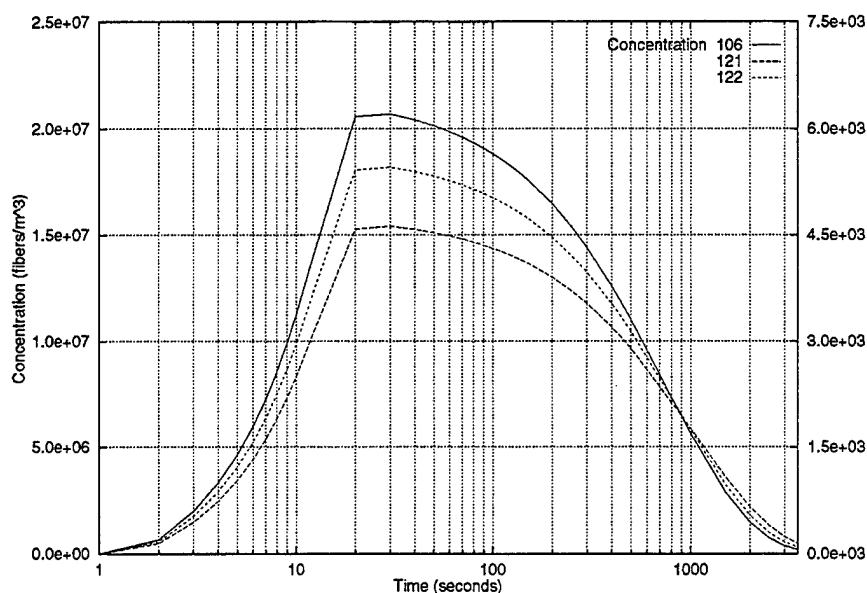
Figure 8-6.   Concentration - Log Time - 12330 cfm airflow

Incorporated. This code is being used at NSWCDD and is resident within the B51 Branch.[13] B51 constructed an example to provide insight to the flow dynamics within a ventilated room.

The notional example consisted of a room $8.0 \times 6.0 \times 2.5$ m with four air inlets and two air outlets. The room volume is 4238 ft^3, which is somewhat smaller than the rooms given in Table 8-1. As shown in Figure 8-13, the four inlets were located near the room center while the two outlets were located at opposite corners of the ceiling at one end of the room. Each of the four inlets has a face speed of 1.5 m/s. The inlet and outlet ducts were square and had dimensions 0.5×0.5 m. The total inlet ventilations flow to the room was 52.96 ft^3/s or 3177.6 cfm for the 1.5-m/s inlet duct speed. CFX version 4.1 was used to generate all CFD results. The prediction in Figures 8-13 and 8-14 depict solutions for steady-state, turbulent, isothermal flow. Note the spatially irregular particle trace shown in Figure 8-14. Even though all four inlets and both

---

[13] The resident expert user of the code is Mary Beth Morris.
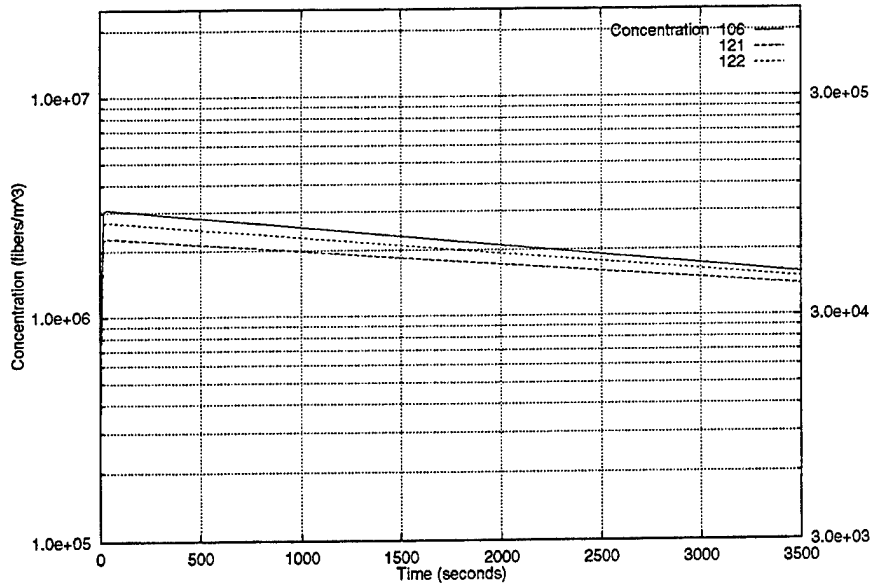
Figure 8-7. Log Concentration - 1800 cfm airflow
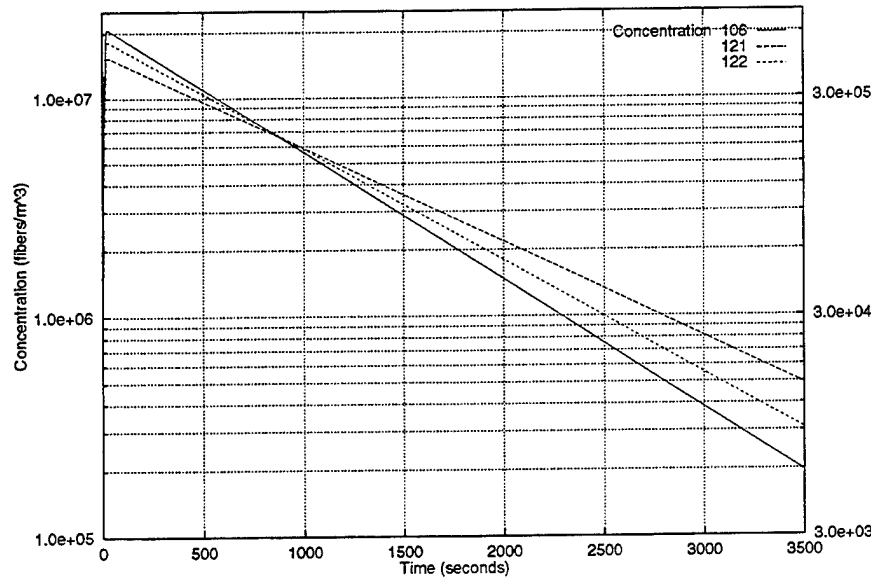
Figure 8-8. Log Concentration - 12330 cfm airflow

outlets were functioning in the situation depicted in Figure 8-14, only a trace from one inlet to one outlet was graphed.

Consider the generation of particle traces within the notional room when the particulates have mass and are somewhat similar to the previously defined nominal mmw obscurant. The following input parameters were used in the CFX simulation : a particle was assumed to have a density of 1.8 gm/cm^3, to be spherical and have a diameter of 23 μm, to have a settling velocity of 2.85 cm/s, a coefficient of restitution of 0.75, and an inertial release velocity of 0.5 m/s. The particle was assumed spherical because the present CFX software can model only this shape of particle. The sphere diameter was intended to be an aerodynamic diameter. An equivalent aerodynamic diameter is defined as the diameter of a sphere of unit density that has the same settling rate as the particle of concern. Once the settling velocity is calculated or assumed,
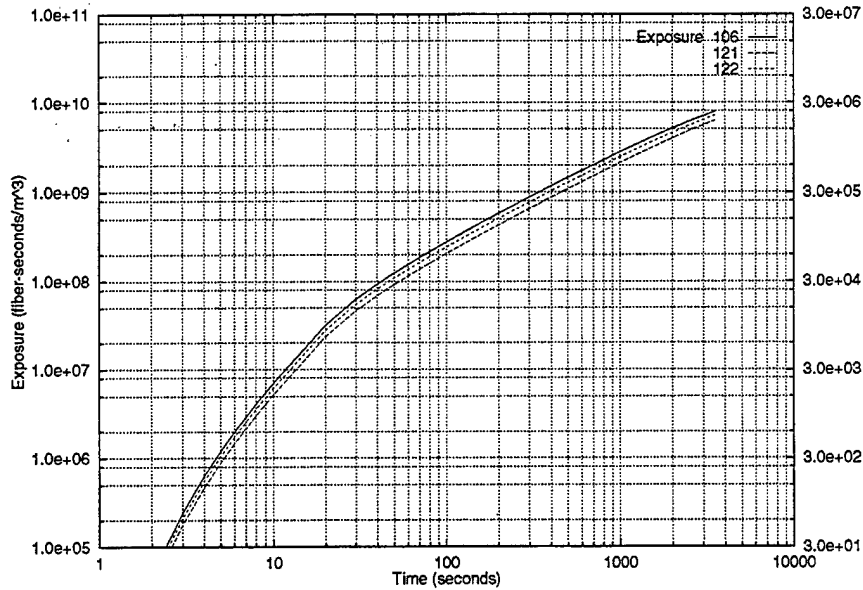
Figure 8-9.   Log Exposure - Log Time - 1800 cfm airflow
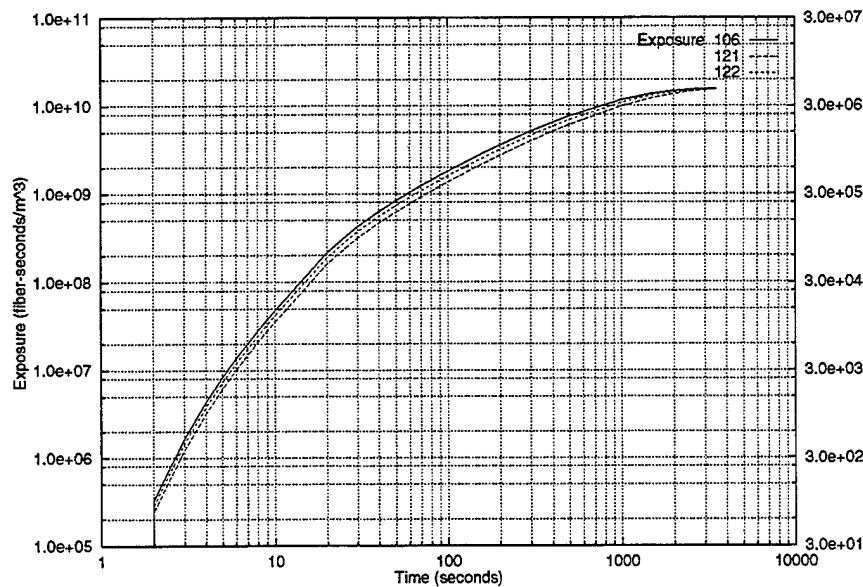
Figure 8-10.   Log Exposure - Log Time - 12330 cfm airflow

the equivalent aerodynamic diameter can be computed via Stoke's Law[14]. A coefficient of restitution of 0.75 means that 25 percent of the particles that come in contact with a wall boundary will stick and 75 percent will bounce off.

For the particle traces shown in Figures 8-15 to 8-18, a previously calculated flow field solution was used to "start" the problem. This particular flow field solution was based on a duct inlet face velocity of 5 m/s as

---

[14] For particles in air at sea level and standard temperature the settling rate for very low Reynolds number flow is given by the formula (see Reference [18]):

$$s = (1.21 \times 10^{-4})\rho r^2$$

where,
s = settling rate, (m/s)
ρ = specific gravity of an aerosol particle
r = radius of an aerosol particle (μm)
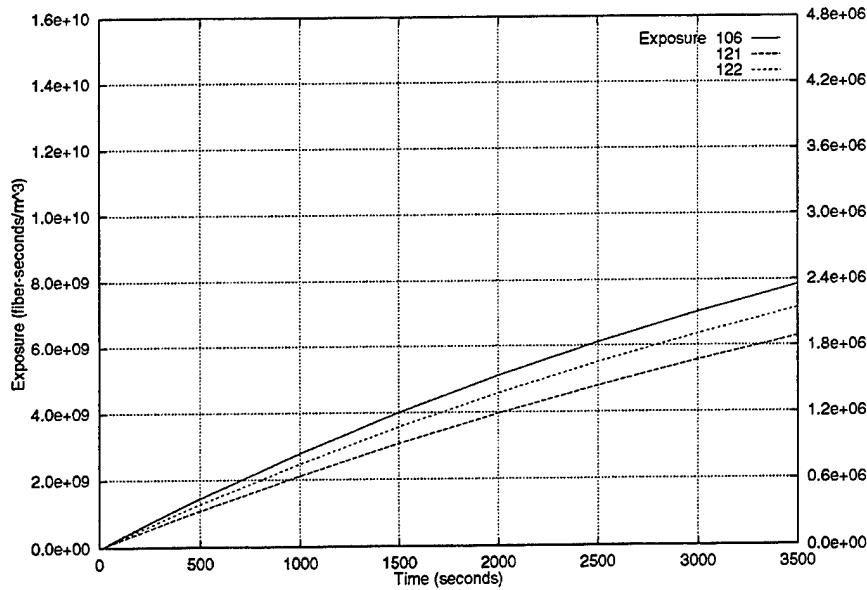
Figure 8-11. Exposure - 1800 cfm airflow
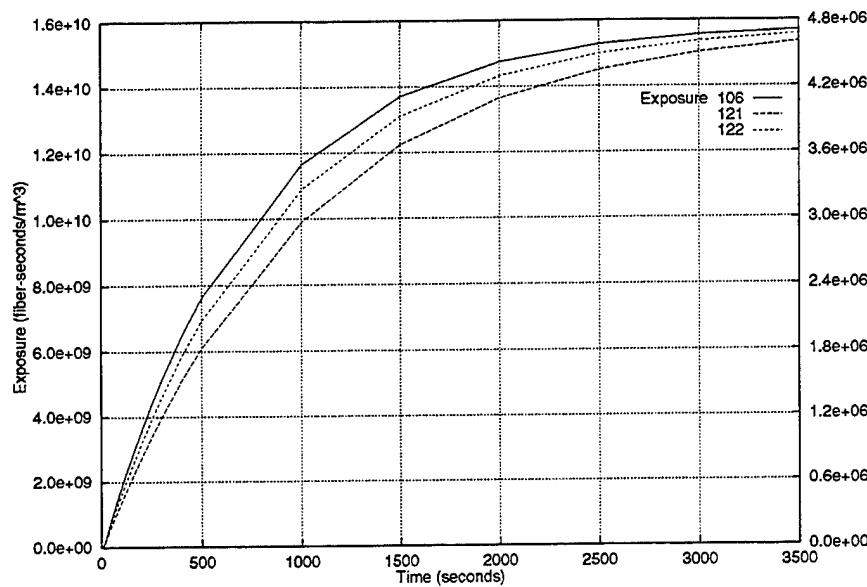
Figure 8-12. Exposure - 12330 cfm airflow

opposed to the 1.5 m/s situation depicted in the results of Figures 8-13 and 8-14. Such a dramatic increase in ventilation causes the total inlet flow rate to the room to be 10,592 ft^3/min. This causes the total room volume to be exchanged 2.5 times per minute. This situation creates an extremely well mixed state within the room volume.

The particles were released into this resident solution and were acted upon by the flow. In Figures 8-15 and 8-16, three particles were released from one duct and their motion was traced. Figure 8-15 shows, via color scaling, how long the particle took to move from the inlet to the outlet duct. Typically, the particle transit time was about 140 seconds. Figure 8-16 shows, via color code, the speed of three particles as they transit the room. One of the particles sticks to the wall of the right-hand outlet duct. This is in contrast to the increased speed (about 14 m/s) experienced by the one particle that enters the left-hand outlet and flows close to the duct centerline where the speed is greatest.

speed (m/s)

▦	4.7468
▨	3.9556
▩	3.1645
▤	2.3734
■	1.5823
	0.7911
	0.0000
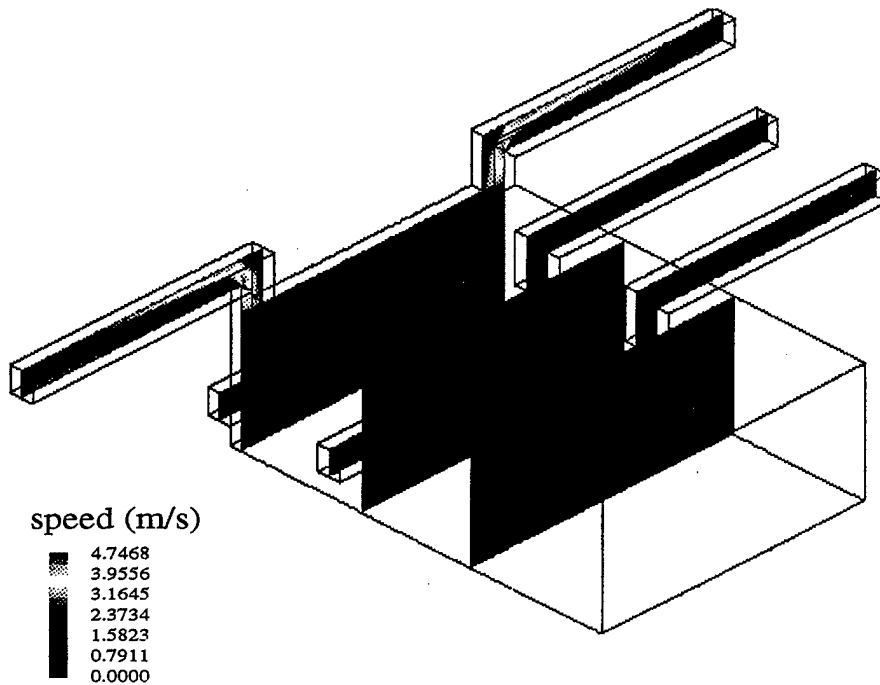
Figure 8-13.   Air Flow In A Room With Ducts — Inlet Velocity 1.5 m/s

speed (m/s)

■	5.134
	3.850
	2.567
	1.283
■	0.000
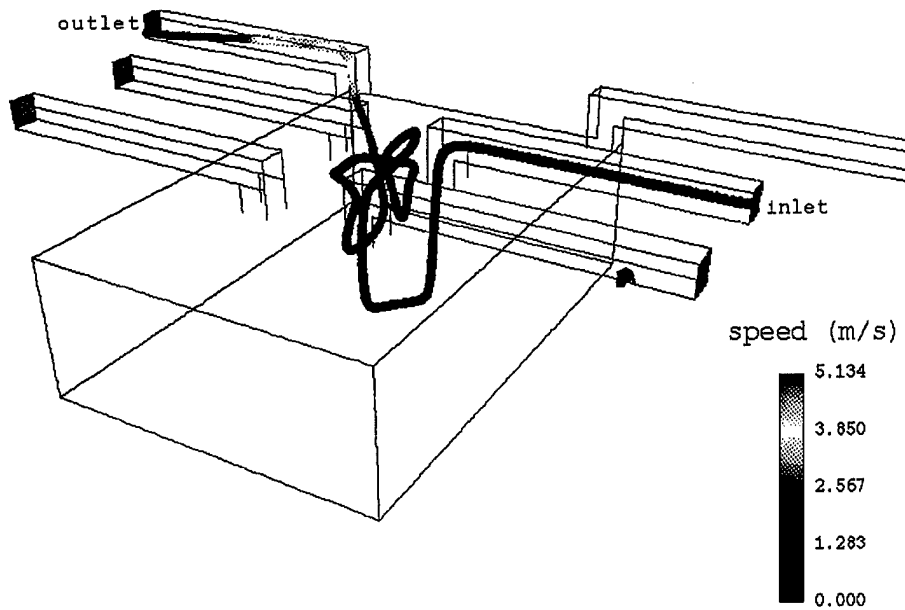
Figure 8-14.   Single Particle Trace Speeds — Inlet Velocity 1.5 m/s

Figures 8-17 and 8-18 are analogous to Figures 8-15 and 8-16; however, in these new figures a total of 81 particles were released into the previously calculated flow field. The 81 particles represent particle releases from each of the 81 resolution cells in the duct openings. In Figure 8-17, the aggregate transit time appears to be between 90 and 120 seconds for the released particles. In Figure 8-18, the speed of the exiting particles converges to 10 m/s, the value expected from simple continuity considerations.
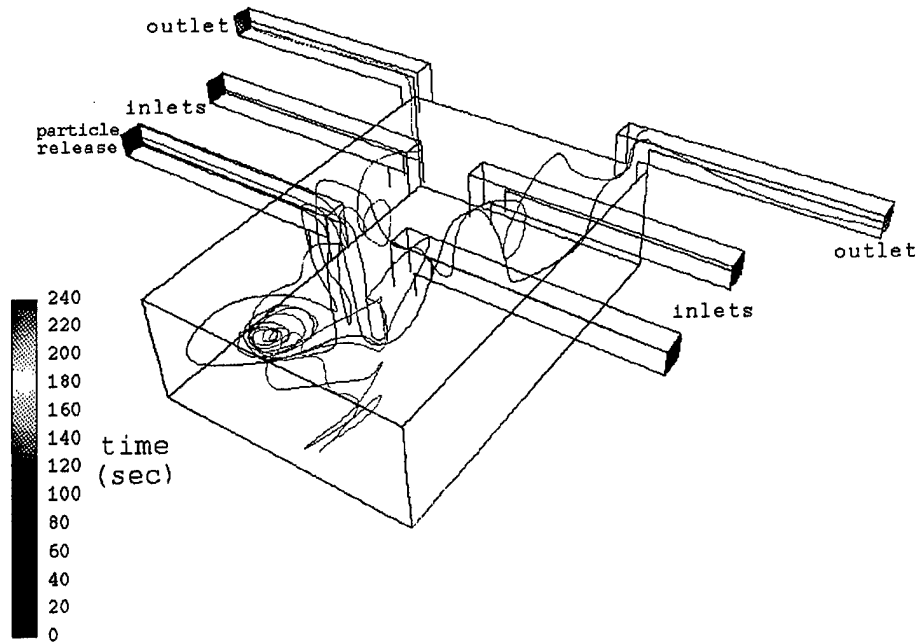
Figure 8-15.   Three Particle Traces Time — Inlet Velocity 5 m/s
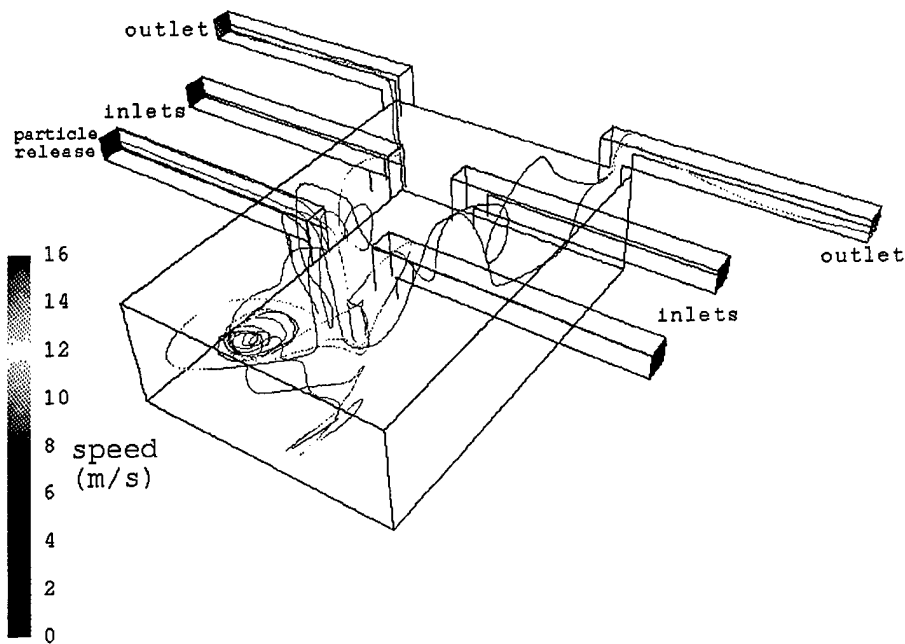
Figure 8-16.   Three Particle Traces Speed — Inlet Velocity 5 m/s

Recall when observing Figures 8-17 and 8-18 that the room flow field was applicable to all four inlet ducts and both outlet ducts in operation. The particles were, however, traced only from their release in one inlet duct. Notice the pronounced self-segregation of the released particles to the left side of the room. Clearly, if particles entered the room from only the left foreground duct, the room concentration and exposure would be dramatically non-uniform. In fact, some locations on the right side of the room might not experience any particulate exposure. Figures 8-17 and 8-18 illustrate one of the potential shortfalls of using a simplified ventilation model like VENM if localized room concentration is a desired result. If the
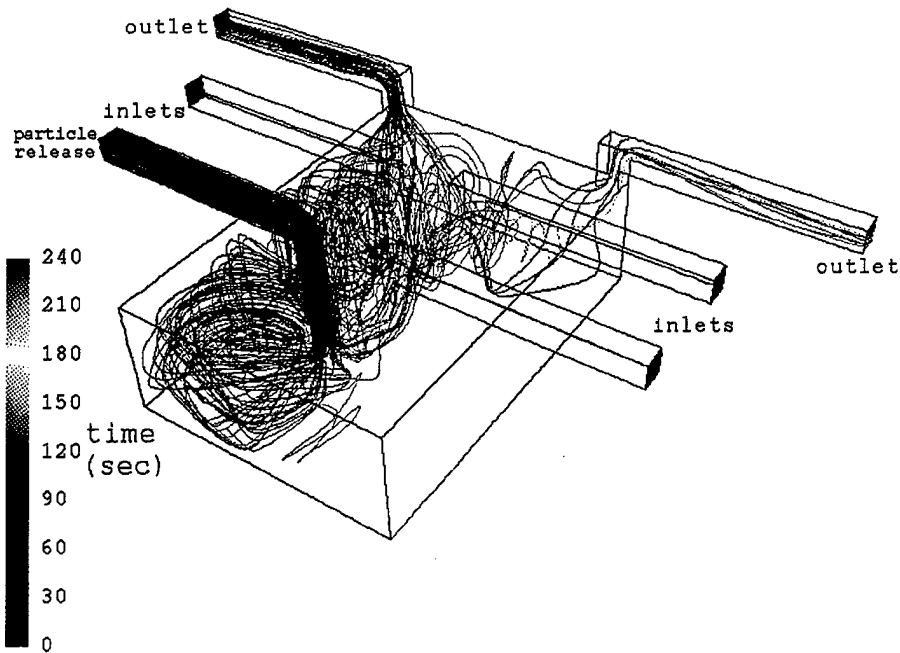
Figure 8-17.   Many Particle Traces Time — Inlet Velocity 5 m/s
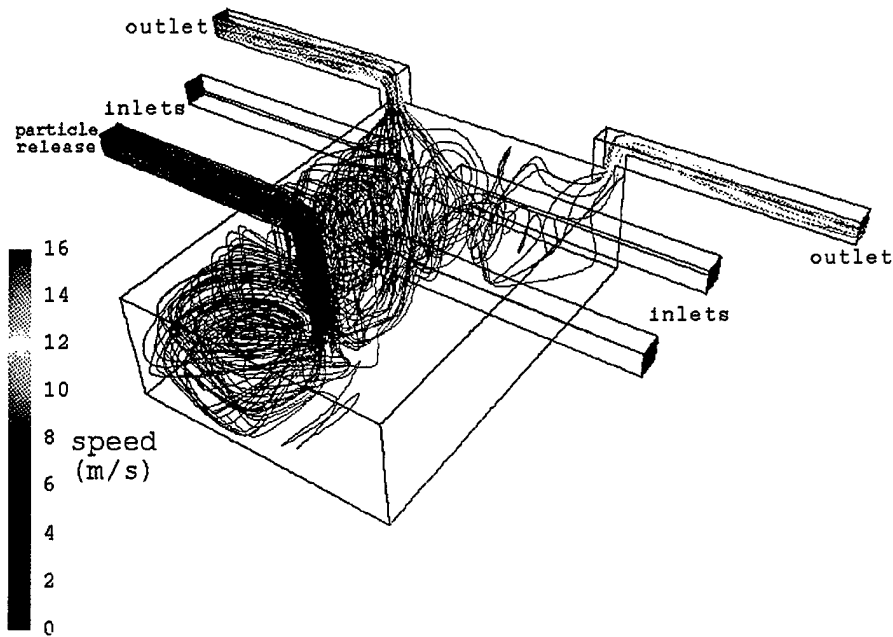
Figure 8-18.   Many Particle Traces Speed — Inlet Velocity 5 m/s

spatial variation of particle concentration and exposure within a confined or bounded space is truly required, then CFD solutions are the only viable approach. Such CFD solutions do have a significant penalty in that they require sophisticated software models, a smart or expert user, and a very capable hardware platform to minimize run times, which still may be long. Before CFD modeling is employed for a specific problem, both the potential benefits and the increased costs should be carefully weighed.

8.6 IMPLICATIONS OF CFD MODELING FOR PREDICTION OF EXTERNAL FLOWS

Recall that Section 8.2 began with the assumption of Figure 8-1 representing two possible cloud concentration histories just outside a building ventilation inlet. The fundamental question about choosing any concentration history prediction is its believability or reasonableness with respect to actual circumstances. Even with the HRW model providing terrain dependent wind fields for use by the SABRE model, the resultant cloud history produced by TDR is Gaussian in nature. TDR does not solve for bounded interior or recirculating flows; only CFD models can produce such results (see Figures 8-15 to 8-18 for examples). One important issue to address in choosing whether to employ a Gaussian or a CFD solution for concentration prediction is the potential impact that recirculation zones may have on particle concentration.

Recirculating zones of turbulent eddies readily arise in external flows. The CFX code was used by B51 to model wind flow over five notional buildings. The buildings were simple rectangular parallelepipeds 30 m on a side but of varying height. The buildings had heights of 10, 20, 25, 40, and 50 m. The buildings were placed in two rows, three buildings in one row and two buildings in the other row. The rows were separated by 30 m. Within each row the buildings were 60 m apart. As shown in Figure 8-19, the wind speed was 5 m/s and the wind approached the buildings from a 45-deg angle. Figure 8-19 clearly shows that the buildings interacted with the wind and produced changes in wind speed and direction.
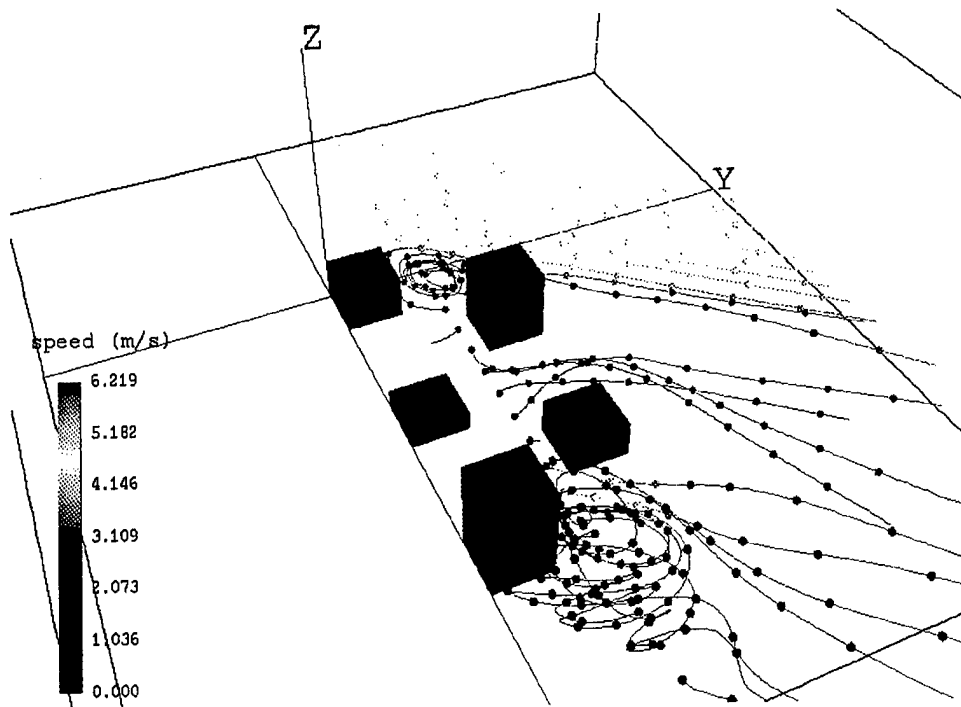
Figure 8-19.   Air Flow Past Five Buildings

In particular, the massless particle traces in Figure 8-19 show two pronounced recirculation zones just behind the first and third buildings in the row of three. Although the CFD solution was for the entire region around the five buildings, the particle trace graphic rendering was chosen to begin midway between the two building rows. This was done to reduce visual clutter in Figure 8-19. By observation of the color scale in Figure 8-19, note the lower speeds in the recirculation zones (about 2 m/s). These downstream eddies might produce a localized increase in particle concentration and exposure. The real issue is whether such localized increases (or decreases) are really significant to the problem being analyzed.

Shown in Figures 8-20 and 8-21 are graphical renderings of steady-state isothermal turbulent wind flow over a notional FFG class ship. These massless particle traces were calculated using the CFX code. The computational space included 120,000 grid intersections. The notional FFG is 125 m in length and has
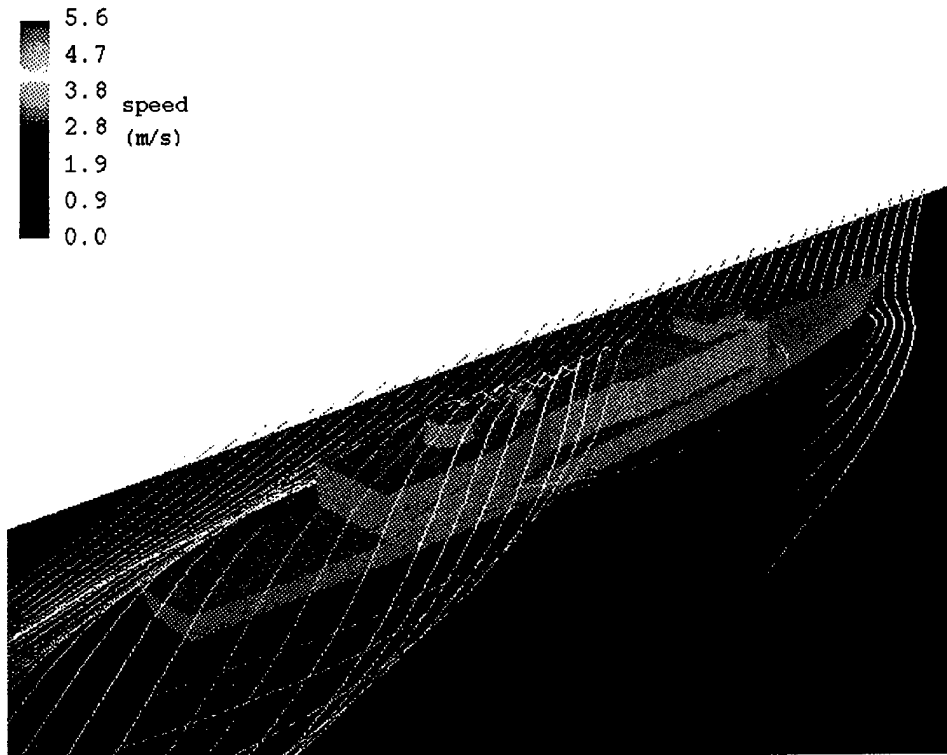
Figure 8-20. Air Flow Over Notional FFG
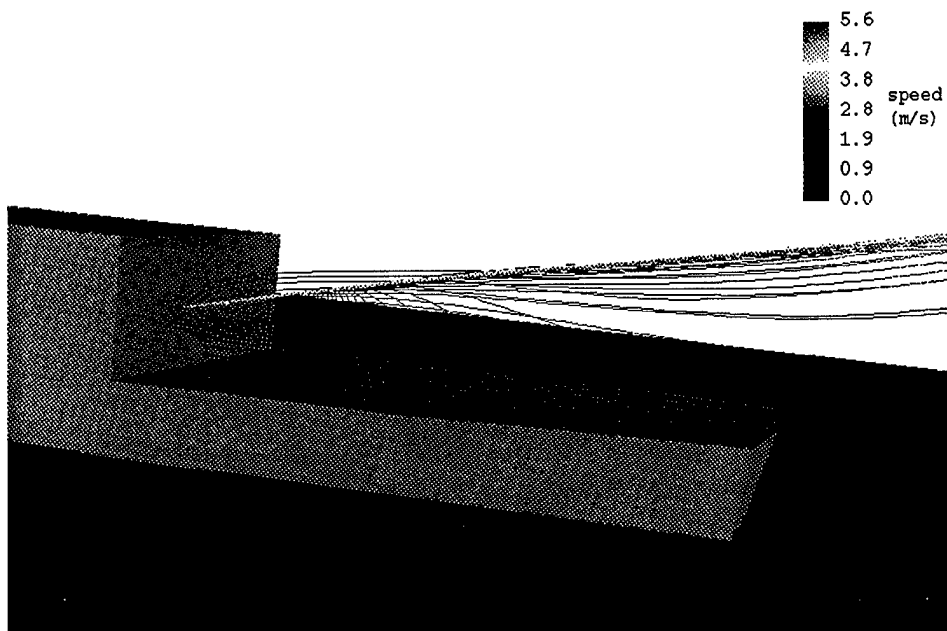
Figure 8-21. Aft Port View of Flow Over Notional FFG

maximum width and height of 16 m and 14 m, respectively. The vertical wind profile was based on a power law relevant to a neutral Pasquill atmospheric stability. The relative wind speed was 4 m/s at a height of 2 m and 5.6 m/s at a height of 40 m. In Figures 8-20 and 8-21 the wind approaches the ship at 30 deg offset from the longitudinal axis. Figure 8-20 gives an overall perspective of the flow over the ship. Figure 8-21 depicts the recirculating zone caused by the reward facing step on the ship superstructure (aft facing hanger

doors). The view direction in Figure 8-21 is from the aft port quarter. Just as for the flow over buildings, the question as to the impact that recirculating zones have on concentration is still the issue. Are they or are they not significant for the problem being addressed?

Consider a field dissemination of particulates like the nominal fiber of this report. If available yet technically disparate instrumentation (e.g., a microwave interferometer and a short path optical transmissometer, as discussed in Reference [19]) were used to measure the same local point, it is likely that the experimental results would differ by a factor of 2 to 5. This is to be expected because of the different assumptions or mathematical interpretations that are needed to convert the output of a given type of measurement device to a particulate concentration, and because of the disparate physical environments used to calibrate the various devices. Since no one type of local concentration measurement tool for mmw obscurants has proven itself the *best*, good experimental practice suggests that a variety of instrumentation be used in an experiment, provided the cost is not prohibitive. A careful interpretation of results from a diverse instrumentation suite should lead to a better determination of the *true* local concentration.

Since large experimental uncertainty for fiber concentration measurement is a fact of life, the need to employ higher fidelity simulation methods such as Navier-Stokes CFD solutions becomes an issue. The question then becomes whether the use of significantly more computational resources will provide results that are any more predictive for any particular event, and whether experimental evidence can corroborate the prediction.

For external flows, the authors assert that CFD should be employed if the flow dynamics would likely cause departure from Gaussian concentration predictions that are a factor of 10 different from the simple solution. Where the flow dynamics and geometry are deemed not so restrictive, then a Gaussian model like TDR does not in general have significant special deficiencies preventing useful prediction of randomly distributed events in a turbulent atmosphere.

9 REFERENCES

[1] Max Born and Emil Wolf. *Principles of Optics*. Pergamon Press, Oxford, fourth edition, 1970. Page 62.

[2] Mark F. Katrancha, Robert E. Richardson, William F. Cary, and David. H. Anderson. Calculations and Measurements of mm-Wave Obscurant Absorption and Scattering Properties. In *Proceedings of the Smoke/Obscurants Symposium XIX*, June 1996. Sponsored by the Chemical and Biological Defense Agency, Aberdeen Proving Ground, Maryland.

[3] Norman E. Pedersen and Jeanne C. Pedersen. Radar Target Concealment Program (U). Final Report AVMSD-0074-67-RR, AVCO Missiles, Space, and Electronics Group Missile Systems Division, April 1967. Contract AF04(694)-936 Sponsored by Advanced Research Projects Agency, 30 April 1967, (SECRET).

[4] A. R. Djordjević, M. B. Baždar, G. M. Vitošević, T. K. Sarkar, and R. F. Harrington. *Analysis of Wire Antennas and Scatters: Software and Users Manual*. Artech House, Inc., 685 Canton St., Norwood, Massachusetts 02062, 1990.

[5] Ronald M. Cionco and John H. Byers. *High Resolution Wind Program and HRWGRAPH Analysis Program User's Guide*. Army Research Laboratory, Battlefield Environment Directorate, White Sands Missile Range, New Mexico, November 1994.

[6] F. L. Ludwig and R. M. Endlich. *User's Guide for the Winds on Critical Streamline Surfaces (WOCSS) Code*. Atmospheric Sciences and Effects Program, SRI International, Menlo Park, California 94025, May 1988.

[7] H. W. Maynard, D. W. Hoock, F. V. Hansen, and T. Henmi. Simulation of Aerosol Behavior in Realistic Environments SABRE. Technical Report TR-0221-12, U.S. Army Laboratory Command, Atmospheric Sciences Laboratory, White Sands Missile Range, New Mexico, October 1987. EOSAEL Volume 12.

[8] D. W. Hoock, R. A. Sutherland, and D. Clayton. Combined Obscuration Model for Battlefield Induced Contaminants (COMBIC). Technical Report TR-0221-11, U.S. Army Laboratory Command, Atmospheric Sciences Laboratory, White Sands Missile Range, New Mexico, October 1987. EOSAEL Volume 11.

[9] Philip M. Bushong. Calculation of Concentration and Deposition for Gaussian Puffs and Plumes in SABRE/TDR-3.2. Technical Report NSWCDD/JTR-97/09, Naval Surface Warfare Center Dahlgren Division, Joint Warfare Applications Department, Dahlgren, Virginia, 1997. To Be Published.

[10] P. F. Lambeck, R. J. Brewer, and J. L. Manning. Transport, Diffusion, and Radiance Version 3.1. Technical Report OMI-545, OptiMetrics, Inc., 2107 Laurel Bush Road, Emmorton Professional Building, Bel Air, Maryland 21015, October 1994. Contract DAAA15-91-C-0144.

[11] Scarlett D. Ayres and Stephen DeSutter. *Combined Obscuration Model for Battlefield Induced Contaminants (COMBIC92) Model Documentation*. U.S. Army Research Laboratory, Battlefield Environment Directorate, White Sands Missile Range, New Mexico, July 1994.

[12] The Khoros System, an Open Software Package, is available by ftp from ftp.khoros.unm.edu in source form, or on CDROM from Khoral Research, Inc. Contact via email at info@khoros.com.

[13] David P. Ramer, Gregg E. Irvin, Harry H. Heaton, and David A. Malek. Multispectral Aerosol Obscurant Effects on Synthetic Aperture Radar Target Acquisition Study. Technical Report Contract Number DAAM01-95-C-0010, Aerospace Systems Division, Science Applications International Corporation, 1321 Research Park Drive, Dayton, Ohio 45432, February 1996.

[14] Underground C^{3}I Facility (Type B Hardened Structure) Characterization for the Enhanced Weapons Program. Technical report, Defense Nuclear Agency, Alexandria, Virginia, June 1993.

[15] D. A. Cataldo, C. J. Driver, M. W. Ligotke, W. G. Landis, and M. V. Norton. Environmental and Health Effects Review for Obscurant Fibers/Filaments. Technical Report CRDEC-CR-126, Pacific Northwest Laboratory, Richland, Washington, January 1992.

[16] H. Rick Blacksten and Thomas Yencha. *User's Manual VENM*. Technical Analysis and Information Office, U.S. Army Dugway Proving Ground, Dugway, Utah, November 1989.

[17] George N. Walton. *CONTAM93 User Manual, NISTIR 5385*. United States Department of Commerce, Technology Administration, National Institute of Standards and Technology, Building and Fire Research Laboratory, Gaithersburg, Maryland, December 1993.

[18] Smoke and Obscurants Engineering Handbook, Volume III: Smoke Production Methods. Technical Report ETI-TR-1138-09B, Engineering Technology Incorporated, 3275 Progress Drive, Orlando, Florida 32826, September 1995. Submitted to U.S. Army Edgewood Research, Development and Engineering Center, via Contract No. DAAA15-91-C-0098.

[19] J. Roderick Chapman, Arthur E. Hanzo, Terance W. Hoehn, and Daniel J. Hartman. DAT and SPOT — Novel Tools For Real Time Obscurant Concentration Measurement. In *Proceedings of the Smoke/Obscurants Symposium XIX*, June 1996. Sponsored by the Chemical and Biological Defense Agency, Aberdeen Proving Ground, Maryland.

APPENDIX A
Baseline Inputs To The Smooth Terrain Wind Field Generator

THIS PAGE INTENTIONALLY LEFT BLANK

```
$smoothin
  hbar = 0.0,
  z0bar = 0.01,
  dxy = 10.0,
  ustbar(1) = 0.519,
  hs(1) = 150.0,
  tbar(1) = 300.0,
  hpbl(1) = 200.,
  ubar = 5.98,
  vbar(1) = 0.0,
  pexp(1) = 0.15,
$end
```

THIS PAGE INTENTIONALLY LEFT BLANK

APPENDIX B
Baseline Inputs To The Phase I Transport And Diffusion Model

THIS PAGE INTENTIONALLY LEFT BLANK

```
$sab1in
  nsorc=216,
  combic_sig=1,
  source_type(1)=
    1, 1, 1, 1, 1, 1, 1, 1, 1, 1, 1, 1, 1, 1, 1, 1, 1, 1, 1, 1, 1, 1, 1, 1,
    1, 1, 1, 1, 1, 1, 1, 1, 1, 1, 1, 1, 1, 1, 1, 1, 1, 1, 1, 1, 1, 1, 1, 1,
    1, 1, 1, 1, 1, 1, 1, 1, 1, 1, 1, 1, 1, 1, 1, 1, 1, 1, 1, 1, 1, 1, 1, 1,
    1, 1, 1, 1, 1, 1, 1, 1, 1, 1, 1, 1, 1, 1, 1, 1, 1, 1, 1, 1, 1, 1, 1, 1,
    1, 1, 1, 1, 1, 1, 1, 1, 1, 1, 1, 1, 1, 1, 1, 1, 1, 1, 1, 1, 1, 1, 1, 1,
    1, 1, 1, 1, 1, 1, 1, 1, 1, 1, 1, 1, 1, 1, 1, 1, 1, 1, 1, 1, 1, 1, 1, 1,
    1, 1, 1, 1, 1, 1, 1, 1, 1, 1, 1, 1, 1, 1, 1, 1, 1, 1, 1, 1, 1, 1, 1, 1,
    1, 1, 1, 1, 1, 1, 1, 1, 1, 1, 1, 1, 1, 1, 1, 1, 1, 1, 1, 1, 1, 1, 1, 1,
    1, 1, 1, 1, 1, 1, 1, 1, 1, 1, 1, 1, 1, 1, 1, 1, 1, 1, 1, 1, 1, 1, 1, 1,

  xs=69.6450040637, 88.2661662073, 208.299069047, 39.2490170089,
     87.7141683742, 123.979719314, 90.3659953135, 53.6024756994,
     52.0713057655, 120.887843419, 108.951613863, 209.418397401,
     117.128677528, 201.702545156, 161.058449149, 120.84476826,
     208.227720524, 172.007642415, 73.084250639, 93.6016911077,
     23.7846386696, 55.3015097127, 62.6705464374, 41.4718663189,
     104.21387596, 18.5601832353, 116.522393238, 30.9584412166,
     94.8491415313, 46.7049893669, 144.524870371, 96.8872038185,
     161.55762694, 35.3193726778, 111.056706701, 79.9377277244,
     58.3386182873, 157.031123577, 207.603136903, 131.269004396,
     92.2506896061, 120.323043382, 178.422415327, 134.059684914,
     77.0223166814, 158.183787406, 72.8540678967, 65.7926309485,
     23.3973108352, 153.93190549, 203.645782273, 61.4961912446,
     159.497136689, 91.4395292045, 161.36549851, 108.445073209,
     20.5435769891, 174.817399501, 150.618665654, 83.9104017171,
     108.51783027, 172.058583079, 79.3132729594, 193.288171114,
     73.2491384837, 132.236237613, 30.019359748, 116.983558487,
     95.5449428582, 186.939095874, 22.9052256593, 130.174783343,
     65.3112516235, 151.856132929, 171.307355483, 34.0985412728,
     142.220542797, 156.222089634, 157.725514819, 151.225460965,
     27.7304627059, 194.811998841, 169.056149295, 217.530677571,
     136.523570698, 174.219844449, 46.1756397778, 18.0848094644,
     142.42025988, 141.458063613, 88.6012324403, 137.020269487,
     196.198099765, 139.544589165, 188.084015294, 199.820318077,
     168.372639959, 128.411759665, 116.740286394, 175.404823997,
     97.11055213, 130.400558313, 107.994258318, 148.19546752, 152.152349828,
     83.404471374, 75.801710271, 131.62422917, 171.666216851, 178.462412864,
     45.9729696783, 167.516612429, 121.775369205, 30.9392985433,
     214.865125116, 219.531023475, 145.561458262, 194.30921658,
     121.020506392, 22.3572172468, 205.494022041, 4.807357123, 182.46092032,
     106.785646921, 67.3995107868, 198.06133778, 97.6411853088,
     106.62432742, 115.719885852, 80.9894058677, 136.954505665,
     81.5025673052, 84.7533418457, 153.377170637, 35.2948043943,
     155.65393189, 100.524841157, 2.327010087, 149.808862625, 44.4641211503,
     15.6420452217, 165.912595118, 129.177559084, 66.9236353635,
     123.570848384, 206.988171945, 172.994941315, 150.739740219,
     130.216187136, 196.820137863, 198.645413642, 198.353780302,
     16.2168862809, 157.573722775, 150.538023837, 188.709054353,
     116.570427391, 22.0656048423, 111.428524097, 29.8804198891,
     53.525407806, 205.084916787, 52.2818688097, 135.59888622,
```

57.1841608244, 121.608896971, 90.6866311482, 27.822267314,
70.1283640694, 153.658063641, 99.7252279007, 133.480595622,
186.41313812, 96.9777359654, 10.1750931308, 107.123464103,
184.513793857, 82.4021529053, 120.822841739, 172.636242924,
6.895667647, 189.80827639, 90.0938178149, 198.864605516, 64.8495275785,
35.2229527597, 48.2701969297, 154.679519862, 15.7498200704,
176.756682592, 12.5351822518, 143.46403033, 82.7955567205,
71.412329949, 28.1269262836, 137.227768438, 112.989309103,
88.3427590271, 55.0228404033, 158.790025819, 141.715670705,
172.742713008, 7.784849275, 171.439979651, 21.335840811, 88.4523386344,
148.549323738, 57.5994720362, 34.7732039483, 174.100989086,
150.77578535, 93.2698238817, 171.044179085, 176.250418495,
57.3462926126, 53.5542526402,

ys=160.292360355, 179.030843368, 111.796767438, 72.5626897284,
60.0888849316, 140.088988225, 81.5746716348, 173.584692336,
182.564098206, 227.5102547, 114.624045526, 127.998891069,
190.534969743, 87.7720119784, 84.3063763333, 154.689926512,
109.215060467, 199.177347026, 105.295325603, 24.2393845807,
113.682447414, 59.8828214211, 138.382677321, 160.42146576,
165.370924264, 139.640771626, 198.488587619, 91.5143547536,
139.090612553, 178.298727507, 22.5216263689, 70.2299831594,
194.066261579, 136.395240247, 167.873618737, 115.389166493,
192.966441873, 205.755894346, 74.2984938233, 158.205097199,
208.729713065, 126.436984956, 112.763075181, 171.595848301,
155.797659183, 34.1668908219, 150.841201795, 140.632705144,
156.427657479, 180.802859144, 130.269735272, 181.590425686,
153.015654765, 112.823028226, 32.076251429, 91.3541939775,
157.007409827, 112.536440396, 21.1560623991, 97.5649189562,
20.622924309, 198.604912482, 211.669650286, 164.441878363,
132.781790869, 220.864016065, 114.605819349, 189.872955504,
184.055064773, 80.8544315896, 162.314303522, 213.957320721,
89.7193829563, 73.6527871793, 126.663945059, 41.4063071036,
194.751833569, 188.545739692, 131.885925934, 43.1920487954,
140.315590895, 112.794109862, 73.4449655736, 109.600318215,
214.53835305, 50.4600001511, 58.4252402178, 63.6919388654,
97.3080025266, 166.769543869, 205.305877564, 121.704416864,
88.3315993934, 118.544922317, 167.189898872, 63.5348739441,
129.981728516, 142.516818293, 42.9508693149, 77.2424392891,
83.6563329642, 13.642972867, 115.103368474, 76.1125728601,
118.523719559, 168.15265161, 63.5245453351, 40.675396548,
184.072441028, 64.6023644475, 190.912194919, 63.3886999377,
225.329676161, 94.812592726, 121.142599894, 129.217098051,
18.292661591, 74.0004782662, 173.371794413, 182.054352234,
156.998537194, 126.442661302, 125.330574675, 87.1569195372,
198.607876952, 61.0831026921, 133.124774262, 211.398057062,
158.305128976, 14.385676028, 75.8134112614, 62.018137924,
169.564162981, 136.625915539, 165.597519116, 118.689083139,
16.225140979, 137.931180754, 137.727223598, 180.166839566,
123.684612606, 90.7633499321, 158.797180666, 157.167550494,
63.9568730873, 166.789897445, 45.4169096326, 45.1516628982,
52.5662860457, 86.2026086588, 169.071281217, 102.375882819,
97.9380966106, 163.402084066, 153.296675861, 97.4193719563,
26.4862069858, 157.07481825, 121.720267102, 164.405550136,

```
     119.212322065, 77.6814626964, 27.1419506346, 194.650499157,
     216.002537114, 227.722947932, 203.767498373, 101.647336689,
     116.798024326, 162.213427711, 112.35610974, 19.906735345,
     77.7740326018, 37.6081275889, 112.859413985, 156.62957195,
     82.8961656288, 127.304713255, 89.375400465, 122.16819565,
     141.943031926, 113.783970743, 227.678892597, 59.8162655983,
     180.418828523, 43.5840775366, 125.237500636, 135.897814469,
     130.858341643, 200.315287022, 74.4850650741, 152.173881862,
     92.5242240172, 154.828030666, 142.063540066, 139.586950398,
     62.1634714813, 224.837798115, 116.757790463, 55.5210625038,
     147.461176809, 136.073330843, 149.783602237, 138.059039301,
     184.642608822, 154.520983324, 93.1308794463, 49.8488441356,
     48.7333938235, 41.8395035948, 211.740587141, 93.3898288797,
     92.5116715708, 138.381568194, 205.320496356, 114.533958928,


zs=3., 3., 3., 3., 3., 3., 3., 3., 3., 3., 3., 3., 3., 3., 3., 3., 3., 3.,
   3., 3., 3., 3., 3., 3., 3., 3., 3., 3., 3., 3., 3., 3., 3., 3., 3., 3.,
   3., 3., 3., 3., 3., 3., 3., 3., 3., 3., 3., 3., 3., 3., 3., 3., 3., 3.,
   3., 3., 3., 3., 3., 3., 3., 3., 3., 3., 3., 3., 3., 3., 3., 3., 3., 3.,
   3., 3., 3., 3., 3., 3., 3., 3., 3., 3., 3., 3., 3., 3., 3., 3., 3., 3.,
   3., 3., 3., 3., 3., 3., 3., 3., 3., 3., 3., 3., 3., 3., 3., 3., 3., 3.,
   3., 3., 3., 3., 3., 3., 3., 3., 3., 3., 3., 3., 3., 3., 3., 3., 3., 3.,
   3., 3., 3., 3., 3., 3., 3., 3., 3., 3., 3., 3., 3., 3., 3., 3., 3., 3.,
   3., 3., 3., 3., 3., 3., 3., 3., 3., 3., 3., 3., 3., 3., 3., 3., 3., 3.,
   3., 3., 3., 3., 3., 3., 3., 3., 3., 3., 3., 3., 3., 3., 3., 3., 3., 3.,
   3., 3., 3., 3., 3., 3., 3., 3., 3., 3., 3., 3., 3., 3., 3., 3., 3., 3.,
   3., 3., 3., 3., 3., 3., 3., 3., 3., 3., 3., 3., 3., 3., 3., 3., 3., 3.,

nistyp=1,
itypma(1)=0,0,
itypsa(1)=13,13,
temp0a(1)=300.0,300.0,
effa(1)= 75.0,010.0,
yfa(1)=1.0,1.0,
tburna=9.,

fwa(1)=1236749,0.22045,

brat1a(1)=1.0,1.0, brat2a(1)=0.0,0.0, brat3a(1)=0.0,0.0,
brat4a(1)=0.0,0.0, brat5a(1)=0.0,0.0, brat6a(1)=0.0,0.0,

uqfaca(1)=0.0,0.0,
uxinsta(1)=1.0,1.0,
uscava(1)=0.00,00.0,
ufalva(1)=0.010,0.125
usurfrefa(1)=0.0,0.5
usigxaa(1)=3.0,1.0,
usigyaa(1)=3.0,1.0,
usigzaa(1)=3.0,1.0,
$end
```

THIS PAGE INTENTIONALLY LEFT BLANK

APPENDIX C
Baseline Inputs To The Phase II Line-of-Sight Transmission Model

THIS PAGE INTENTIONALLY LEFT BLANK

```
$sab2in
  image=        .true.
  h_fov=        15,
  v_fov=        15,
  nv_pix=        60,
  nh_pix=        60,
  nsrcs=        216,
  bgnsrc(1)=        52.6753620424, 50.5151832727, 51.1029623674, 53.1970522687,
    51.5959562732, 52.8294035777, 51.4494686372, 51.3409902874,
    51.711774195, 50.8377572473, 52.8232804912, 53.0892465061,
    52.3526601971, 53.040756573, 52.1297615834, 51.6623954314,
    51.3519944506, 52.4781965303, 51.0540462653, 50.1702144672,
    51.37084446, 52.8532900132, 51.4806356632, 51.1910669847,
    53.1253497952, 52.5679811753, 53.173213029, 52.8216001575,
    50.4599307457, 50.5332716819, 51.2926892631, 52.4406541499,
    51.8978440773, 52.4286482903, 51.8637782755, 53.1932922402,
    52.7605347673, 52.4250117422, 50.7920117138, 49.9250633216,
    50.1429669984, 50.2610095432, 49.9910069697, 53.1772192097,
    51.2369977459, 52.6682393464, 52.1958241388, 51.7254539579,
    50.5714621347, 52.9612308302, 52.8938358838, 50.4525230985,
    49.8720779199, 52.7666105773, 52.9897361875, 52.9957588182,
    50.2473220388, 52.1407474724, 50.3507446053, 52.4904771869,
    51.4791310006, 50.2597530138, 52.6249851857, 53.1204939633,
    51.7639298445, 49.8603374771, 52.7256799318, 50.6543352585,
    50.7261322316, 51.5214242351, 51.3825814533, 52.233334047,
    52.861542248, 52.6860019141, 51.5811883175, 52.5790764471,
    51.7654884071, 52.7365407337, 51.4654622813, 52.2321901317,
    50.2324745942, 50.8481664287, 52.3467289249, 51.6483991967,
    52.8262577383, 53.1637017299, 51.5800874213, 49.9308729693,
    51.0035979561, 50.8172900199, 51.7033229341, 51.3491236714,
    52.6148018578, 51.9012237846, 52.5214820293, 52.373212524,
    51.1627470607, 51.2803288353, 50.4061797725, 51.6033111227,
    51.9791921522, 52.4437823214, 51.8462609535, 52.7551203707,
    52.3003060084, 50.0364522661, 49.9142713391, 50.0719916993,
    49.820825784, 52.5716725584, 51.9541857886, 51.0644956541,
    52.0079095821, 52.7220992928, 50.6516911858, 52.0137483709,
    52.1159901091, 51.1011240734, 50.3184807992, 50.3162350348,
    52.8669155501, 51.526730697, 52.7473247453, 53.1177534115,
    51.8195364115, 50.863572205, 53.0485797117, 51.4585271878,
    51.2283960409, 51.0079286912, 50.268995483, 51.3957150677,
    52.3504992961, 53.1843392199, 51.1395221667, 52.4576660419,
    51.0866349234, 51.0145521607, 52.039808487, 50.0574032628,
    51.623471538, 53.0335286708, 52.5512635144, 51.4493629283,
    50.1847843051, 51.3384775636, 51.204499136, 52.7987536459,
    50.1674492194, 51.8657047564, 52.679149204, 49.9768887515,
    51.7239544484, 53.1678856184, 50.0269054325, 50.0737932506,
    51.9966438354, 53.1916279953, 53.0218772464, 50.179781299,
    51.1818755604, 50.3583219475, 50.0314514495, 52.7907755813,
    50.1519102993, 52.0395877958, 51.4978550201, 52.4909494468,
    52.6352364048, 51.9270005554, 51.9486437664, 50.7368393352,
    51.9065390173, 51.9296910813, 50.9649344448, 50.7335301719,
    50.2269177545, 52.9737980428, 50.2083528241, 52.2165336594,
    52.2598763753, 50.282917235, 52.7788337423, 50.2909856597,
    50.2390395981, 50.7247124507, 52.875066475, 53.1084708859,
```

```
53.1409905351, 52.0057683605, 51.0086138453, 51.9414543856,
51.2413113904, 50.5370255533, 49.8536819399, 51.8790309744,
52.3816833228, 52.9992614714, 51.9983034758, 49.8936796158,
50.2405995451, 52.1160338948, 50.6535627741, 51.8132147539,
51.6709995317, 51.8670831787, 50.1608891333, 50.8055211648,
50.2675850298, 49.8300376134, 52.0452052432, 51.9517980779,
53.1686672813, 49.9762987939, 51.6126963807, 52.9673418301,

bgnlos=          110,
endlos=          110,
tstep=           1,

xobs=            400.,
yobs=            120.,
zobs=            1368.7.,

xtgt=            400,
ytgt=            120,
ztgt=            1.5,

iband=           0,
numtt=           1,
ttcoef=           0.0000015836,
ttwave=           8.00, 12.0,
ttresp=           1.0,

clytp=           15,
a(2)=            1.3,1.37,1.38,2.4,2.7,2.62,

$end
```

APPENDIX D
Baseline Inputs To The Phase III Concentration, Exposure, and Deposition Model

THIS PAGE INTENTIONALLY LEFT BLANK

```
$sab3in
  bgnbat=      0,
  endbat=      301,

  tbegin=      49.0,
  tend=        200.0,
  tstep=       1.,

  xbegin=      286.5,
  xstep=       1,
  xend=        286.5,

  ybegin=      120.0,
  ystep=       1.0,
  yend=        120.0,

  zhigh=       1.5,
  tspout=      1.,

  bgnsrc(1)=   52.6753620424, 50.5151832727, 51.1029623674, 53.1970522687,
    51.5959562732, 52.8294035777, 51.4494686372, 51.3409902874,
    51.711774195, 50.8377572473, 52.8232804912, 53.0892465061,
    52.3526601971, 53.040756573, 52.1297615834, 51.6623954314,
    51.3519944506, 52.4781965303, 51.0540462653, 50.1702144672,
    51.37084446, 52.8532900132, 51.4806356632, 51.1910669847,
    53.1253497952, 52.5679811753, 53.173213029, 52.8216001575,
    50.4599307457, 50.5332716819, 51.2926892631, 52.4406541499,
    51.8978440773, 52.4286482903, 51.8637782755, 53.1932922402,
    52.7605347673, 52.4250117422, 50.7920117138, 49.9250633216,
    50.1429669984, 50.2610095432, 49.9910069697, 53.1772192097,
    51.2369977459, 52.6682393464, 52.1958241388, 51.7254539579,
    50.5714621347, 52.9612308302, 52.8938358838, 50.4525230985,
    49.8720779199, 52.7666105773, 52.9897361875, 52.9957588182,
    50.2473220388, 52.1407474724, 50.3507446053, 52.4904771869,
    51.4791310006, 50.2597530138, 52.6249851857, 53.1204939633,
    51.7639298445, 49.8603374771, 52.7256799318, 50.6543352585,
    50.7261322316, 51.5214242351, 51.3825814533, 52.233334047,
    52.861542248, 52.6860019141, 51.5811883175, 52.5790764471,
    51.7654884071, 52.7365407337, 51.4654622813, 52.2321901317,
    50.2324745942, 50.8481664287, 52.3467289249, 51.6483991967,
    52.8262577383, 53.1637017299, 51.5800874213, 49.9308729693,
    51.0035979561, 50.8172900199, 51.7033229341, 51.3491236714,
    52.6148018578, 51.9012237846, 52.5214820293, 52.373212524,
    51.1627470607, 51.2803288353, 50.4061797725, 51.6033111227,
    51.9791921522, 52.4437823214, 51.8462609535, 52.7551203707,
    52.3003060084, 50.0364522661, 49.9142713391, 50.0719916993,
    49.820825784, 52.5716725584, 51.9541857886, 51.0644956541,
    52.0079095821, 52.7220992928, 50.6516911858, 52.0137483709,
    52.1159901091, 51.1011240734, 50.3184807992, 50.3162350348,
    52.8669155501, 51.526730697, 52.7473247453, 53.1177534115,
    51.8195364115, 50.863572205, 53.0485797117, 51.4585271878,
    51.2283960409, 51.0079286912, 50.268995483, 51.3957150677,
    52.3504992961, 53.1843392199, 51.1395221667, 52.4576660419,
    51.0866349234, 51.0145521607, 52.039808487, 50.0574032628,
```

```
 51.623471538, 53.0335286708, 52.5512635144, 51.4493629283,
 50.1847843051, 51.3384775636, 51.204499136, 52.7987536459,
 50.1674492194, 51.8657047564, 52.679149204, 49.9768887515,
 51.7239544484, 53.1678856184, 50.0269054325, 50.0737932506,
 51.9966438354, 53.1916279953, 53.0218772464, 50.179781299,
 51.1818755604, 50.3583219475, 50.0314514495, 52.7907755813,
 50.1519102993, 52.0395877958, 51.4978550201, 52.4909494468,
 52.6352364048, 51.9270005554, 51.9486437664, 50.7368393352,
 51.9065390173, 51.9296910813, 50.9649344448, 50.7335301719,
 50.2269177545, 52.9737980428, 50.2083528241, 52.2165336594,
 52.2598763753, 50.282917235, 52.7788337423, 50.2909856597,
 50.2390395981, 50.7247124507, 52.875066475, 53.1084708859,
 53.1409905351, 52.0057683605, 51.0086138453, 51.9414543856,
 51.2413113904, 50.5370255533, 49.8536819399, 51.8790309744,
 52.3816833228, 52.9992614714, 51.9983034758, 49.8936796158,
 50.2405995451, 52.1160338948, 50.6535627741, 51.8132147539,
 51.6709995317, 51.8670831787, 50.1608891333, 50.8055211648,
 50.2675850298, 49.8300376134, 52.0452052432, 51.9517980779,
 53.1686672813, 49.9762987939, 51.6126963807, 52.9673418301,
$end
```

DISTRIBUTION

	Copies

DOD ACTIVITIES (CONUS)

ATTN DR JON MARTIN   1
UNITED STATES ARMY RESEARCH LABORATORY
PROVISIONAL AMSRL BE E
WHITE SANDS MISSILE RANGE NM 88002-5513

ATTN DR JIM KVACH   1
      DR PATTON ALLEN   1
      DR HELEN BENET   1
ARMED FORCES MEDICAL INTELLIGENCE CENTER
DEFENSE INTELLIGENCE AGENCY
BUILDING 1607
FT DIETRICK MD 21702-5004

ATTN BOB BROCK   1
PROGRAM EXECUTIVE OFFICE
GLOBAL PROTECTION AGAINST LIMITED STRIKES
SFAE GPL SM E HS
HUNTSVILLE AL 35807-3801

ATTN MAJ SHERYL R MILLER   1
      MAJ JERRY GLASOW DAMO FDB   1
UNITED STATES ARMY CONCEPTS ANALYSIS AGENCY
8120 WOODMONT AVENUE
BETHESDA MD 20814-2797

ATTN JOHN D'ERRICO   1
COMMANDANT
UNITED STATES ARMY INFANTRY SCHOOL
ATSH WCS J
FORT BENNING GA 31905-5400

ATTN N541 CHRIS DIAMOND   1
COMMANDING OFFICER
NAVAL OCEANOGRAPHIC OFFICE
1002 BALCH BOULEVARD
STENNIS SPACE CENTER MS 39522-5001

ATTN DOUGLAS P SCHULTZ   1
      ELEANOR SCHWARTZ   1
INSTITUTE FOR DEFENSE ANALYSES
1801 N BEAUREGARD STREET
ALEXANDRIA VA 22311

DISTRIBUTION (CONTINUED)

Copies

ATTN CPT MILLER   1
      MAJ SIMCHIK   1
UNITED STATES ARMY CHEMICAL SCHOOL
ATZN CM CC
FT MCCLELLAN AL 36205-5020

ATTN LTC A J KUEHN CODE SPWE   1
      LEON WITWER   1
      JAMES GERDING   1
      ROB KEHLET   1
DEFENSE SPECIAL WEAPONS AGENCY
6801 TELEGRAPH ROAD
ALEXANDRIA VA 22310-3398

ATTN DR CLYDE REPLOGLE   1
COMMANDER UNITED STATES AIR FORCE
ARMSTRONG LABORATORY CFDA
2245 MONAHAN WAY BUILDING 29
WRIGHT PATTERSON AIR FORCE BASE OH 45433-7008

ATTN DR MICHAEL ROSENE   1
COMMANDER NATIONAL GROUND INTELLIGENCE CENTER
220 SEVENTH STREET NE
CHEMICAL AND LIFE SCIENCES BRANCH
CHARLOTTESVILLE VA 22902-5396

ATTN N67 FLEASWTRACENPAC   1
      AGC JIM HRABOVSKY   1
      CHIEF DUCKSTEAD   1
DIRECTOR NAVAL OCEANOGRAPHIC OFFICE
PACIFIC COMPONENT
SAN DIEGO CA 92147-5000

ATTN DR WALTER BACH   1
DEPARTMENT OF THE ARMY
ARMY RESEARCH OFFICE
PO BOX 12211
RESEARCH TRIANGLE PARK NC 27709-2211

ATTN CHARLIE HOLMAN   1
UNITED STATES ARMY OPERATIONAL TEST AND
EVALUATION COMMAND PARK CENTER IV
4501 FORD AVENUE SUITE 780 CSTE ECS A
ALEXANDRIA VA 22302-1458

DISTRIBUTION (CONTINUED)

Copies

ATTN DR JAMES M OLIVER	1
JOE NORMAN	1
UNITED STATES ARMY MISSILE COMMAND	
AMSMI RD SS AA	
REDSTONE ARSENAL AL 35898-5000	

ATTN RUSSELL DOUTHETT   1
NATIONAL TEST FACILITY PDS
730 IRWIN AVENUE
FALCON AIR FORCE BASE CO 80912-7300

ATTN LOUIS DOMINGUEZ   1
DIRECTOR UNITED STATES ARMY TRAINING AND
DOCTRINE COMMAND ANALYSIS CENTER
WHITE SANDS MISSILE RANGE NM 88002-5502

ATTN GARY LOVE   1
COMMANDING OFFICER
NAVAL RESEARCH LABORATORY
MONTEREY CA 93943-5000

ATTN DR SAL BOSCO   1
    DR TED PROCIV   1
OFFICE OF THE SECRETARY OF DEFENSE OSD AE
OFFICE OF THE DEPUTY ASSISTANT FOR CHEMICAL MATTERS
PENTAGON ROOM 3E1074
WASHINGTON DC 20301-3050

ATTN DALE SLOOP   1
    RICK ZUM BRUNNEN   1
    ROBERT V JOLLIFFE   1
    J TERRENCE KLOPCIC   1
    BRIAN G SMITH AMSRL SL CS   1
    LYNN DAVIS   1
UNITED STATES ARMY RESEARCH LABORATORY
AMSRL SL CM
ABERDEEN PROVING GROUND MD 21010-5423

ATTN PMW 31 GREG MELCHER   1
DEPARTMENT OF THE NAVY
SPACE AND NAVAL WARFARE SYSTEMS COMMAND
WASHINGTON DC 20363-5100

DISTRIBUTION (CONTINUED)

Copies

ATTN LCDR BILL SAMPSON UNITED STATES STRATEGIC COMMAND 901 SAC BOULEVARD SUITE 2E8 OFFUTT AIR FORCE BASE NE 68113-6500	1
ATTN C MEYERHOFF SY71A COMMANDER NAVAL AIR WARFARE CENTER AIRCRAFT DIVISION SYSTEMS ENGINEERING TEST DIRECTORATE BUILDING 2109 PATUXENT RIVER MD 20670-5304	1

ATTN GEORGE R FAMINI   1
    JOHN GREEN   1
    MIKE MYIRSKI   1
    DICK SICKENBERGER   1
    DENNIS FLANIGAN   1
    C R CRAWFORD   1
    AL SEITZINGER SCBRD RTB   1
    JOHN ASTARITA SCBRD RTM   1
    STEVE GOTOFF   1
    ROBERT KROUTIL SCBRD RT   1
    DR JOHN R WHITE   1
    DR PAUL FEDELE   1
DEPARTMENT OF THE ARMY
EDGEWOOD RESEARCH DEVELOPMENT AND ENGINEERING CENTER
ABERDEEN PROVING GROUND MD 21010-5423

ATTN MAJ PAT CHRISTIAN   1
    MAJ JIM DEMYANOVICH   1
UNITED STATES ARMY NUCLEAR AND CHEMICAL AGENCY
7500 BACKLICK ROAD BUILDING 2073
SPRINGFIELD VA 22150-319

ATTN PATRICK DUGGAN CSSD SA A   1
    DR JULIUS LILLY CSSD WD L   1
    ROBERT WOOD CSSD SA A   1
COMMANDER
UNITED STATES ARMY SPACE AND STRATEGIC DEFENSE COMMAND
LETHALITY DIVISION WEAPONS DIVISION
PO BOX 1500
HUNTSVILLE AL 35807-3801

DISTRIBUTION (CONTINUED)

Copies

ATTN CSSD SA ES DAVID L TILSON   1
COMMANDER
UNITED STATES ARMY SPACE AND STRATEGIC DEFENSE COMMAND
SYSTEMS DIRECTORATE SYSTEMS ENGINEERING DIVISION
SYSTEMS ENGINEERING BRANCH
HUNTSVILLE AL 35807-3801

ATTN N86D CHUCK BOGNER   1
CHIEF OF NAVAL OPERATIONS
2000 NAVY PENTAGON
WASHINGTON DC 20350-2000

ATTN ROBERT A HUME JR   1
DEPARTMENT OF THE AIR FORCE
AERONAUTICAL SYSTEMS CENTER AFMC ASC YOX
102W D AVENUE SUITE 300
EGLIN AIR FORCE BASE FL 32542-6808

ATTN LUIS A SANTANA   1
WRIGHT LABORATORY ARMAMENT DIRECTORATE
WL MNOE
101 W EGLIN BOULEVARD SUITE 238
EGLIN AFB FL 32542-6810

ATTN KIRK HERZOG   1
WRIGHT LABORATORY ARMAMENT DIRECTORATE
WL MNSN
101 W EGLIN BOULEVARD SUITE 250
EGLIN AFB FL 32542-6810

ATTN N14B HICKMAN   1
COMMANDER MILITARY SEALIFT COMMAND
WASHINGTON NAVY YARD
BUILDING 210 901 M STREET SE
WASHINGTON DC 20398-5540

ATTN CAPT LUNSFORD   1
DEFENSE INFORMATION SYSTEMS AGENCY
7010 DEFENSE PENTAGON
ROOM ME 670
WASHINGTON DC 20301-7010

DISTRIBUTION (CONTINUED)

Copies

ATTN N393B AGCS KOHN   1
NAVAL OCEANOGRAPHIC OFFICE
ATLANTIC COMPONENT FLEET TRAINING CENTER
9550 FARRAGUT AVENUE
NORFOLK VA 23511-2790

ATTN LTC PAUL W COUTEE   1
DEPARTMENT OF THE AIR FORCE
WL MNSA
101 WEST EGLIN BLVD
SUITE 326
EGLIN AFB FL 32542-6810

ATTN DR MARCUS BUNTING   1
SANDIA NATIONAL LABORATORIES
STRATEGIC DEFENSE STUDIES DEPARTMENT
PO BOX 5800 M S 0423
ALBUQUERQUE NM 87185-0423

ATTN MAJ FRANK WOLF   1
HEADQUARTERS
UNITED STATES AIR FORCE XOXI
1480 AIR FORCE PENTAGON ROOM 1D373
WASHINGTON D C 20330-1480

ATTN DOUGLAS BONFORTE   1
BALLISTIC MISSILE DEFENSE ORGANIZATION
7100 DEFENSE PENTAGON
WASHINGTON DC 20301-7100

ATTN CAPT DUBUQUE   1
FCDNA FCPRA
1680 TEXAS STREET SE
KIRTLAND AFB NM 87117-5616

ATTN DONALD M LITTRELL   1
UNITED STATES AIR FORCE WARHEADS BRANCH
MUNITIONS DIVISION ARMAMENT DIRECTORATE
WRIGHT LABORATORY
EGLIN AIR FORCE BASE FL 32542-6810

ATTN DANIEL MCGRATH   1
COMMANDER
US ARMY ARDEC AMSTA AR FSS
BUILDING 94
PICATINNY ARSENAL NJ 07806-5000

DISTRIBUTION (CONTINUED)

Copies

ATTN LTC JIM MARTIN   1
PERSIAN GULF TASK FORCE
SKYLINE 1 ROOM 810
5205 LEESBURG PIKE
FALLS CHURCH VA 22041

ATTN MAJ TONY FRANCIS DAMO FDB   1
HQDA
DCSOPS
PENTAGON 3C549
WASHINGTON DC 20310

ATTN MARK J ORMSBY ONI 232   1
     MRS JANET L ANDERSON ONI 232   1
OFFICE OF NAVAL INTELLIGENCE
4251 SUITLAND ROAD
WASHINGTON DC 20395

ATTN STEDPWDM JIM BOWERS   1
COMMANDER
WEST DESERT TEST CENTER
BLDG 4034
DUGWAY PROVING GROUND UT 84022-5000

ATTN MIKE CAROTHERS AMXSY CB   1
DIRECTOR
US ARMY MATERIAL SYSTEMS ANALYSIS ACTIVITY
392 HOPKINS ROAD
ABERDEEN PROVING GROUND MD 21005-5071

MAJ JOHN SEES   1
10 4TH ARTILLERY ROAD
FT LEAVENWORTH KS 66027-1123

ATTN LOIS BENSON   1
DIAC
PAX 4
WASHINGTON DC 20340

ATTN LT HELMER   1
NAIC TABS
4180 WATSON WAY
WRIGHT PATTERSON AFB OH 45433-5648

DISTRIBUTION (CONTINUED)

Copies

ATTN JIM LETTERIO   1
PHILLIPS LABORATORY WSAT
3550 ABERDEEN SE
KIRTLAND AFB NM 87117-5776

ATTN LTC TIM MADREE   1
COMMANDER
USA TECH ESCORT UNIT
BUILDING E5422
ABERDEEN PROVING GROUND MD 21010-5423

ATTN CPT LESLIE DILLRED   1
310TH CHEMICAL COMPANY BIDS
B10 DETECTION
BUILDING 141B
FORT MCCLELLAN AL 36205-5000

ATTN DAVID EVANS   1
OFFICE OF ATSD NCB MATTERS
2451 CRYSTAL DRIVE SUITE 640
ARLINGTON VA 22002

ATTN SSC NC AA DALE MALABARBA   1
COMMANDER
US ARMY SOLDIER SYSTEM COMMAND
NATICK MA 01760-5015

ATTN J8 WAD LTC SHELLEY RICHARDSON   1
JOINT STAFF
PENTAGON ROOM 1D940
WASHINGTON DC 20318-8000

ATTN AMSTA AR FSS   1
COMMANDER
US ARMY ARDEC
PICATINNY ARSENAL NJ 07806-5000

ATTN EDWARD W STUEBING   1
TEAM LEADER AEROSOL SCIENCES
USA ERDEC SCBRD RTB E5951 STUEBING
5101 HOADLEY ROAD
ABERDEEN PROVING GROUND MD 21010-5423

DISTRIBUTION (CONTINUED)

	Copies
ATTN CAPT TODD M GESLING AFIT ENS BOX 4005 2950 P STREET BLDG 640 WRIGHT PATTERSON AFB OH 45433-7765	1
ATTN COL ELLEN M PAWLIKOWSKI ASSISTANT TO THE SECRETARY OF DEFENSE 3050 DEFENSE PENTAGON WASHINGTON DC 20301-3050	1
ATTN VAN CUNNINGHAM DAMO ZDS OFFICE OF THE TECHNICAL ADVISOR DEPUTY CHIEF OF STAFF FOR OPERATIONS AND PLANS HEADQUARTERS DEPARTMENT OF THE ARMY 400 ARMY PENTAGON WASHINGTON DC 20310-0400	1
ATTN CPT DRUSHAL B62 COMMANDER NATIONAL TRAINING CENTER ALPHA COMPANY OPERATION GROUP FORT IRWIN CA 92310	1

ATTN DR HAL GUARD ONR 341
    DR ERIC EISENSTADT ONR 341
    CDR E MARCINIK ONR 341
OFFICE OF NAVAL RESEARCH
BALLSTON TOWER ONE
800 N QUINCY STREET
ARLINGTON VA 22217-5660
	1
	1
	1

ATTN CDR TIMOTHY SHERIDAN PMW185 COMMANDER SPACE AND NAVAL WARFARE SYSTEMS COMMAND ARLINGTON VA 22245-5200	1
ATTN DOUGLAS SCHAEFFER AQT BALLISTIC MISSILE DEFENSE ORGANIZATION 7100 DEFENSE PENTAGON WASHINGTON DC 20302-7100	1

DISTRIBUTION (CONTINUED)

Copies

ATTN R JABLONSKI SCBRD RTM O   1
DEPARTMENT OF THE ARMY
EDGEWOOD RESEARCH DEVELOPMENT AND ENGINEERING CENTER
ABERDEEN PROVING GROUND MD 21010-5423

ATTN CPT DONALD CARLSTON   1
310TH CHEMICAL COMPANY BIDS
BUILDING 141B 13TH AVE
FORT MCCLELLAN AL 36205-5000

ATTN J54IX MARY G B PACE   1
USCINCPAC
BLDG 2AA RM 303
CAMP SMITH HI 96861-4105

ATTN DR MAURICE MIZRAHI   1
STRATEGIC STRIKE AND ARMS CONTROL PROGRAM DIVISION
OFFICE SECRETARY OF DEFENSE PROGRAM ANALYSIS AND EVALUATION
1800 DEFENSE
WASHINGTON DC 20301-1800

ATTN TIM MOSHIER   1
JPO BD
5201 LEESBURG PIKE
SKYLINE 3 SUITE 1200
FALLS CHURCH VA 22041

COL LARRY CEREGHINO
SKYLINE 8 SUITE 901
5118 LEESBURG PIKE
FALLS CHURCH VA 22041   1

ATTN RICHARD L WENDT   1
US ARMY SPACE STRATEGIC DEFENSE COMMAND
CSSD TC SR
PO BOX 1500
HUNTSVILLE AL 35807-3801

ATTN LT FRED GAGHAN UNDERSEA WARFARE   1
NAVAL POSTGRADUATE SCHOOL
2 UNIVERSITY SCHOOL
MONTEREY CA 93943-2983

DISTRIBUTION (CONTINUED)

	Copies
ATTN 418 R MARTINEZ NAVAL AIR WARFARE CENTER BLDG 2107 UNIT 5 PATUXENT RIVER MD 20670	1
ATTN W O STAMPER AGCS DIRECTOR NAVOCEANO ATLANTIC COMPONENT FLEET TRAINING CENTER CODE N396 9549 BAINBRIDGE AVENUE NORFOLK VA 23511-2594	1
ATTN DS 32 THOMAS PERFETTO PROJECT OFFICER MCTSSA NBC JWARN BOX 555171 CAMP PENDLETON CA 92055	1
ATTN BOB ANDREOLI STEWS NRES C WHITE SANDS MISSILE RANGE NM 88002	1
ATTN MCHB OC EES KIRKPATRICK USACHPPM BLDG E1675 ABERDEEN PROVING GROUND MD 21010-5422	1

DOD ACTIVITIES (EX-CONUS)

	Copies
ATTN LCDR G M MINEART USS ABRAHAM LINCOLN CVN 72 OPERATIONS DEPARTMENT OA DIVISION FPO AP 96612-2872	1
ATTN METOC OFFICER LCDR JIM ALLEN COMMANDING OFFICER USS CONSTELLATION CV 64 FPO AP 96635-2780	1
ATTN LCDR D TITLEY COMMANDER CARRIER GROUP 6 UNIT 60103 FPO AA 34099-4306	1

DISTRIBUTION (CONTINUED)

	Copies

ATTN METOC OFFICER LCDR SPRINGER 1
USS JOHN F KENNEDY CV 67
OPERATIONS OA DIVISION
FPO AE 09538-2800

OFFICER IN CHARGE
NAVPACMETOCDET BAHRAIN
PFC 451 BOX 562
FPO AE 09834-2800 1

ATTN MAJ BOB NEUMANN ECJ5 P 1
HQ USEUCOM
UNIT 30400
BOX 1000
APO AE 09128

ATTN FKJ3 PL OA PLUME 1
COMMANDER USFK
APO AP 96205

NON-DOD ACTIVITIES (CONUS)

ATTN WILLIAM K MOORE 1
MEVATEC CORPORATION
1525 PERIMETER PARK SUITE 500
HUNTSVILLE AL 35806

ATTN JERRY JENSEN 1
JAYCOR
1430 OAK COURT SUITE 202
DAYTON OH 45430

CAPT DANIEL W MERDES
561 EASTERLY PARKWAY
STATE COLLEGE PA 16801-6404 1

ATTN ARNOLD S WARSHAWSKY 1
LAWRENCE LIVERMORE NATIONAL LABORATORY
TECHNOLOGY ASSESSMENT GROUP LEADER
D DIVISION MAIL STOP L 83
LIVERMORE CA 94550

DISTRIBUTION (CONTINUED)

	Copies
ATTN ANTHONY PATRICK KAMAN SCIENCES CORPORATION ENGINEERING SCIENCES DIVISION 2560 HUNTINGTON AVENUE SUITE 200 ALEXANDRIA VA 22303-1410	1
ATTN STEVE R DIEHL KAMAN SCIENCES CORPORATION PO BOX 7463 COLORADO SPRINGS CO 80933	1
ATTN DENNIS S STAPP SRS TECHNOLOGIES 500 DISCOVERY DRIVE NW HUNTSVILLE AL 35806-2810	1
ATTN EM 36 ANTHONY T SKINNER LORAL VOUGHT SYSTEMS CORPORATION PO BOX 650003 DALLAS TX 75256-0003	1
ATTN STEVE HURSH	1
JOE FANZONE SCIENCE APPLICATIONS INTERNATIONAL CORPORATION 626 TOWNE CENTER DRIVE SUITE 205 JOPPA MD 21085	1
ATTN RICHARD E MCNALLY SCIENCE APPLICATIONS INTERNATIONAL CORPORATION 7939 HONEYGO BLVD SUITE 229 BALTIMORE MD 21236	1
ATTN GREG BOWEN BATTELLE 505 KING AVENUE COLUMBUS OH 43201-2693	1
ATTN JAY WILLIS MEVATEC CORPORATION 1700 DIAGONAL ROAD SUITE 525 ALEXANDRIA VA 22314	1

DISTRIBUTION (CONTINUED)

Copies

ATTN DALE PACE   1
JOHNS HOPKINS UNIVERSITY
APPLIED PHYSICS LABORATORY
11100 JOHNS HOPKINS ROAD
LAUREL MD 20723-6099

ATTN MICHAEL KIERZEWSKI   1
OPTIMETRICS INC
1 NEWPORT DRIVE SUITE H
FOREST HILL MD 21050

ATTN CHUCK MARTIN   1
    ARTHUR DEVERILL   1
ARES CORPORATION
1800 N KENT STREET SUITE 1230
ARLINGTON VA 22209-2104

ATTN GEORGE ANNO   1
PACIFIC RESEARCH CORPORATION
2901 28TH STREET
SANTA MONICA CA 90405

ATTN DR JOHN A HASDAL   1
TELEDYNE BROWN ENGINEERING
PO BOX 070007
MS 50
HUNTSVILLE AL 35807-7007

ATTN DENNIS METZ   1
EAI CORPORATION
1308 CONTINENTAL DRIVE SUITE J
ABINGDON MD 21009

ATTN GENE MCCLELLAN   1
PACIFIC SIERRA RESEARCH CORP
1400 KEY BOULEVARD
SUITE 700
ARLINGTON VA 22209

ATTN TERRY JARRETT   1
HORIZONS TECHNOLOGY
3990 RUFFIN ROAD
SAN DIEGO CA 92123-1826

DISTRIBUTION (CONTINUED)

Copies

ATTN ROSS JAMISON   1
PHYSITRON CORPORATION
3304 WESTMILL DRIVE
HUNTSVILLE AL 35805

ATTN CHARLES HOLMES   1
BDM FEDERAL INC
1501 BDM WAY
MCLEAN VA 22102-3204

ATTN ALAN J SIEGEL   1
ENSCO INCORPORATED
APPLIED RESEARCH AND SYSTEMS DIVISION
445 PINEDA COURT
MELBOURNE FL 32940

ATTN WILLIAM HACKER   1
APPLIED RESEARCH ASSOCIATES INC
4300 SAN MATEO BLVD NE SUITE A220
ALBUQUERQUE NM 87110

ATTN DR CHOW   1
RAND CORPORATION
1700 MAIN STREET
DTP 2
SANTA MONICA CA 90407

ATTN DR DAVID MCGARVEY   1
POET ARTI
1745 JEFFERSON DAVIS HIGHWAY
SUITE 1100
ARLINGTON VA 22202

ATTN TODD R QUACKENBUSH   1
CONTINUUM DYNAMICS INC
PO BOX 3073
PRINCETON NJ 08543

ATTN DR JAD BATTCH   1
SCIENCE APPLICATIONS INTERNATIONAL CORPORATION
1225 JOHNSON FERRY ROAD SUITE 100
MARIETTA GA 30068

DISTRIBUTION (CONTINUED)

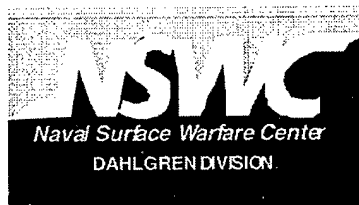|	Copies
ATTN STEVE JOHNSON DELTA RESEARCH INCORPORATED 325 WYNN DRIVE SUITE 1 HUNTSVILLE AL 35805	1
ATTN JACKIE LEWIS PLG 7315 WISCONSIN AVENUE SUITE 620 EAST BETHESDA MD 20814-3209	1
ATTN MARK BOVANKOVICH LORAL ADVANCED DISTRIBUTED SIMULATION TECHNOLOGY 12151 A RESEARCH PARKWAY ORLANDO FL 32826	1
ATTN HERB BRACEWELL INNOVATIVE RESEARCH CORPORATION 6564 LOUISDALE COURT SUITE 800 SPRINGFIELD VA 22150	1
ATTN JEFFREY S HUTH MSAC LOGICON RDA 2100 WASHINGTON BLVD SEQUOIA 2ND FLOOR ROOM 2078 ARLINGTON VA 22204-5706	1
ATTN DR RONALD R PARENTI MS S3 223 MIT LINCOLN LABORATORY 244 WOOD STREET LEXINGTON MA 02173-9185	1
LOS ALAMOS NATIONAL LABORATORY TECHNOLOGY AND SAFETY ASSESSMENT DIVISION SYSTEMS ENGINEERING AND INTEGRATION GROUP GROUP TSA 3 MAIL STOP F607 LOS ALAMOS NM 87545	1
ATTN GERALD FROST RAND 1700 MAIN STREET PO BOX 2138 SANTA MONICA CA 90407-2138	1

DISTRIBUTION (CONTINUED)

	Copies
ATTN VLADIMIR KOGAN BATTELLE 505 KING AVENUE COLUMBUS OHIO 43201-2693	1
ATTN MATTHEW ANDERSON SCIENTIFIC AND TECHNICAL ANALYSIS CORPORATION 11250 WAPLES MILL ROAD SUITE 300 FAIRFAX VA 22030	1

INTERNAL

	Copies
B	1
B20 GRIPSHOVER	1
B50 GIBBS	1
B51 AMICK	2
B51 MORRIS	2
J042	5
J07	5
J33	15

THIS PAGE INTENTIONALLY LEFT BLANK

NAVAL SEA SYSTEMS COMMAND

NSWC

Naval Surface Warfare Center
DAHLGREN DIVISION

PanamaCity   Dahlgren